Development of a Thermal Model for an Inner Stator Type Reluctance Motor

by

Michael J. Pieterse

A thesis
presented to the University of Waterloo
in fulfillment of the
thesis requirement for the degree of
Master of Applied Science
in
Mechanical Engineering

Waterloo, Ontario, Canada, 2009

I hereby declare that I am the sole author of this thesis. This is a true copy of the thesis, including any required final revisions, as accepted by my examiners.

I understand that my thesis may be made electronically available to the public.

Abstract

Thermal modeling is an important aspect of electric motor design. Numerous techniques exist to predict the temperatures in a motor, and they can be incorporated in the design of a thermal model for a new type of electric motor. This work discusses the available modeling techniques and determines which methods are applicable for medium-sized motors with either natural convection or forced convective cooling over irregular geometry. A time-dependant thermal model, with thermal transport parameters based upon geometric and simplified air flow information, is developed based on a discrete lumped parameter model with several modifications to improve accuracy. The model was completed with the aid of nine experiments, and the result is a thermal model that exhibits an absolute error of less than 6.1°C for the nine test runs at three different currents between 8.4 A_{rms} and 28.2 A_{rms} and three cooling levels, natural, 10.7 CFM and 24.4 CFM.

Acknowledgements

I would like to thank my supervisor Dr. Roydon Fraser for his guidance and mentorship over the past few years, and also for connecting me with Sprung-brett RDI which presented me the opportunity to work on this project. I would like to thank the founder and CEO of Sprung-brett RDI Michael Brewster for steering me towards the thermal management aspects of the motors and his continuous focus on my development and my being a member of the team. I would also like to acknowledge the help of Dr. Shohel Mahmud at Sprung-brett RDI for his effective co-supervision and his guidance with all aspects of thermodynamics, heat transfer, and thermal modelling.

I would like to thank Meikle Automation and their employees for their patience with me as I ran the experiments over two weeks in their facilities.

I would like to acknowledge Andre Hladio for his creation of the control system required to run the motor and collect data from the input side.

I have been supported financially throughout this work by the Natural Science and Engineering Research Council of Canada through an Industrial Postgraduate Scholarship, for which I am most thankful. I would also like to thank the department of Mechanical and Mechatronics Engineering at the University of Waterloo for the teaching assistantship positions I have held.

I would like to thank my family for all their support and encouragement, and my friends for helping me really enjoy the time.

Finally I would like to thank Jay Lee for all her love, support, interest, and understanding.

Dedication

I would like to dedicate this thesis to Martin Pieterse and Walt van der Zwet, without whom none of this would have been possible.

Table of Contents

Appendices

List of Figures

List of Tables

Nomenclature

Roman Symbols

A	area, m²; accuracy
a	geometric parameter, m
B	magnetic flux density, T
b	geometric parameter, m
C	heat capacity, J/K
C_n	constant of integration, (various units)
c	specific heat for solids, J/kg·K
c_p	constant pressure specific heat, J/kg·K
D	electric flux density, C/m²
D_h	hydraulic diameter, m
E	electric field intensity, V/m; energy, J; emissive power, W/m²
F_{ij}	view factor between surfaces i and j
f	frequency, Hz; friction factor
H	magnetic field intensity, A/m
h	convective heat transfer coefficient, W/m²K; height, m
I	electric current (constant), A
i	electric current (variable), A
J	current density, A/m²

Greek Symbols

α	thermal diffusivity, m²/s; absorptivity
β	coefficient of thermal expansion at constant pressure, $^{\circ}C^{-1}$, K^{-1}
γ	temperature coefficient, $^{\circ}C^{-1}$, K^{-1};
δ	tolerance, m; skin depth, m
Δ	difference of a parameter
ε	permittivity, N/A²; emissivity
μ	magnetic permeability, N/A²
μ_r	relative magnetic permeability
ν	kinematic viscosity, m²/s
ρ	density, kg/m³; electric charge density, C/m³
ρ_e	electrical resistivity, Ω·m
τ	torque, N·m; time constant, s
ω	rotational velocity, rad/s

Constants

μ_0	permeability of free space, $4\pi \times 10^{-7}$ N/A²
σ	Stefan-Boltzmann constant, $5.67 \times 10^{-8}\ W/m^2K^4$

K	conductance, W/K
k	thermal conductivity, W/m·K
L	length, m, inductance, H
m	mass, kg
N	gear ratio,
n	number of turns; number of laminations
n_c	coil packing factor
n_B	flux density saturation factor
n_f	copper fill factor
n_L	number of conductors in one layer
n_s	iron stacking factor
n_T	thermal factor
P	power, W; perimeter, m
P_i	iron loss, W
P_w	wetted perimeter, m
p	pressure, N/m², Pa
Q	flow-rate, m³/s
q	heat transfer rate, W
q_{gen}	total heat generation, W
q'	heat transfer rate per unit length, W/m
q'_{gen}	heat generation per unit length, W/m
q''	heat flux, $\mathrm{W/m^2}$
q'''_{gen}	heat generation per unit volume, $\mathrm{W/m^3}$
R_e	electrical resistance, Ω
R_t	thermal resistance, K/W

Dimensionless Groups

Gr	Grashof number
Nu	Nusselt number
Pr	Prandtl number
Ra	Rayleigh number
Re	Reynolds number

Subscripts

0	initial condition
avg	average
b	blackbody
c	contact; cross section
coil	relating to an entire coil
cond	conductive
conv	convective
core	relating to the iron core
e	electrical
enc	enclosure
est	estimate
eq	equivalent
ext	external
f	final
hold	holding
i	inner, initial, impregnation
in	in, input
max	maximum
mech	mechanical
min	minimum
n	counter

R_t''	thermal resistance per area, m^2K/W
RPM	rotational speed, rev/minute
r	radius, m
SCL	specific core loss, W/kg
T	temperature, K (°C)
t	time, s; thickness, m
U	heat transfer coefficient, W/m^2K
V	volume, m^3
v	voltage, V

o	outer
out	output
peak	peak amplitude
r	radial
rad	radiation
ref	reference
rms	root mean square
s	surface
ss	steady state
surr	surroundings
t	transverse
w	referring to a specific waveform
wire	relating to a single wire
ϕ	phase
∞	ambient

Chapter 1

Introduction

An innovative type of electric motor has been developed by Sprung-brett RDI (2007) based on Davison (2004) which exhibits a very high torque to mass ratio by virtue of its operating method. As a result, the motor does not require an external gearing, such as a gearbox or planetary gear system to reduce the speed and increase the torque. The new motor, seen in Figure 1-1, is based upon an eight-pole switched reluctance motor, and for optimal packaging it requires the inversion of a traditional motor where the stator is now central instead of surrounding a central rotor. Though not unheard-of for electric motors, this configuration means that heat is generated in the middle of the motor, but then lacks a direct path for its removal, unlike in a traditional motor where the outer face of the stator can act as a heat sink to the environment. The heat generation, through various mechanisms, will cause the temperatures of the components of the motor to rise which will have negative impacts upon the performance of the motor. As the temperature rises, particularly the coil temperature, Yoon et al. (2002) note that the efficiency of the motor decreases, the electrical insulation degrades, and ultimately the useful life of the motor is diminished. It is important to gain an understanding of heat flows and thermal response in the stator so that safe operational guidelines can be developed for the prototype motor. Subsequent generations of the motors then can be designed with thermal response in mind, or feature an integrated cooling system to control temperatures and maximize performance.

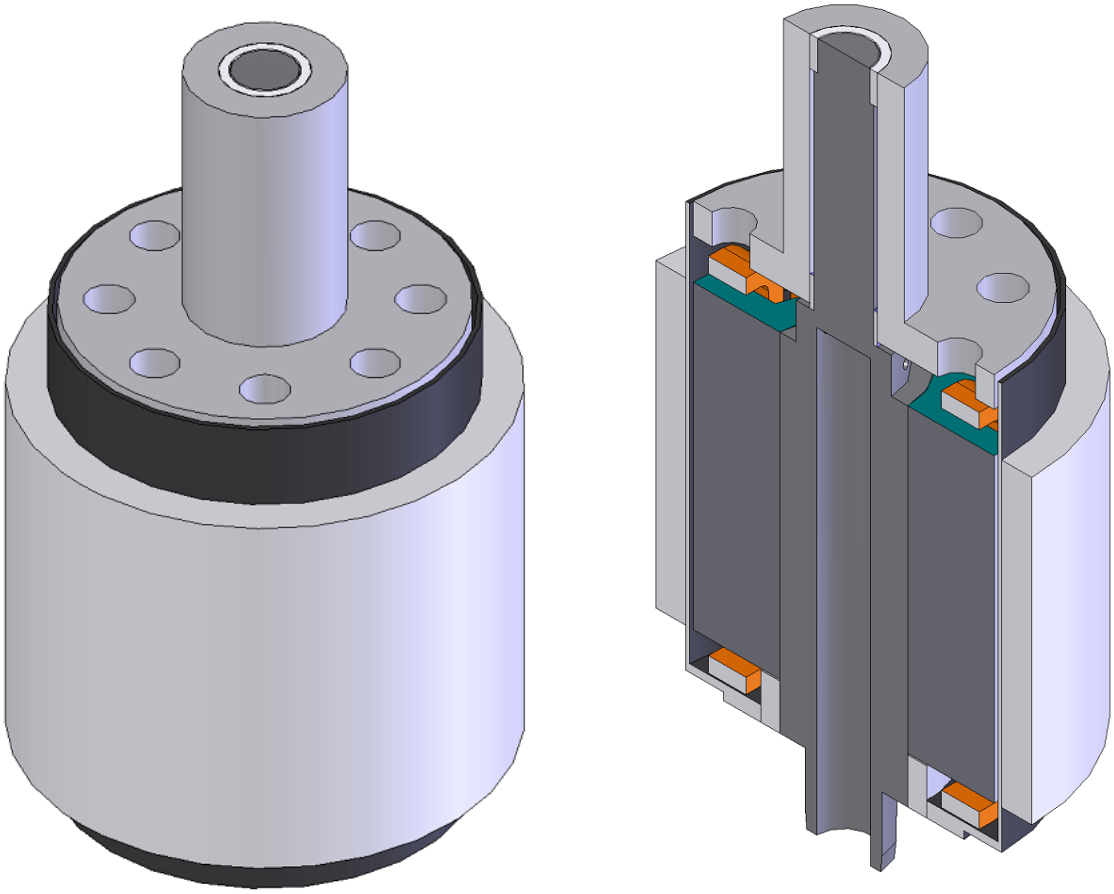

a) external view b) internal view

Figure 1-1: Prototype motor solid model. Model from Sprung-brett RDI (2008)

1.1 Motivation

Thermal characteristics play a large role in the design of, and place limits upon the performance of, a motor. The temperatures which are expected to be encountered dictate the class of insulation to be used on wires, limit the material selection based on melting-points, curie temperatures, thermal expansion, and other mechanical and electrical factors. At the same time, a user would expect to not be burned by touching the casing of the motor, which further restricts the performance. Thermal performance was once an afterthought in the design of an electromagnetic machine; however Boglietti et al. (2008) observe that as the

knowledge of heat generation and flow in motors improved, the thermal design became an important part of the design and optimization process. As computers became more advanced, it became possible to fully envision the temperature distribution in a motor before it was ever produced, allowing careful designers to maximize the performance of their motors. The first generation prototype motor was designed without an integrated thermal-electromagnetic approach, therefore the limiting performance needs to be determined for a variety of operating modes. The successful application of a thermal model to this new motor would allow future motors to be designed with an integrated approach, allowing motors beyond the prototype model to be more compact, cooler, and more efficient.

All heat that is generated in the motor is a function of the current supplied to the stator windings, therefore the temperature rise in the motor can be determined as a function of this input parameter, however models will have to be created to address the heat generation mechanisms. There are two operating modes of interest: transient, in which a desired current is provided and the time it can be supplied is determined based on the maximum acceptable temperature rise, and steady-state performance, where the maximum current is determined based on the permissible temperature rise. A factor in both operating modes is the cooling performed by the internal airflow; the model should be able to specify the cooling air-flow required to operate the motor at a desired current level while maintaining temperatures below a specified limit.

As this is a new type of motor, the temperature rise under the various operating conditions is unknown. A full understanding of the temperature distribution in various operating modes will allow for the determination of a limiting duty cycle, if any, and will allow for the prediction of the degradation of performance when operating under extreme conditions. Without an understanding of how the heat flows in the motor, it will be difficult to implement an effective cooling strategy.

1.2 Research Objectives and Approach

The objective of this work is to develop an accurate thermal model of the prototype motor in order to predict thermal performance, determine operational limits, and provide a tool to optimize the design of next-generation motors of similar construction.

The approach taken to reach the objective is to first gain an understanding of the phenomena that will dictate both temperature and performance. A sophisticated motor model will require accurate models of individual modes of heat transfer and generation, which in turn will require the mechanical, thermal and magnetic properties of the constituent materials. These material properties are dependant upon the local temperature, and the heat sources depend on the temperature and the magnetic properties; in order to develop an accurate thermal model, the interactions between electrical, magnetic and thermal domains must be considered and applied correctly. Material properties will be found in thermal modelling literature, as well as material property databases. The models of relevant thermal phenomena and their interactions will come from heat transfer literature and motor-specific literature when available. In some cases new models will be developed in order to incorporate various phenomena in the final motor thermal model.

Once the materials and mechanisms are understood and modelled, a model of the entire motor can be constructed. This model could be made very complex; as Boglietti et al. (2008) observe, complexities arise in many forms: intricate geometry, complex three-dimensional fluid (air) motion, temperature dependence of material properties, unknown composite material properties, and thermal contact resistance. Different types of models will be assessed, their strengths and weaknesses compared, and ultimately the optimal modelling approach for this application will be selected and applied. Following the construction of the model and running of simulations, the prototype motor will be used for extensive thermal testing to validate the model, and to help gain a further understanding of the heat flow wherever the actual thermal field disagrees with the predicted field. Data from the testing will be measured using thermocouples and heat flux sensors to provide complimentary thermal data; the thermocouples will help validate local temperatures, while the heat flux sensors will help to validate the path of the heat flux.

1.3 Literature Review

The simultaneous consideration of the flow of both heat and magnetic flux is paramount for creating smaller motors that can operate at a low temperature and still generate the required torque. Commercial software exists that assists the engineer with the development of the

motor. Motor CAD by Motor Design Ltd. (2009) for example assists an engineer with the thermal aspects of the motor design and allows for evaluation of cooling schemes including natural or forced convection, radiation and spray cooling among other methods. Related software called SPEED, also by Motor Design Ltd. (2007) features a full suite of motor design tools that includes electromagnetic and thermal finite element analysis. The prototype motor represents a new type of motor which is not featured in commercial packages, hence the thermal model must be built upon the same fundamentals as SPEED or Motor CAD. In fact, Motor Design Ltd was founded in 1998 by Dr. Dave Staton, whose name frequents not only the references of this thesis, but the motor thermal modelling literature which forms the groundwork of this thesis.

In order to create a thermal model of the prototype motor, existing motor models were first investigated. Boglietti et al. (2008) identify two approaches to thermal modelling in electric motors: analytical lumped-circuits and numerical methods. Both of these approaches include finite element analysis (FEA), used for the modeling of conduction within solid geometries, and computational fluid dynamics (CFD), used to predict fluid flow and model convection around complex geometries such as end-windings. Whether a lumped-circuit or numerical model is developed, the convective boundaries must be modeled.

Matveev (2006) suggests that both 2D and 3D FEA have significant drawbacks. The computational time required for an accurate 3D model is considerable, while the loss of accuracy by simplification to 2D is unacceptable. In addition to the challenges posed by FEA, the difficulty associated with the development of a thermal model is discussed; Matveev notes that exact determination of the thermal field is impossible due to complex airflow, unknown or elusive thermal parameters and unknown or unmodelled loss components. Regardless, the results obtained by thermal circuit analysis or 3D finite element analysis are extremely useful as order of magnitude estimates.

Since it is impossible to develop an exact thermal model, it is important to understand the variability which can be induced by inaccurate data. Boglietti et al. (2005) performed a sensitivity analysis on complete and simplified models of a totally enclosed fan cooled (TEFC) motor. Tests were performed on five motors with power ratings of 4 kW, 7.5 kW, 15 kW, 30 kW and 55kW, a range in which the prototype motor falls. Parameters such as the

emissivity, natural convection coefficient and impregnation varnish conductivity were varied by -80% to +100%, and were shown to cause changes in peak temperature between -3.7% and +34%. The authors concluded that an accurate emissivity is of extreme importance when cooling is by natural convection, as is the extreme case for the prototype motor.

Boglietti et al. (2008) discuss the critical thermal model parameters that must be incorporated to develop an accurate model. They suggest that an experienced designer can make informed decisions regarding the value of critical model parameters, including interface gaps between components and the effective winding thermal conductivity. For an inexperienced designer the authors suggest that sensitivity analyses can be employed to determine which parameters are of critical importance.

Staton et al. (2005) note the interrelation of electromagnetic and thermal design which governs motor performance. The authors discuss the most challenging aspects of thermal modelling in small and medium induction motors, motors the same size as the prototype motor. The notable challenges include: the gaps between components, winding models, internal and external convective cooling, heat transfer across the air-gaps, and the uncertainty of material properties. Interfacial thickness and effective thermal conductivities are provided for a wide range of materials similar to those used on the motor: iron, aluminum, and copper. They note that accounting for the random variations in the position of each individual conductor when modelling the windings is not necessary to obtain an accurate temperature distribution. They instead develop a layered winding model to account for the temperature distribution in the coils, an approach echoed by Matveev (2006). For convective modelling, well-known correlations such as those presented in heat transfer textbooks such as Arpachi and Larsen (1984), Arpachi et al. (1999) or Incropera and DeWitt (2002) are used. The authors recommend performing a CFD analysis for the particular geometry of a motor's "end space", as curve fits to experimental data from other motors are unlikely to be successful due to the geometric differences between motors. For the thin air-gap between the stator and rotor, the key parameter governing the magnitude of the heat transfer is the Taylor number, which determines the form of the air flow: laminar vortex or turbulent. For the uncertainty of material properties, one of the first deficiencies discussed by the authors is the lack of

published thermal conductivity for silicon iron steels. Another complexity is the directionally dependant thermal conductivity of the stack of iron that forms stators and rotors.

Before a CAD design is begun, often a spreadsheet is used to analytically predict motor parameters and suggest geometry based on input parameters such as total diameter or desired torque. It is generally accepted that a finite element model will give the most accurate results, however the time required to build such a model can be considerable. Lumped circuit models have been shown to give good results, as noted by Boglietti et al. (2008), Mellor et al. (1991) and Trigeol et al. (2006). Since one of the aims of the thermal model is adaptability to predict performance of future motor designs, perhaps the most useful model would be one in which geometric parameters are simply input and parameters such as maximum current, and thus torque, are determined based on the acceptable temperature rise. Rouhani et al. (2007) do just this; they use a lumped circuit thermal model in order to optimize the design of a switched reluctance motor.

To build a sufficiently advanced, yet computationally simple lumped circuit model, there is a wealth of literature to draw upon. Mellor et al. (1991) state that when creating a lumped parameter thermal model, the model needs to have sufficient detail to distinguish between various components of interest, notably coils, the stator, and the rotor. In addition to providing a picture of performance at steady state, a comprehensive model should include capacitance to provide a transient solution. The number of components that are modeled indicates the complexity of the model; however what results is a set of linear differential equations that is simple to solve using software such as MATLAB or Maple. The ease of solving these equations permits a lumped parameter model to be used for online temperature monitoring of an electric motor, which will serve to protect the motor, and can be used to evaluate performance under various duty cycles.

In a lumped parameter model, correctly modelling the thermal relationships between components is critical for determining the flow of heat. The lumped parameter model used by Mellor (1991), Bousbaine (1999), Boglietti et al. (2005), Guo et al. (2005) and Trigeol et al. (2006) is of the form

$$[C]\frac{d[T]}{dt} = [K][T] + [q_{gen}], \tag{1-1}$$

where [C] is a matrix comprised of the thermal capacities required to solve for time-dependant temperature data, [T] is a matrix of the component temperatures, [K] is a matrix of the thermal conductances between components, and [q_{gen}] is a matrix of the rates of heat generated in each component. For this type of model determining [K] is the most important aspect of the model, and also the most challenging.

Solid components of the motor interact in two ways: conduction and radiation. When the surrounding air is considered, however, natural and forced convection are also involved in the conductance matrix. Various conduction models are available; Boglietti et al. (2005) and Guo et al. (2005) base their thermal models on elements where the center is assumed to be at the average temperature of the element, which is inaccurate for some components with internal generation, while Mellor et al. (1991) and Bousbaine (1999) use an element that attempts to compensate for this fact.

For convection, Trigeol et al. (2006) combine the predictions of a control volume CFD analysis of the end space into a lumped parameter thermal circuit and find a high degree of agreement between their model and experimental data. Others such as Mellor et al. (1991) and Staton and Cavagnino (2006) use dimensional analysis and convection correlations to determine convective heat transfer coefficients, the former demonstrating strong agreement between the model and experimental data.

Most literature, such as Boglietti et al. (2008), recognizes the importance of radiation from the external surface of the motor, however Boglietti et al (2005) also note the importance of internal surface-to-surface radiation heat transfer when a motor lacks forced cooling. The prototype motor is equipped to allow forced cooling, however it will not always be available and internal radiation should therefore be considered. Boglietti et al. (2006) studied radiation heat transfer in a motor noting that the radiation heat exchange between the windings and the inner surfaces of the motor are of significant importance. The experiments were performed in a vacuum and heat transfer coefficients of the same order of magnitude as free convection were found.

The flow of heat in a motor is important, but of equal importance is the generation of heat in the first place. Ryff (1994) states that losses, and thus heat generation, can be classified in three ways: copper losses, iron losses, and rotational losses. Copper losses result from the

electrical resistance in the coils of a motor and the current passing through it which is dissipated as heat. Rotational losses can include friction against a rotor resulting from brushes on a DC motor, viscous dissipation inside bearing, or the air resistance against rotor motion. For the prototype motor, the only significant loss would be in the bearings, and even this is very small due to the low rotational speed.

The iron loss is more complicated. Reinert et al. (2001) state that iron losses result from remagnetization, and consist of hysteresis and eddy-current losses. In order for iron losses to exist, the magnetic flux density must fluctuate. Traditionally the iron losses were found using the Steinmetz equation which was originally published in 1892, and still provides good estimates of iron losses. The Steinmetz equation for volumetric core loss, as stated in Reinert et al. (2001), is of the form

$$q'''_{gen,core} = k_h f^{\alpha} B_{\max}{}^{\beta} + k_e f^2 B_{\max}{}^2, \qquad \textbf{(1-2)}$$

where α, β, k_h, and k_e are the Steinmetz coefficients which are specific to the material and thickness, f is the frequency of excitation and B_{max} is the peak magnetic flux. The Steinmetz coefficients are often provided by electrical steel. There are two important restrictions to the use of the Steinmetz equation: first that the induction is sinusoidal, and second that the peak induction does not exceed 1 T.

There is strong disagreement in the literature on how to deal with iron losses which result from non-sinusoidal flux density waveforms, likely owing to the fact that the physical nature of core loss is still not completely understood, a fact noted by Chen and Pillay (2002). One approach to handling non-sinusoidal waveforms with the Steinmetz equation was discussed by Gradzki et al. (1990) and Severns (1991), wherein they performed a Fourier decomposition of the waveform, and applied the resulting flux densities and frequencies of successive modes to the Steinmetz equations and summed the results to obtain the total core loss. This approach was criticized by Albach et al. (1996) and by Reinert et al. (2001) due to the use of superposition on a non linear system. Reinert et al. (2001) recognize the strength of the Steinmetz equation for calculation of core losses induced by sinusoidal waveforms and try to address the inaccuracy of the equation when applied to non-sinusoidal waveforms by developing a modified Steinmetz equation. Results obtained from the original and modified Steinmetz equations, as well as results from a Fourier expansion were compared to

experimental results for triangular excitation waveforms applied to ferri- and ferromagnetic materials, and found strong agreement between their new model and the experimental results for frequencies between 500 Hz and 20,000 Hz. Additionally, it was found that even the original Steinmetz equation was more accurate than the Fourier expansion approach. Two important notes about the results obtained using the modified Steinmetz equations are the fact that the frequencies analyzed are several times higher than the prototype motor's operational frequencies, and the new approach does not address the limit of 1 T.

Despite the criticism of the superposition approach, it remains a popular method to predict the core loss. Mthombeni and Pillay (2005) use superposition on a non-sinusoidal induction waveform to predict the core loss in switched reluctance motors operating with a 10 Hz fundamental frequency. Their method overpredicted the core losses by an amount that decreases with increasing flux density; at a fundamental peak stator flux of 1.4 T their predictions are high by 1.06% in the rotor pole and 11.12% in the rotor core. This work is significant for two reasons: the induction is over 1 T, and it shows that a Fourier expansion can give good results under conditions similar to what will be experienced in the prototype motor. A model known to over-predict is preferable to under-prediction, where the increased temperature will have negative consequences. To obtain these results, the authors used high frequency core loss data which they note has only recently been made available by steel manufacturers, so until recently the Steinmetz equation was the most accurate way to model core loss.

In addition to their work on core loss, Mthombeni and Pillay (2003) studied another potential source of loss in motors, that resulting from the switching frequency. For a pulse-width modulation (PWM) generated signal, such as that used by the prototype motor controller, the authors note that additional losses occur when the switching frequency of the PWM signal is below 5 kHz. Between 5 kHz and 20 kHz the losses were found to remain nearly constant.

1.4 Thesis Outline

This thesis documents the development of a thermal model for the prototype motor and the testing of the prototype motor to verify the model.

Chapter 1 presents an overview of the approaches taken in thermal modelling of electric motors, and switched reluctance motors where literature exists. The objectives and scope of the thesis work are discussed.

Chapter 2 discusses operation of the prototype motor in detail. The underlying electromagnetic and thermal physics are analyzed in detail and material parameters critical to the development of a thermal model are discussed. Simplifications are introduced where possible to improve the versatility of the model. Material properties are discussed with the purpose of removing temperature dependence where possible.

Chapter 3 discusses available modelling options in detail, and covers the development of a variety of thermal models of the prototype motor. Thermal models predict performance and thermal response as a function of operating mode and input waveform.

Chapter 4 details the experimental equipment which will be used to validate the prototype motor thermal model.

Chapter 5 presents the experimental approach taken to validate the thermal models. Results of experiments are presented and compared to predictions of thermal models.

Chapter 6 discusses the results of the experiments and modelling and draws conclusions regarding the strengths and shortcomings of each model. Recommendations are presented for future work.

The work performed is summarized in Figure 1-2.

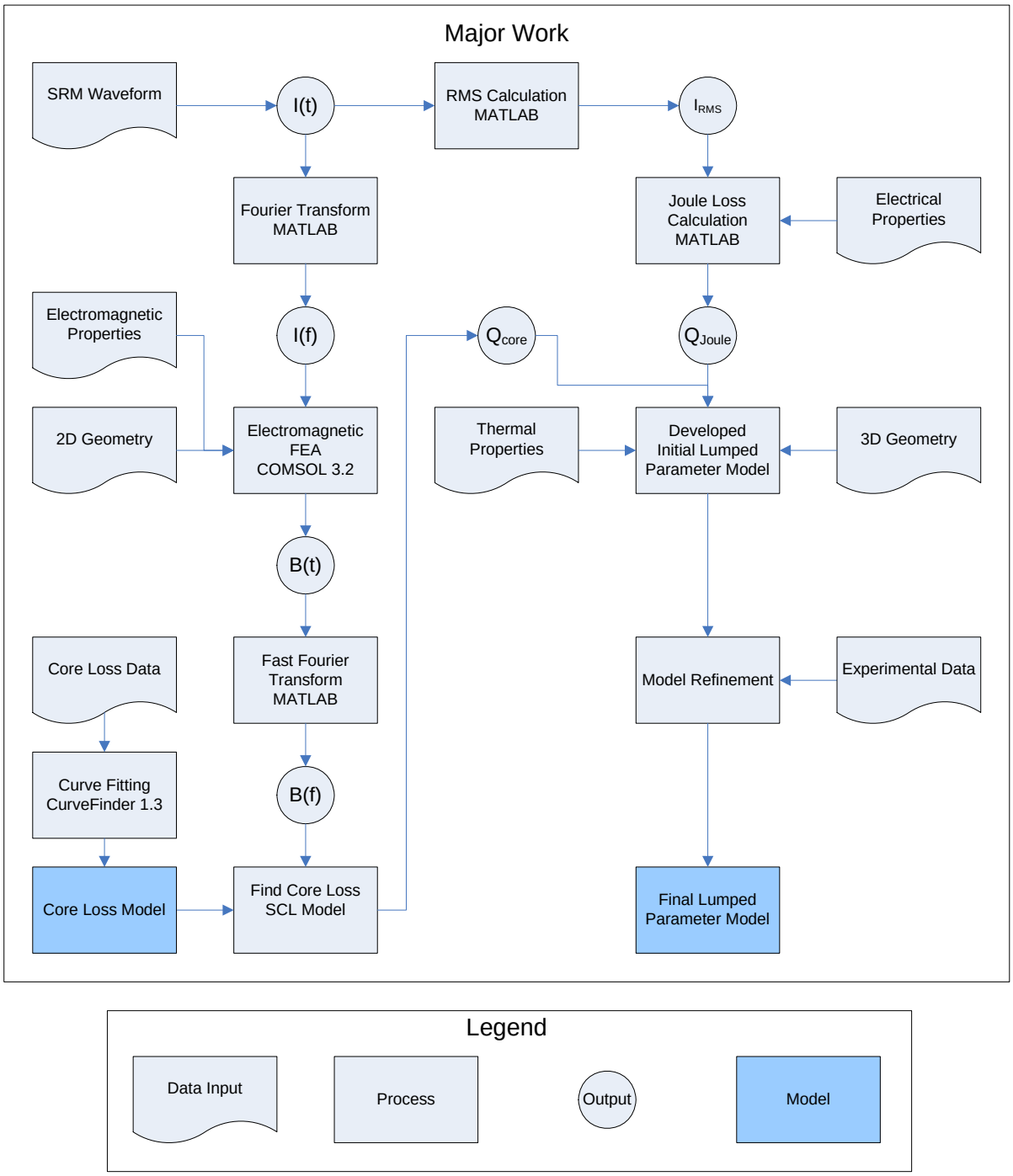

Figure 1-2: Outline of work

Chapter 2

Motor Physics

The prototype motor is a highly complex system which relies on the interaction of several physical phenomena in order to operate. The objective of this work is to create an accurate thermal model of the motor, but before any models can be constructed the underlying physics of heat transfer, fluid dynamics and electricity and electromagnetism, must be well understood. The most challenging aspect of thermal modelling is the coupling of these domains and determining which phenomena from each domain must be accounted for, even in the simplest thermal models. Another challenge lies in the strong temperature dependence of several material properties including magnetic permeability, thermal conductivity, and electrical resistivity. Because thermal generation is dependant upon temperature via the magnetic field characteristics and the electrical resistivity, an iterative solution must be adopted to achieve a high level of accuracy. The coupling of equations can be handled by multiphysics finite element modeling, which can provide a highly accurate spatial and temporal prediction of performance if all relevant phenomena are considered. For simpler models, however, average values could be used; part of this chapter will be devoted to determining such values. Because of the complex geometry and three-dimensional airflow in the stator, even the simplest model must consider three dimensional effects to some degree.

2.1 Fundamentals of the Motor

Understanding the motor first requires an understanding of the underlying technologies which are presented in Sprung-brett RDI (2007) and Davison (2004). The prototype motor is built upon, and takes advantage of the operation of a switched reluctance motor (SRM) and a gear reducing mechanism called a harmonic drive. A brief overview of these two technologies will be presented briefly before their integration into the motor is discussed. The important components which form the prototype motor will then be discussed followed by an introduction to the path of energy through the motor. This information will lay the groundwork for the thermal modeling strategy which will then be introduced.

2.1.1 Introduction to Switched Reluctance Motors

In a switched reluctance motor, the rotor revolves as it tries to align with the active poles, as seen in Figure 2-1; successive phase activation causes a continuous motion. The rotation is caused by the magnetic field which exerts a force on the rotor when it is not aligned with the excited poles, resulting in an electromagnetic torque. The term switched reluctance arises from the way that the inductance changes with the rotor's angular position. When the rotor is aligned the magnetic reluctance is minimized due to the increased presence of iron along the flux path, and as a result the inductance is maximized. When the rotor is not aligned with a particular phase the reluctance is much higher because there is more air along the flux path, which results in a lower inductance.

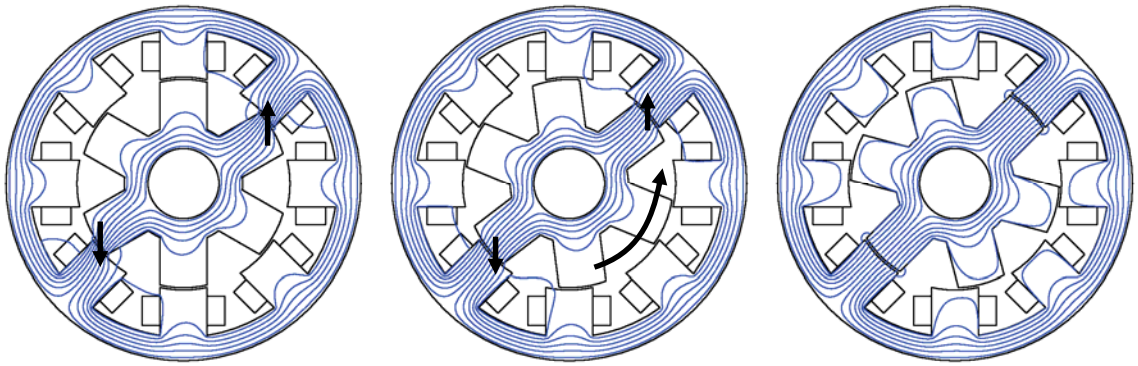

a) one phase activates, exerting a force on the poles

b) causing the rotor to rotate until

c) rotor pole is aligned with active phase

Figure 2-1: Switched reluctance motor operation

2.1.2 Introduction to Harmonic Drives

A harmonic drive is a single-stage gear reducing mechanism which, according to Tuttle (1992), offers typical gear ratios ranging from 50:1 to 320:1. A harmonic drive consists of three components: a wave generator, a flexible spline and a circular spline, which can be seen in Figure 2-2.

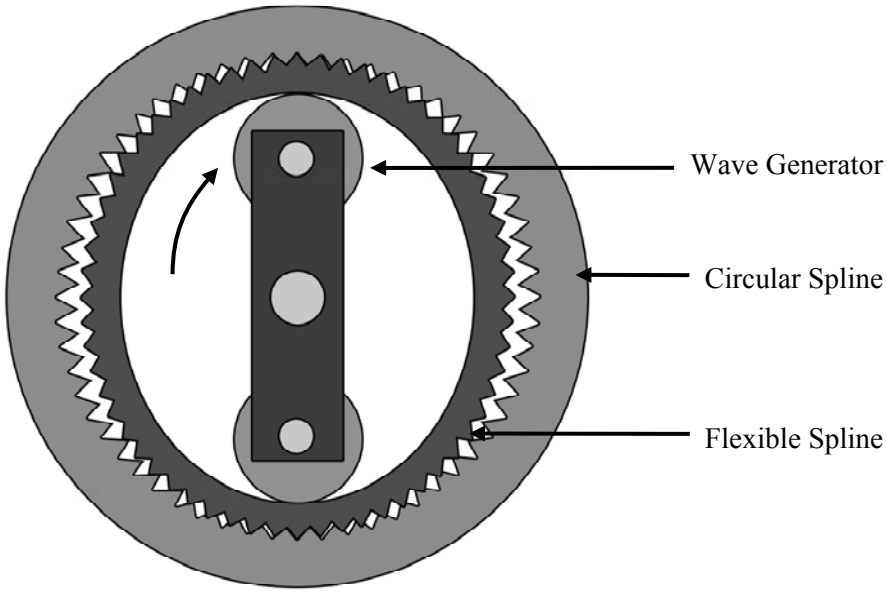

Figure 2-2: Principle of harmonic drive, adapted from Encylopædia Britannica (2009)

As the wave generator rotates, it deforms a flexible spline into an elliptical shape which propagates at the same speed as the wave generator. The deformation causes gear teeth on the flexible spline to engage with teeth on a circular spline which has a different number of gear teeth. If either the flexible spline or circular spline are fixed in position, the motion of the wave generator and the force exerted by the rigid spline will cause a rotation in the other spline.

2.1.3 Principles of the Motor

The first major difference between the prototype motor and a traditional switched reluctance motor is that the stator is on the inside. The second difference is that instead of using the stator to cause a rotor to rotate, the stator is instead used in place of a physical wave generator to generate magnetic force which causes the surrounding flexible spline, referred to as the flexispline, to deform, causing the flexispline's gear teeth to engage with a spur gear.

In order to further the understanding of motor thermal behaviour and help identify required model parameters, it is important to discuss some aspects of how the prototype motor works. First, there are two modes of operation: holding and rotating, which can be seen in Figure 2-3. In the holding case, one phase, two opposite poles, energize with a constant current, for as long as a zero rotation counter-torque is desired. In the rotating case, each phase is energized by the same waveform, however each phase lags the preceding phase by 90°, which causes the orientation of the generated magnetic field to rotate and complete one full revolution in the same time as one period of the energizing waveform. It can be seen in Figure 2-3 that the two operating modes will result in two completely different temperature distributions. When holding, a DC current is provided to one phase, two opposite poles, and it's there that the highest temperature will be encountered while the other coils are significantly cooler which results in angular symmetry at 90°. In the rotating case each coil undergoes an identical amount of heating resulting in angular symmetry at 22.5°. This symmetry will only truly be manifest when the motor is oriented in a vertical direction due to the magnitude of natural convective cooling varying with angle for a horizontal cylinder.

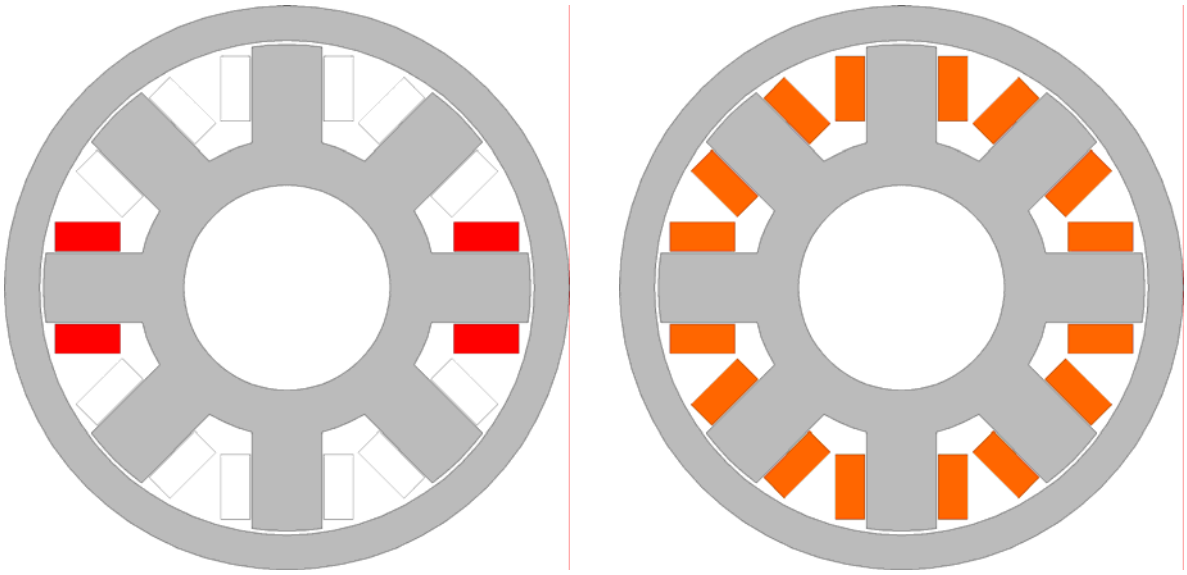

a) Holding condition, red coils on with 100% duty cycle

b) Rotating condition, orange coils each active with 25% duty cycle

Figure 2-3: Coil energization under different operating conditions

When rotating, two electrical cycles are required to complete a full revolution of the magnetic field. Due to the harmonic gearing, the spur gear rotates a fractional amount, per magnetic revolution, given by the gear ratio *N*. These factors lead to the relationship

$$\omega_e = 2N \cdot \omega_{mech} . \tag{2-1}$$

From this the fundamental frequency of the electrical input can be found using

$$f_e = \frac{2N}{60} \cdot RPM . \tag{2-2}$$

Based on the gear ratio and projected rotational speeds given by Sprung-brett (2008), the fundamental frequency of the electrical signal was found to be 13.33 Hz for the maximum motor RPM.

An important aspect of the motor is the thermal limitations imposed by the constituent materials. The maximum temperature in a motor will occur within the windings, and in the prototype motor these are specified to withstand 180°C, a Class H rating as per Sprung-brett (2008).

2.1.4 Identification of Motor Components

To successfully model the motor, first all significant components need to be identified. Figure 2-4 identifies the constituent components of the prototype motor. Of the components, the most important are the windings, the stator, and the fieldbooster. In addition to those components shown, an epoxy is present in the V-shaped void between adjacent coils.

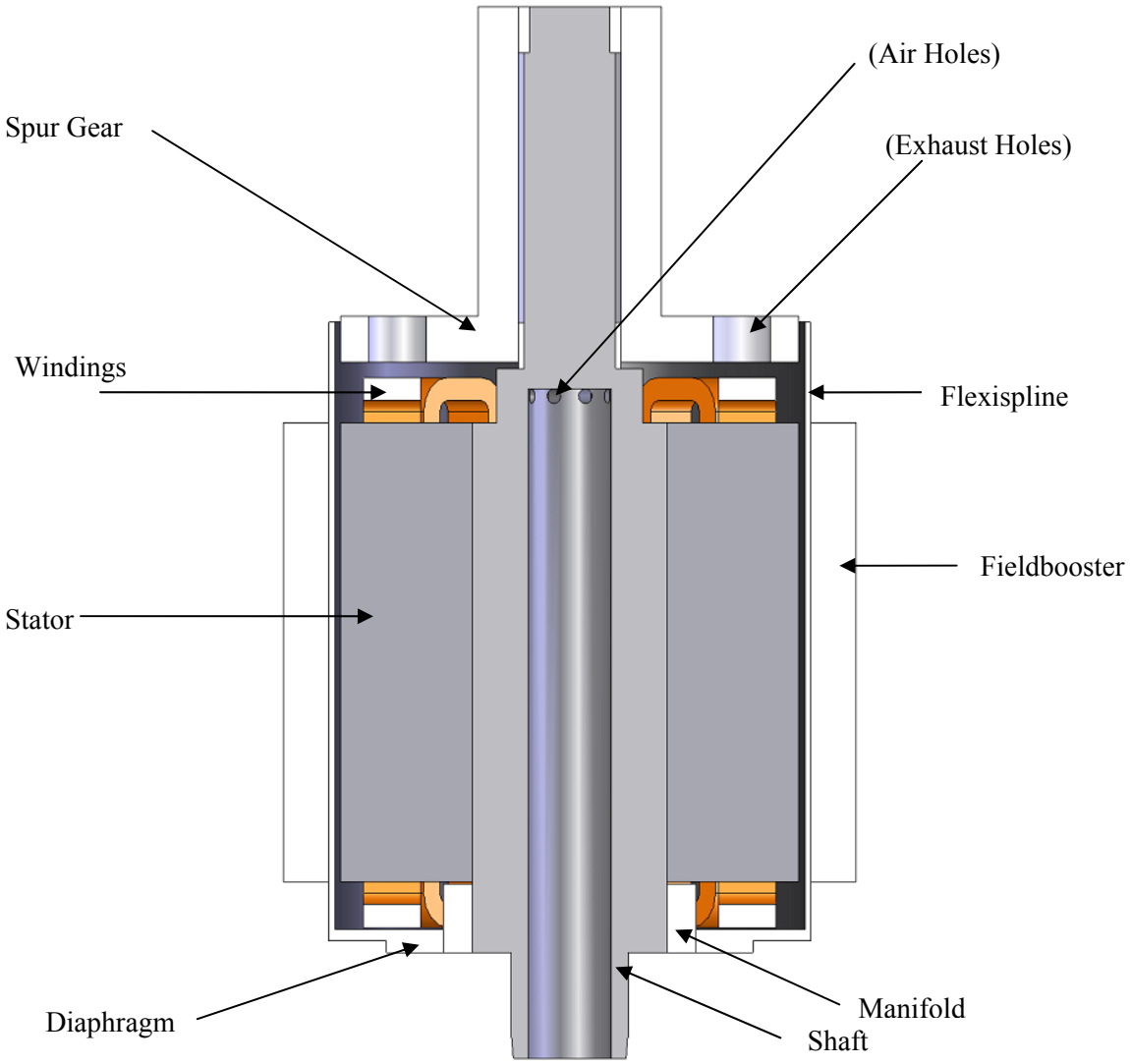

Figure 2-4: Identification of primary motor components and features (in parentheses)

The stator windings, or coils, are extremely important to the thermal model. Most of the motor's heat is generated in the coils via the Joule effect, and they represent the first thermal

resistance to heat flow. Consequently, they contain the hottest points in the motor. The coils are composite domains, consisting of copper wires, an enamel coating which provides a dielectric barrier between adjacent turns or between the copper and the stator, as well as a filler material between the turns, such as a bonding compound, a ceramic potting material, or simply an air gap. Staton et al. (2005) have shown that it is difficult and unnecessary to model the fine detail of the coils, but rather it is sufficient to use the bulk properties of this domain. Therefore, to ensure an accurate thermal model, the equivalent thermal conductivity and specific heat of the bulk domain must be determined. A consideration here is that the conductivity will be different in the transverse and radial directions; the transverse direction features continuous strands of copper, diminishing the overall conductivity by the packing factor, while the radial direction has the thermal resistances of the enamel and the filler material to account for. The coils are important for the electromagnetic model as they generate the magnetic flux that flows through the machine. Electrically, Matveev (2006) notes that the phenomena of the skin effect and proximity effect must be considered in the coils to accurately predict their heat generation.

The stator and fieldbooster are laminar constructions of a soft-magnetic iron alloy called M-19, and are of primary importance to the magnetic model. Throughout this work, the term 'iron' is often used, with the implication that it is actually an iron alloy. Due to the stacking of laminations, this material is a composite with directionally dependant material properties. The electromagnetic and thermal properties of the iron alloy were provided by the manufacturer, although the temperature dependence of these properties was unknown. The bulk properties of the iron composite will be determined from this information. The iron is of importance in the thermal model due to the transfer of heat through it and because of the heat generated within the laminations as a result of the magnetic irreversibilities and eddy currents created by the time-varying flux.

2.1.5 Energy Analysis of the Motor

In any electric motor, energy is converted from electrical potential to work using the magnetic field as an intermediary. With respect to energy, the beginning and end points of

the prototype motor match a standard motor, as seen in Figure 2-5, however the conversion path from electrical energy to work is slightly different. In the prototype motor, the electrical energy still creates a rotating magnetic field, but the magnetic force generated by the field is used to cause an elastic deformation of the flexispline component. When the magnetic field activates, force is generated at the two active poles that causes the flexispline to deform into an ellipse with its minor axis aligned with the active poles of the motor. As the magnetic field rotates the elliptical shape propagates and the gear teeth near the minor axis engage with the gear teeth on the spur gear causing a rotation in the direction opposite that of the elliptical propagation due to the strain wave phenomenon.

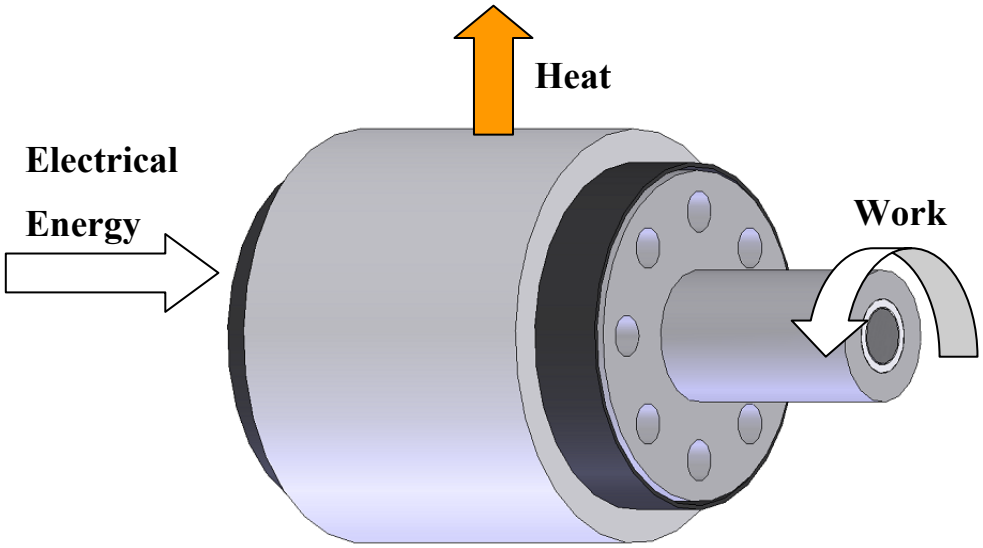

Figure 2-5: Energy analysis of the motor

The creation of a magnetic field generates heat due to losses of two types: joule loss in the windings due to their electrical resistance, and core loss in the stator and rotor iron as a result of a time-varying magnetic field. Electrically, because the prototype motor is based on a switched reluctance motor, the phase voltage can be represented by the equation

$$v = R_\phi i + L(\theta, i)\frac{di}{dt} + i\frac{d\theta}{dt}\cdot\frac{dL(\theta, i)}{d\theta}, \qquad \textbf{(2-3)}$$

as given by Krishnan (2001). Recognizing that power is the product of voltage and current, Krishnan (2001) states that the power is given by

$$P = vi = R_\phi i^2 + \frac{d}{dt}\left(\frac{1}{2}L(\theta,i)i^2\right) + \frac{1}{2}i^2\frac{dL(\theta,i)}{dt}, \quad \textbf{(2-4)}$$

which he reduces to

$$P = vi = R_\phi i^2 + \frac{d}{dt}\left(\frac{1}{2}L(\theta,i)i^2\right) + P_{out}, \quad \textbf{(2-5)}$$

where the first term, $R_\phi i^2$, represent the heat generated by the windings, the second term $d(L(\theta,i)i^2/2)/dt$ is the time rate-of-change of the magnetic field energy, and the third term, P_{out}, is the power output from the motor. Generally speaking, the output power from the motor will be

$$P_{out} = \tau\,\omega, \quad \textbf{(2-6)}$$

the product of the generated torque τ and the rotational velocity ω, which represents the useful work done by the motor. In the absence of a load or rotation the magnetic field still does work because the flexispline will continue to deform cyclically. Ultimately, from a thermal perspective the only important parameters are the phase resistance and the input current.

2.1.6 Modelling Approach

The following sections detail the fundamental electromagnetic and thermal equations that govern the behaviour of the device. Multiple types of models of varying sophistication exist that can be used to predict the behaviour of the motor. In the case of thermal models, the simplest models, such as a lumped parameter model, require convection coefficients on each face while more advanced CFD models need the 3D geometry of a fluid space, the fluid properties, and the boundary conditions. Because of the difference in sophistication of the available models, the following sections will determine the electromagnetic and thermal parameters which will be required for the simplest models.

Since the electromagnetic model is the most basic component, it will be investigated first with the goal of obtaining a model for the relative magnetic permeability. For the thermal

models, the thermal conductivity which is required for all thermal models will be investigated first. The next parameter to be investigated will be the convection coefficients which are required for lumped parameter models, but not for CFD models. Next, radiation parameters will be found which can be used in any thermal model, and then contact resistances will be found which can be used in a lumped parameter model and finite element software which has the ability to incorporate them. For any transient model the thermal capacity is required, hence the density and specific heats are sought. The final piece required for all models will be the heat generation in the windings and the iron. Once the parameters are found in the remaining sections of this chapter, the following chapter will delve into the creation of the thermal model.

2.2 Electromagnetic Parameters

The motor's electromagnetic behaviour can be thought of as the starting point of the entire thermal analysis. The motor is designed as a low-speed, high torque motor, and generally speaking the greater the current supplied, the greater the torque produced. The purpose of this work is to assess the temperature rise for a given operating condition, not to determine the torque.

The governing equations of electromagnetic fields are collectively known as Maxwell's equations. This series of differential vector equations, as outlined in Matveev (2006 include the Maxwell-Ampere law,

$$\nabla \times \vec{H} = \vec{J} + \frac{\partial \vec{D}}{\partial t}, \tag{2-7}$$

Faraday's law,

$$\nabla \times \vec{E} = -\frac{\partial \vec{B}}{\partial t}, \tag{2-8}$$

Gauss's law of magnetism,

$$\nabla \cdot \vec{B} = 0, \tag{2-9}$$

and Gauss's law for electricity,

$$\nabla \cdot \vec{D} = \rho \,, \tag{2-10}$$

where $\vec{B}$ is the magnetic flux intensity vector, $\vec{D}$ is the electric flux density vector, $\vec{E}$ is the electric field intensity vector, $\vec{H}$ is the magnetic field intensity vector, $\vec{J}$ is the total current density vector, and ρ is the electric charge density. In addition to Maxwell's equations, the equation of electromagnetic continuity,

$$\nabla \cdot \vec{J} = -\frac{\partial \rho}{\partial t} \,, \tag{2-11}$$

is used, as stated by Matveev (2006), as are the relationships

$$\vec{D} = \varepsilon \vec{E} \,, \tag{2-12}$$

and Ohm's law,

$$\vec{E} = \rho_e \vec{J} \,, \tag{2-13}$$

and

$$\vec{B} = \mu \vec{H} \,, \tag{2-14}$$

where ε is the permittivity, ρ_e is the electrical resistivity, and μ is the magnetic permeability. The magnetic permeability is commonly expanded such that

$$\mu = \mu_r \mu_0 \,, \tag{2-15}$$

where μ_0 is the permeability of free space, defined as $4\pi \times 10^{-7}$ N/A², and μ_r is the relative permeability of the material, approximately 1 for air, aluminum, and copper, nearly 700 for steel, and over 4000 for electrical steels. For M-19, seen alongside other electrical steels in Figure 2-6, the relative permeability in the linear region was calculated to be 7493 based on Sprague (1999).

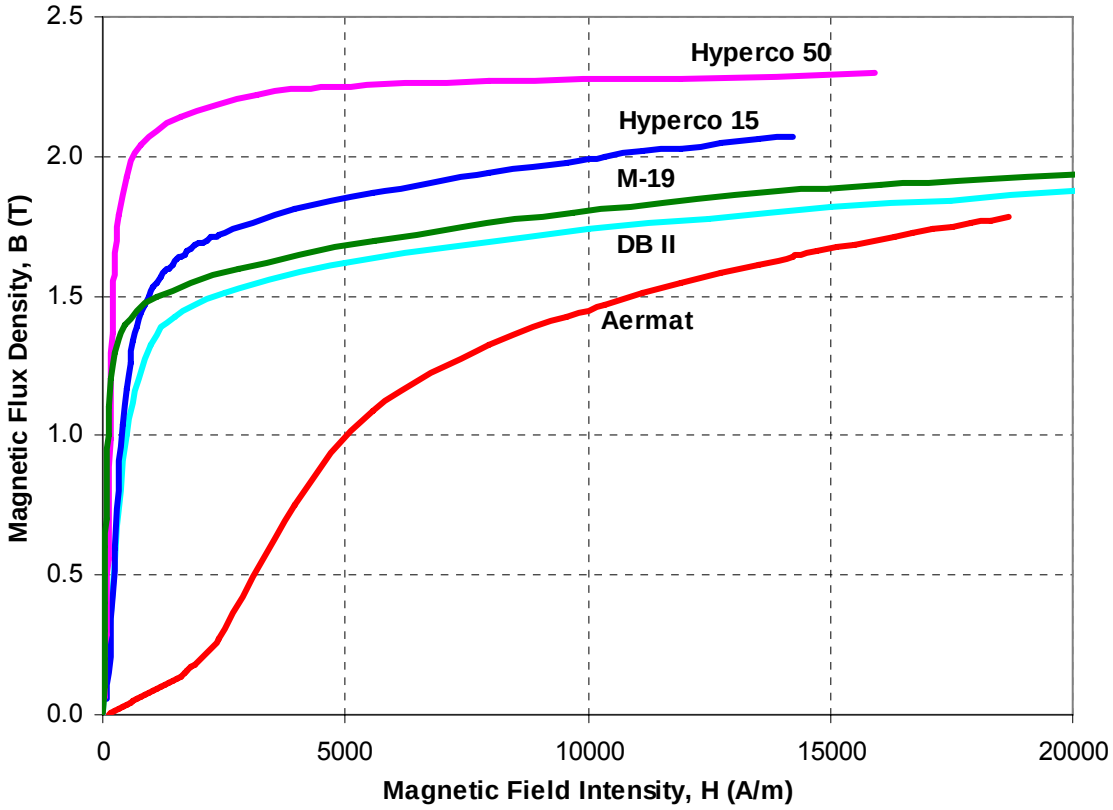

Figure 2-6: B-H curves for selected soft magnetic alloys, from Carpenter Technology Corportation and data from Nasar, 1987

The solution to Maxwell's equations is highly complex, and analytic solutions are limited to simple geometries. Another complexity is that the magnetic permeability is only linear for a limited range of magnetic field intensities. As the field strength H increases, the flux density B initially rises quickly, but then becomes saturated with flux which causes a diminishing increase in magnetic flux density as the field strength is increased, as seen in Figure 2-6. This means that in reality the magnetic permeability is a function of the magnetic flux density, resulting in (2-14) being non-linear. For these reasons, Maxwell's equations will be solved by finite element analysis.

B-H curves are well understood for ferromagnetic materials, but another important consideration is that the peak flux density decreases with a rising temperature, a facet which is highlighted in Figure 2-7 for several electrical steels. Unfortunately, temperature

dependant data for the magnetization of M-19 is not available, so an exact treatment of the temperature effect is impossible without detailed experimentation. Observing the effect on the known materials using the data from Kueser et al. (1965), however, it can be seen that from 26.7°C to 180°C the peak flux density drops by a minimum of 1.5% (Nivco Alloy) to a maximum of 4.7% (18% Ni). Because this drop in peak performance is small over the temperature range considered, the temperature effect will be neglected for this analysis. This assumption will cause the core loss to increase, however it will be demonstrated that the core loss is small with respect to the joule loss, hence even with an approximately 5% increase in the flux density the thermal generation will not increase substantially.

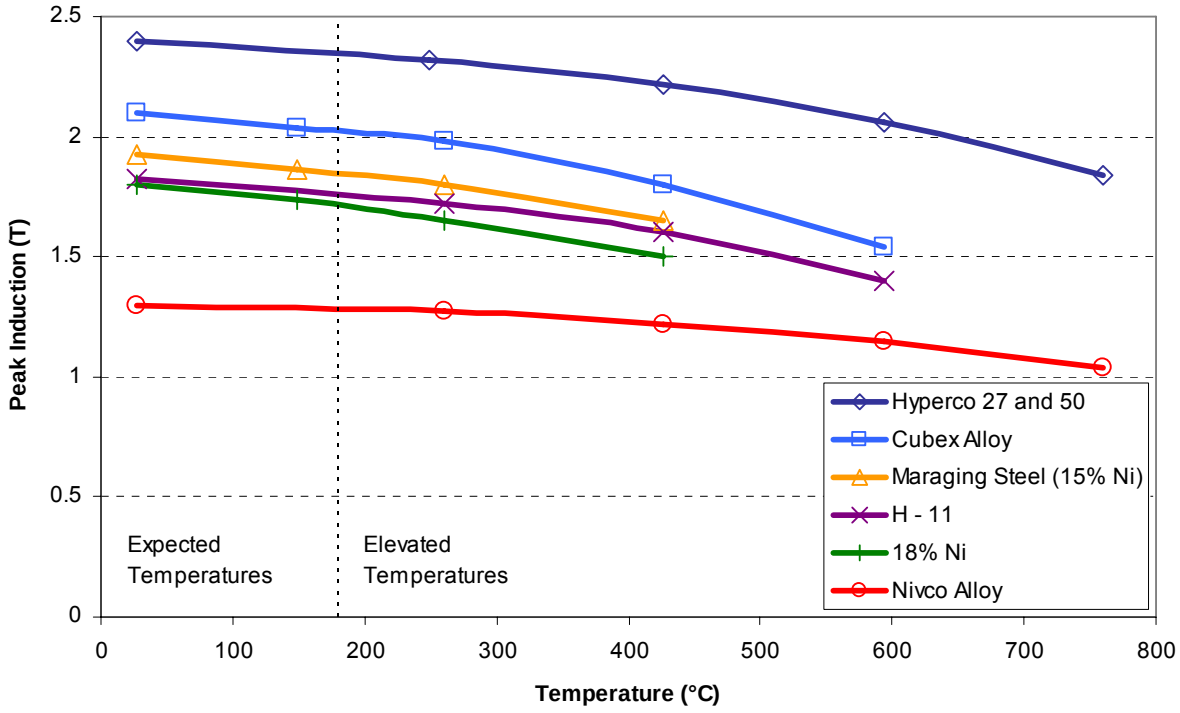

Figure 2-7: Temperature dependence of peak flux intensity in selected soft magnetic alloys at 2.0-2.4 kA/m, by Kueser et al. (1965)

2.3 Thermal Conductivity of Solid Domains

The simplest mode of heat transfer and the starting point of the thermal model is conduction. Regardless of the thermal model to be employed, the thermal conductivity of the components

that form the motor will be required. For one-dimensional heat transfer through an object, the conductive heat flux q''_{cond} is given by Fourier's law,

$$q''_{cond} = -k_x \frac{dT}{dx}, \tag{2-16}$$

where k is the thermal conductivity of the material in the direction x. The more general case of time-dependant three-dimensional flow of heat in a solid is governed by the equation

$$\rho c_p \frac{dT}{dt} = \frac{1}{r}\frac{\partial}{\partial r}\left(k_r \cdot r \frac{\partial T}{\partial r}\right) + \frac{1}{r^2}\frac{\partial}{\partial \theta}\left(k_\theta \cdot \frac{\partial T}{\partial \theta}\right) + \frac{\partial}{\partial z}\left(k_z \cdot \frac{\partial T}{\partial z}\right) + q'''_{gen}, \tag{2-17}$$

for a cylindrical coordinate system. In isotropic materials, the thermal conductivity coefficients k_r, k_θ and k_z will be equal, however thermal conductivity is a temperature dependent property, and if this dependence is considered, then (2-17) cannot be simplified yet. For simple models it may be desirable to choose a constant value of thermal conductivity to simplify the mathematics, where such a value is available in the literature. However in more detailed models a full temperature dependant conductivity should be used. Heat transfer by conduction is one of the most important modes of heat transfer in the motor due to the high ratio of solid volume relative to the total volume. In order to determine the thermal conductivities to be used in the model, the various materials will be considered and the range of values relative to the expected temperatures will be considered.

There are two categories of solids in the motor: isotropic and anisotropic. Isotropic materials include machined parts such as the spur gear, the central shaft and flexispline, while anisotropic solids are the stator, fieldbooster and the coils.

2.3.1 Iron Regions

The iron regions, the stator and fieldbooster, are both constructed of stacks of non-oriented M-19 silicon steel bonded together by an epoxy. To understand the thermal conductivity of these components, first the M-19 needs to be understood. The thermal conductivity of the iron is temperature dependant and M-19 electrical steel is no exception, however there is little literature to consult for the thermal properties of M-19. However, Touloukian (1967), provides the thermal conductivity at high temperatures (above 100°C) for a 2.78% silicon steel, very nearly the silicon content of M-19, given to be 2.75% by Sprague (2009). The

values from Touloukian (1967) provide a thermal conductivity of 24.7 W/m·K at 100°C and one can extrapolate a thermal conductivity of 22.8 W/m·K at room temperature, as seen in Figure 2-8. This agrees with data from Staton et al. (2005) which shows that as the silicon content increases the thermal conductivity decreases, and at 2.75% silicon it is approximately 24 W/m·K.

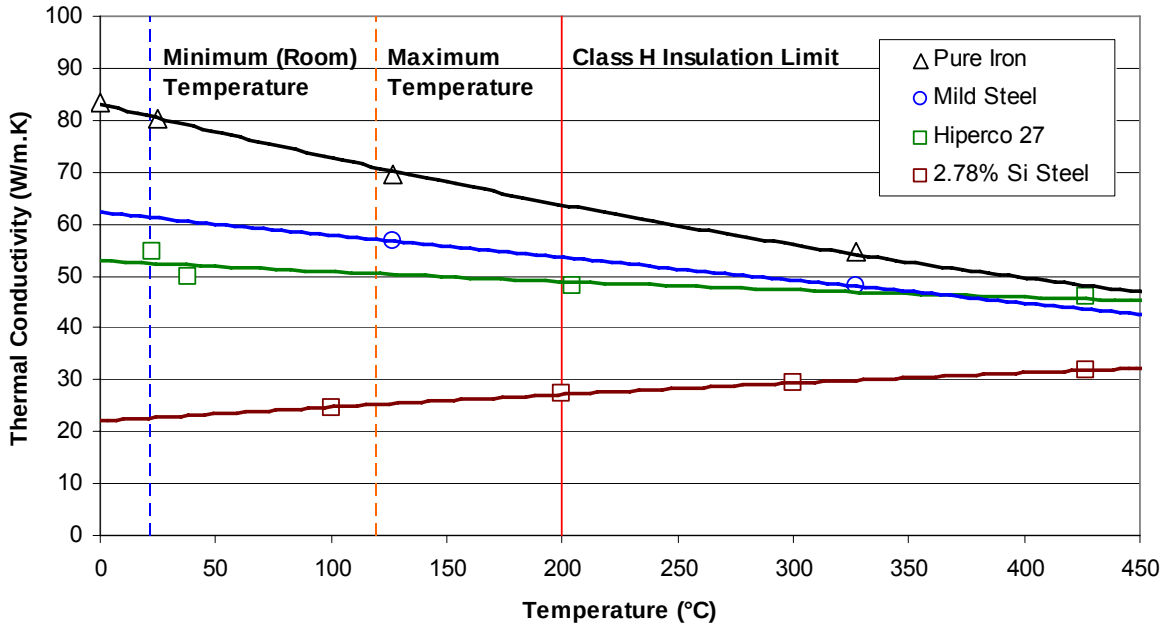

Figure 2-8: Temperature dependant thermal conductivities of pure iron, mild steel, and two electrical steels, from Incropera and DeWitt (2002), Valentich (1965), and Touloukian (1967),

The thermal conductivity is nearly constant in the expected temperature range, 22°C to 180°C, so an average or representative value of thermal conductivity can be chosen. A value of 24 W/m·K is chosen, which will be most accurate in the temperature range of 60-100°C.

The stator and fieldbooster are both anisotropic, consisting of layers of iron stacked in the axial direction. The highly conductive and continuous nature of the material in the radial and circumferential directions causes the thermal conductivity to be greater than in the axial direction, where the highly conductive laminations alternate with layers of lower conductivity epoxy. The stacking factor n_s represents the ratio of iron volume to the total volume of the stator or rotor, and can be expressed as

$$n_s = \frac{nt}{h}, \tag{2-18}$$

where n is the number of laminations of thickness t, and h is the total stator height. It can be seen that n_s cannot exceed unity, therefore for a unit height, there will be a height n_s of iron and (1 - n_s) of the inter-lamination fill material (epoxy). To determine the equivalent, or lumped thermal conductivity in the radial direction, consider the model of heat flow shown in Figure 2-9.

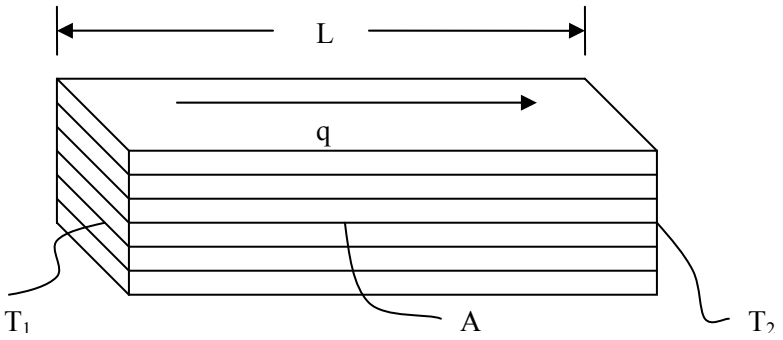

Figure 2-9: Model of Radial Heat Flow in Laminated Stator or Rotor

If the end faces are considered to be at uniform temperatures T1 and T2, then a quantity of heat proportional to the thermal conductivity and area will flow. Looking at a smaller scale, a certain quantity of heat will flow through the iron while a smaller quantity flows through the epoxy since the temperature gradient is constant but the normal areas and thermal conductivities are different. For the arbitrary geometry chosen, it can be observed that the total area of iron is equal to the product of the total area A and the stacking factor n_s, while the total area of epoxy is simply the difference of that quantity from A. Since parallel resistances can be moved arbitrarily, the series of several epoxy and iron resistances can be added into one large resistance for each, which can be seen in Figure 2-10.

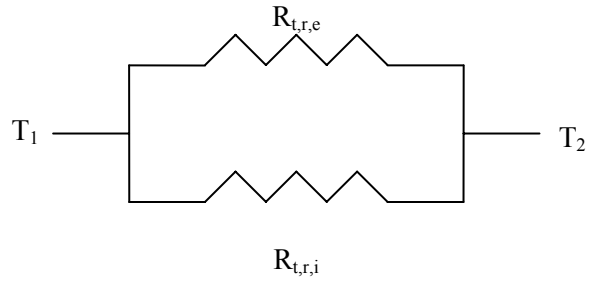

Figure 2-10: Equivalent Resistive Circuit Diagram of Heat Flow in Radial Direction of Laminations

The radial thermal resistances of the epoxy and iron, $R_{t,r,e}$ and $R_{t,r,i}$ respectively, are therefore

$$R_{t,r,e} = \frac{L}{k_e A(1-n_s)}, \tag{2-19}$$

$$R_{t,r,i} = \frac{L}{k_i A n_s}, \tag{2-20}$$

where k_e and k_i are the thermal conductivities of the epoxy and iron respectively. Since parallel resistances add by the relationship

$$\frac{1}{R_t} = \sum_{n=1}^{m} \frac{1}{R_{t,n}}, \tag{2-21}$$

the inverse of the thermal resistance is therefore

$$\frac{1}{R_{t,r}} = \frac{k_e A(1-n_s)}{L} + \frac{k_i A n_s}{L}. \tag{2-22}$$

For modelling purposes, it is impractical to model each lamination individually, therefore one can define an equivalent thermal conductivity k_{eq} by the relationship

$$\frac{A k_{eq}}{L} = \frac{1}{R_t}. \tag{2-23}$$

it can be seen that the equivalent thermal conductivity is

$$k_{eq,r} = k_i n_s + k_e(1-n_s), \tag{2-24}$$

a result which is valid for cylindrical or rectangular geometries. In motor manufacturing, it is ideal to have a stacking factor close to unity to maximize the iron volume and thus strengthen

the generated magnetic field. The stacking factor of the prototype motor is approximately 95%, and the thermal conductivities of the M-19 and the epoxy, 3M™ Scotch Weld™ 2290, are 24 W/m·K and a nominal 0.3 W/m·K respectively, as per Thompson (2009). Using (2-24), the equivalent thermal conductivity in the radial direction can be found to be 22.815 W/m·K. Because of the low thermal conductivity of the epoxy coupled with its low area, equation (2-24) could be simplified to be

$$k_{eq,r} \cong k_i n_s , \tag{2-25}$$

a function of only the iron thermal conductivity and the stacking factor, with a difference on the order of 0.1%. The advantage of this simplification is that knowing the exact thermal conductivity of the epoxy is unnecessary to achieve an accurate equivalent thermal conductivity.

The most noticeable difference between the transverse and radial thermal conductivities is that now the thermal resistances are in series, rather than parallel, the reason for which can be seen in Figure 2-11. Instead of continuous media spanning the length of the volume, thin layers of laminations and epoxy alternate along the length. For a given length L, the length of iron will be the product of L and n_s, and the length of epoxy will be the difference of the iron length from the total.

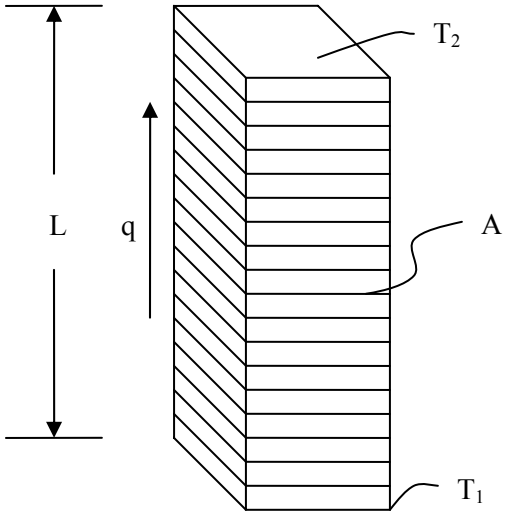

Figure 2-11: Model of Transverse Heat Flow in Laminated Stator or Rotor

The other significant difference is that because of the discontinuous nature of the material, imperfections introduced in manufacturing will cause a thermal contact resistance between layers. Ideally, the epoxy perfectly coats each layer and when the stator is consolidated there are no voids, however in practice this is difficult if not impossible to achieve. Unfortunately, contact resistance is difficult to predict, and it is dependant upon many factors: roughness of lamination material, pressure of contact between laminations, fill material, and presence of air bubbles in the interface. For modelling of the prototype motor, a value of this contact resistance can be predicted from the literature.

A new resistance circuit diagram can be constructed for the transverse case, which can be seen in Figure 2-12.

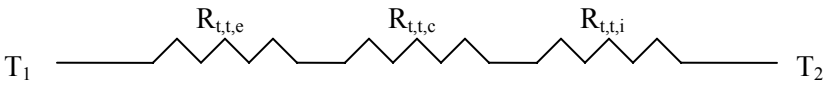

Figure 2-12: Equivalent Resistive Circuit Diagram

The transverse thermal resistances of the epoxy and iron, $R_{t,t,e}$ and $R_{t,t,i}$ respectively, are

$$R_{t,t,e} = \frac{L(1-n_s)}{k_e A}, \tag{2-26}$$

$$R_{t,t,i} = \frac{Ln_s}{k_i A}, \tag{2-27}$$

while $R_{t,t,c}$ represents the total thermal contact resistances along the length L which is to be determined. Series resistances add by

$$R_t = \sum_{n=1}^{m} R_{t,n}, \tag{2-28}$$

which results in a total thermal resistance of

$$R_{t,t} = \frac{L(1-n_s)}{k_e A} + \frac{Ln_s}{k_i A} + \frac{(n-1)R''_{t,t,c}}{A}, \tag{2-29}$$

where n represents the total number of laminations along the length L, which is equivalent now to the height h of the stator. Using the equivalent thermal conductivity equation (2-23) and rearranging, the equivalent transverse thermal conductivity can be found to be

$$k_{eq,t} = \frac{k_e k_i}{k_e n_s + k_i (1 - n_s) + (n-1)\dfrac{k_e k_i R''_{t,t,c}}{h}}. \qquad \textbf{(2-30)}$$

The strong dependence of the equivalent thermal conductivity upon the contact resistance can be seen in Figure 2-13. For a precise solution, the transverse thermal conductivity should be included in the model. Staton et al. (2005) suggest basing contact resistance on the air gap between materials, and suggest values from Janna (1988) of 0.0001 mm for a smooth mirror finish, or 0.023 mm for a rough interface. Based on these values, the thermal contact resistance will range from 3.9×10^{-6} m²K/W to 8.9×10^{-4} m²K/W, resulting in equivalent conductances of 4.61 W/m·K and 0.371 W/m·K, respectively. This is a wide range of values, separated by an order of magnitude. As a result the transverse thermal conductivity of iron laminate components will undergo a sensitivity analysis in Section 5.5.

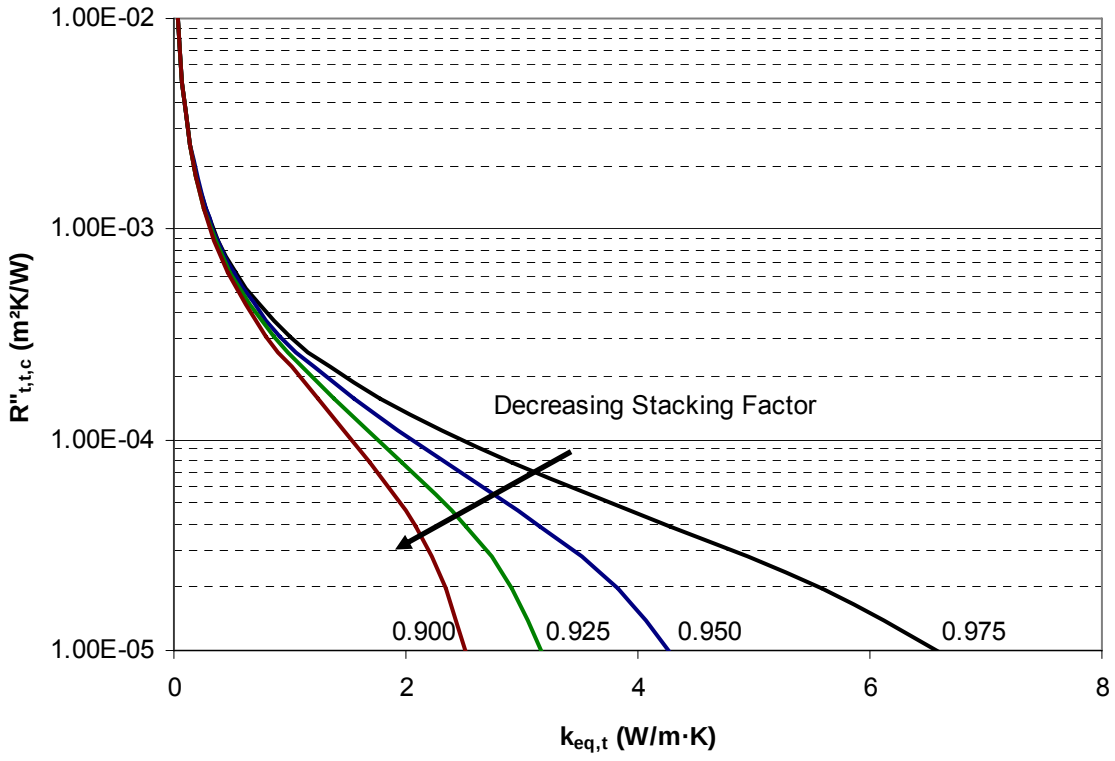

Figure 2-13: Effect of contact resistance and stacking factor on equivalent thermal conductivity of iron laminate components

2.3.2 Equivalent Thermal Conductivity of Windings

Trigeol et al. (2006) note that accurate modelling of the windings is of significant importance to a motor's thermal model because they represent the largest source of heat and are the warmest point in the motor. In fact, the entire thermal response hinges upon the accurate modeling of these components. Thermal modeling of the windings is more complicated than most components of a motor because of their composite nature. Windings are formed of layers of copper wire covered in an enamel which provides a dielectric barrier between turns, preventing short circuits. Because copper is continuous along the length of the wire but is interrupted by the enamel in the normal direction, the windings are anisotropic and the thermal conductivities in the axial and radial directions will not be equal; values for both will be required for the thermal model. In order to determine the thermal conductivities of the windings a geometric approach will be taken.

Based on linearly interpolated thermal conductivities based on the tabulated values of Incropera and DeWitt (2002), the thermal conductivity of pure copper ranges from 403 W/m·K at 20°C to 389 W/m·K at 180°C, which is the highest of any material in the motor. Over the temperature range of interest the thermal conductivity decreases by a maximum of 3.6%, however because of the elevated temperatures expected, the thermal conductivity at 100°C, 396 W/m·K will be used, which will lead to a maximum error of 2%.

According to Staton et al. (2006), even precision-made windings such as those in the prototype motor do not require that each conductor be modeled to determine an accurate thermal distribution; rather a lumped approach can be taken. Several models exist to determine an equivalent thermal conductivity. Lussier et al. (2003) take both analytic and finite element approaches towards obtaining equivalent thermal conductivity and observed a strong dependence on the material between windings. Staton et al. (2005) and Boglietti et al. (2008) simulate the random layering of windings by using a model which is comprised of concentric cylinders which alternate between copper and enamel. In this approach, each layer is considered in the model and is allowed to have its own temperature, enabling the model to give a much better representation of the temperature difference between the inside and outside of the winding. This is the approach to be taken in the development of this thermal

model. As a result, the radial thermal conductivity will be that of pure copper rather than an equivalent which includes the enamel. The enamel portion will be considered as a thermal resistance which will be based on an assumed thickness between 10 and 100 μm. Boglietti et al. (2005) perform a sensitivity analysis for the impregnation goodness parameter in their model, which found that changes of -80% and +100% in the parameter resulted in changes of +8.26% and -3.66% in the maximum temperature. This will likewise be investigated in this model.

For the lengthwise thermal conductivity of the copper, the equivalent thermal conductivity

$$k_{cu,z,eq} = k_{cu} n_c + k_e (1 - n_c), \tag{2-31}$$

can be used, where

$$n_c = \frac{A_{wire}}{A_{wire} + A_{fill}} = \frac{d^2}{(d+w)^2}. \tag{2-32}$$

If the spacing of 10 to 100 μm is again considered, equivalent lengthwise conductivities ranging from 364 to 393 W/m·K result. Arbitrarily choosing a spacing of 50 μm gives a value of 379 W/m·K. It should be noted that this spacing gives a copper packing factor of 0.96.

2.3.3 Summary of Thermal Conductivities

All parts other than the stator, fieldbooster and coils are isotropic, and therefore their thermal conductivities can simply be found in the literature.

The flexispline, diaphragm and spur gear are composed of 4340 steel. Between the coils and these components there are several thermal barriers or a large air gap, so it can be assumed that the temperature of these components is only approximately 10°C to 20°C above ambient, therefore a thermal conductivity at room temperature from thermal properties lieterature can be used. The 4340 steel in the prototype motor is quenched and tempered, and a thermal conductivity of 44.5 W/m·K from MatWeb (2009c) was used.

The shaft is constructed of 1045 steel. A thermal conductivity of 49.8 W/m·K was suggested by MatWeb (2009b), however this value is stated as being for “typical steel”. Looking at the value for 1040 steel, which has a similar composition, MatWeb (2009a) had

temperature dependant data from 0°C to 1200°C. In the temperature region of interest, the thermal conductivity ranges from 51.9 W/m·K at 0°C to 50.7 W/m·K at 100°C. Because the shaft is likely to be warm, but not to the extent of the coils, if a temperature of 50°C is assumed, a linear interpolation yields a thermal conductivity of 51.3 W/m·K.

The manifold component is constructed of 6061-T6 aluminum, and is located between the stator and the air, so the temperature can be assumed to be closer to the ambient temperature than the peak temperature. According to Incropera and DeWitt (2002), the listed aluminum alloys have high and fairly constant thermal conductivity at higher temperatures, so the representative value of thermal conductivity of 167 W/m·K from MatWeb (2009d) can be used.

Around the fieldbooster is a thin coating of a material that will modeled as a soft rubber, with a thermal conductivity of 0.13 W/m·K taken from Incropera and DeWitt (2002). The epoxy used on the stator assembly is a Duralco 4525 electrically resistant epoxy, with a thermal conductivity of 1.88 W/m·K, given by Cotronics Corporation (2009).

Table 2-1: Summary of Thermal Conductivities

Material	Thermal Conductivity	Source	Comment
Alloy Steel (4340 P/H)	$k =$ 44.5 W/m·K	[45]	
Carbon Steel (AISI 1045)	$k =$ 51.3 W/m·K	[43], [44]	As 1040 Steel at 50°C
Aluminum (6061-T6)	$k =$ 167 W/m·K	[46]	
Thin Coating	$k =$ 0.13 W/m·K	[34]	As soft rubber
Epoxy	$k =$ 1.88 W/m·K	[18]	
M-19	$k_r = k_\theta =$ 28.5 W/m·K $k_z =$ 2.00 W/m·K	[72], [79]	
Copper	$k_r = k_\theta =$ 20 W/m·K $k_z =$ 379 W/m·K	[34]	

2.4 Convective Heat Transfer Coefficients

Surrounding and within the motor is air which will be heated as the temperature of the motor increases, and serves as a sink for the heat generated by the motor. The air will be set in motion in one of two ways: free convection caused by temperature gradients inducing the less dense warm parcels of air to rise relative to the colder parcels, or forced convection by a fan or high pressure air line. Free convection will always be the case for the outside of the motor in laboratory testing, however future applications may have the motor sitting in a high air speed flow. The interior air of the motor will always be in motion due to the geometry and the inevitable temperature gradients. When there is no forced air into the motor the result will be free convection, and when there is a forced airflow into the motor the forced convection dominates the effects of buoyancy.

In a CFD model, the governing equations of fluid motion and energy transfer are solved directly, however in a simplified model convection can be incorporated through the use of a convection coefficient h at a surface, which govern heat transfer based on Newton's law of cooling,

$$q''_{conv} = h\left(T_s - T_\infty\right), \tag{2-33}$$

where q''_{conv} is the heat flux from a surface at temperature T_s to surrounding air at temperature T_∞. In seeking an analytic solution for the heat removed by convection, several complexities arise. The first is the irregular geometry. Traditional motors feature thin air gaps, and stators and rotors that can be modeled as concentric hollow cylinders, leading to simple and accurate analytic solutions which cannot be employed here. The second, and most challenging problem with finding an analytic result is that in the case of forced convection, above a critical flow rate of cooling air into the motor the flow becomes turbulent. The combination of turbulence and complex geometry means that the optimal approach for internal forced convection may be through a numerical approach, similar to that used by Trigeol et al. (2006) or Staton and Cavagnino (2006). Convection correlations can be used as a starting point, however, particularly for the case of free convection. Boglietti et al. (2005) base free

convective heat transfer coefficients on dimensional analysis, then multiply by an experimentally determined factor to match their model to the data.

Another approach to internal convection is based on experimental results. Staton et al. (2005) note that many authors provide correlations for convection of the form

$$h = k_1(1 + k_2 v^{k_3}), \tag{2-34}$$

for the end space of motors, where k_1 represents the natural convection coefficient which is shown to be as high as 40 W/m²K in the cases they examine. For forced convection, they find convection coefficients as high as 120 W/m²K with an average airspeed of 20 m/s.

2.4.1 Convective Modeling of Interior Air

The behaviour of the internal air is complicated. Heat generated in the coils and stator will warm the adjacent air, causing it to rise while regions of cooler air fall. The spur gear features large holes which permit air to enter or leave the inside of the motor. In the case of free convection, air will likely enter and leave through these holes, however when cooling air is forced in through the holes in the shaft the air will exit through the holes in the spur gear. Because of the irregular geometry around the stator and coils, analytic modelling of the precise air-flow is difficult. A simplified approach may be taken to find convection coefficients which will provide a good starting point for the model.

In order to find the convection coefficient h for a surface, convection correlations from heat transfer literature can be employed. These correlations provide the dimensionless Nusselt number Nu, which is defined as

$$Nu = \frac{hL}{k}, \tag{2-35}$$

and is stated by Incropera and DeWitt (2002) to represent the dimensionless temperature gradient at the surface, and can be used to find h. For a laminar flow, the Nusselt number is constant, its value depending on whether the surface is at a constant temperature, or whether the heat flux from the surface is constant. For laminar flow in a tube with a uniform surface temperature, Incropera and DeWitt (2002) state that

$$Nu = 3.66\,. \tag{2-36}$$

For turbulent flow, the Nusselt number is a function of the Reynolds and Prandtl numbers, as well as the friction factor *f*, itself a function of the Reynolds number, roughness ε and hydraulic diameter D_h, hence

$$Nu = Nu\left(\mathrm{Re}, \mathrm{Pr}, f\right). \tag{2-37}$$

Incropera and DeWitt (2002) state that an approximation of the convective heat transfer coefficients can be made by employing the hydraulic, or effective diameter of an irregular geometry, defined by

$$D_h = \frac{4A_c}{P_w}\,. \tag{2-38}$$

where A_c is the cross sectional area and P_w the wetted perimeter of the flow. Using this effective geometry, one can employ correlations from heat transfer literature to find the Nusselt number. For turbulent flow, Gnielinski (1976) suggest the equation

$$Nu = \frac{\left(f/8\right)\left(\mathrm{Re}_{D_h} - 1000\right)\mathrm{Pr}}{1 + 12.7\left(f/8\right)^{1/2}\left(\mathrm{Pr}^{2./3} - 1\right)}. \tag{2-39}$$

which is valid for $0.5 < Pr < 2000$ and $3000 < \mathrm{Re}_{D_h} < 5\times10^6$. Haaland (1983) give the friction factor by the equation

$$f = \left(-1.8\log\left[\frac{6.9}{\mathrm{Re}_{D_h}} + \left(\frac{\varepsilon/D_h}{3.7}\right)^{1.11}\right]\right)^{-2}, \tag{2-40}$$

The roughness of many materials and surface finishes can be found in fluid mechanics literature, but for many of the irregular surfaces of the inside of the prototype motor, the roughness can be geometrically obtained, for example by the lamination thickness of the M-19 components or the wire thickness for the faces of the windings.

2.4.2 External Free Convection

Free convection is one mechanism by which heat leaves the surface of the motor and spreads to its surroundings when there is no active cooling. The thermal resistance formed by the boundary layer acts as the final thermal barrier between the motor and the ambient air.

In natural convection, the heat transfer is governed by the buoyancy, and the dimensionless Rayleigh number *Ra*, which is equal to

$$Ra_x = \frac{g\beta(T_s - T_\infty)x^3}{\nu\alpha}. \quad \textbf{(2-41)}$$

where x represents a geometric parameter such as length L or diameter D. As stated by Arpaci and Larsen, (1984), the Rayleigh number represents the ratio of buoyant force to the change in momentum flux, and in natural convection flows determines the onset of turbulence, similar to the Reynolds number for forced flows. The Rayleigh number is equal to the product of the Grashof number *Gr* and Prandtl number *Pr*,

$$Ra_x = Gr_x Pr, \quad \textbf{(2-42)}$$

where the Grashof number Gr represents the ratio of buoyancy to viscous forces acting on a fluid, which is given by the equation

$$Gr_x = \frac{g\beta(T_s - T_\infty)x^3}{\nu^2}, \quad \textbf{(2-43)}$$

and the Prandtl number Pr, a fluid property given by

$$Pr = \frac{\nu}{\alpha}, \quad \textbf{(2-44)}$$

which represents the ratio of momentum to thermal diffusivities. The expected Rayleigh number was calculated to be on the order of $10^5 < Ra < 10^7$ for any orientation, which corresponds to a temperature rise between 1°C and 100°C.

For free convection, the Nusselt number *Nu* is a function of the Rayleigh and Prandtl numbers, however the relation is dependant upon the geometry to be considered. There are two primary orientations of the motor to be considered, horizontal and vertical. Because of the regular, cylindrical shape of the outside of the motor, the convection coefficient can be found based on convection correlations.

For the horizontal case, in a model that considers the surface to be at uniform temperature, the average Nusselt number can be found using the correlation of Churchill and Chu (1975)

$$\overline{Nu_D} = \left[0.60 + \frac{0.387 Ra_D^{1/6}}{\left(1 + \left(0.559/\mathrm{Pr}\right)^{9/16}\right)^{8/27}} \right]^2, \tag{2-45}$$

which is valid for the wide range $10^{-5} < Ra < 10^{13}$. For the vertical case, each surface has its own correlation. The bottom of the motor can be modelled as a hot surface facing downwards, in which case

$$\overline{Nu_L} = 0.27 Ra_L^{1/4}, \tag{2-46}$$

from Incropera and DeWitt (2002) can be used when $10^5 \lesssim Ra_L \lesssim 10^{10}$, where

$$L \equiv \frac{A_s}{P}, \tag{2-47}$$

is the recommended characteristic length to improve accuracy. For the top surface of the motor Incropera and DeWitt (2002) recommend

$$\overline{Nu_L} = 0.54 Ra_L^{1/4}, \tag{2-48}$$

also based on the characteristic geometry given by (2-47), and with validity for $10^4 \lesssim Ra_L \lesssim 10^7$. For the vertical cylindrical face, Incropera and DeWitt (2002) recommend a correlation from Churchill and Chu (1975b),

$$\overline{Nu_L} = 0.68 + \frac{0.670 Ra_L^{1/4}}{\left[1 + \left(0.492/\mathrm{Pr}\right)^{9/16}\right]^{4/9}}, \tag{2-49}$$

for $Ra_L \lesssim 10^9$, so long as the boundary layer is much thinner than the cylinder. Sparrow and Gregg (1956) demonstrated that the free convection correlations for vertical plates, (2-49), can be applied to cylindrical shapes, so long as the condition

$$\frac{D}{L} \gtrsim \frac{35}{Gr_L^{1/4}}, \tag{2-50}$$

is met, which for the given geometry will be true when the temperature difference between the cylinder and the quiescent air is greater than 10°C.

The Rayleigh number *Ra* exhibits strong dependence upon the kinematic viscosity *v* and thermal diffusivity α of air. In addition, the Nusselt number *Nu* is strongly dependant upon their ratio (the Prandtl number *Pr)* and the convective heat transfer coefficient will require the thermal conductivity *k* of air. It can be seen in Incropera and DeWitt (2002) that all of these thermophysical properties of air vary significantly with temperature, therefore the thermal model will incorporate functions to allow each value to be precisely determined at a given temperature. Based on the values tabulated by Incropera and DeWitt (2002), CurveExpert 1.3 was used to develop the following quadratic curve fits based on temperatures in degrees Celcius,

$$\alpha_{air} = (1.884 \times 10^{-5}) + (1.338 \times 10^{-7}) \cdot T + (1.464 \times 10^{-10}) \cdot T^2, \quad \textbf{(2-51)}$$

$$k_{air} = (2.414 \times 10^{-2}) + (7.914 \times 10^{-5}) \cdot T - (2.714 \times 10^{-8}) \cdot T^2, \quad \textbf{(2-52)}$$

$$\nu_{air} = (1.341 \times 10^{-5}) + (9.004 \times 10^{-8}) \cdot T + (9.643 \times 10^{-11}) \cdot T^2, \quad \textbf{(2-53)}$$

2.4.3 Internal Free Convection

For the internal air, the contribution of free convection to the total heat transfer will be modeled based on geometry, namely the orientation of surfaces with respect to the air around it. As a first approximation, the effect of the enclosure and proximity of surfaces will be neglected, and the equations used for the external free convection will be used. For vertical surfaces, equation (2-49) can be employed, for hot surfaces facing downwards equation (2-46) will be used, and for hot surfaces facing upwards equation (2-48) will be used.

2.5 Thermal Radiation Modelling

Thermal radiation is an important mode of heat transfer in motors where large temperature differences between surfaces drive high rates of heat transfer. The rate of heat flux emitted by a blackbody (an ideal emitter and absorber of radiative thermal energy) at a temperature *T* in kelvin is governed by the Stefan-Boltzman law,

$$E_b = \sigma T^4, \tag{2-54}$$

as stated in Incropera and DeWitt (2002), where σ is the Stefan-Boltzmann constant, $5.67 \times 10^{-8} \ W/m^2K^4$. The radiative heat flux emitted by a real surface is less than that emitted by a blackbody, and is given by

$$q''_{rad} = \varepsilon E_b = \varepsilon \sigma T^4, \tag{2-55}$$

where ε represents the emissivity of a surface, a value between zero and unity. Because radiation occurs between surfaces the ability of one surface to see another, or view factor, plays an important role in any thermal network consisting of multiple surfaces.

There are two important categories of radiation heat transfer in a motor: surface-to-ambient, and surface-to-surface. Surface-to-ambient occurs from the external faces of components to the surroundings, which can be assumed to be of uniform and constant temperature, such as the walls of a laboratory. This mode of heat transfer combines with free convection to control the external temperature, and ultimately the combined heat transfer from these two modes must equal the thermal generation rate less the heat carried away by forced convection if steady state is to be reached. The most important surface-to-surface radiation occurs between the warm coils and the surrounding components.

It was observed by Boglietti et al. (2005) that radiation is important for accurate results at low rotational speeds, where the mass flow rate of cooling air is also low and convective cooling is reduced, however it is important in all cases for a highly accurate solution. Because of the complicated and non-linear nature of radiation, it is desirable to simplify the way radiation is accounted for in the model. One such approach to simplification, according to Arpachi et al. (1999), is to linearize the Steffan-Boltzmann law by defining a radiative heat transfer coefficient which will compliment the convective heat transfer coefficient, an approach taken by Boglietti et al. (2008). The two most important properties required for successful radiation modeling are the emissivity of a material and the view factor from one surface to another.

2.5.1 Summary of Emissivities

Emissivity is a surface property which is influenced by its finish, for example polish or oxidation. Even when the material is well known, there is still a high degree of uncertainty regarding this property, a reason why this parameter is investigated in sensitivity analyses such as the one performed by Boglietti et al. (2005).

There are a limited number of materials used to construct the motor, however what is more important than the materials for radiation is the surface finish. For example, the stator has every surface with the exception of the tooth face painted, meaning that an emissivity is required for the paint, as well as for the bare material. Table 2-2 summarizes the materials used in the prototype motor and the chosen representative emissivities

Table 2-2: Emissivities of selected electric motor materials

Material	Emissivity		Notes and References
	Range	Chosen	
1045, 4340 Steel	0.4-0.5	0.45	Based on "Steel Shaft" [80]
6061-T6 Aluminum	0.1-0.11	0.11	Based on oxidized aluminum [62], "housing aluminum" [80]
Coils	0.9	0.9	Based on various paints [13], "Impregnation Resin" [80]
M-19 (Painted)	0.9-0.98	0.9	Based on various paints [13] , [34]
M-19 (Bare)	0.6	0.6	Based on "Stator Iron" [80]
Thin Coating	0.86	0.86	As "Soft Rubber" [13]

2.5.2 Thermal Radiation View Factors

Incropera and DeWitt (2002) state that the exact view factor is given by

$$F_{ij} = \frac{1}{A_i} \int_{A_i} \int_{A_j} \frac{\cos\theta_i \cos\theta_j}{\pi R^2} dA_i dA_j , \qquad \textbf{(2-56)}$$

however there are many geometries that are commonly encountered for which simplified view factor equations exist. In addition to these equations, symmetry, intuition, and the reciprocity relationship which follows from (2-56), given by Incropera and DeWitt (2002) to be

$$A_i F_{ij} = A_j F_{ji}\,, \tag{2-57}$$

can be used to find the view factors.

An alternative approach would be to assume view factors. Due to the prototype nature of the motor and the ease of extending the model to subsequent motors, the significant view factors could be assumed or deduced. There are several view factors which can be assumed to be unity, for example from the outer face of the windings to the flexispline.

2.5.3 External Thermal Radiation

A motor can be assumed to be small with respect to its surroundings. If the exterior motor surfaces are assumed to be grey, the rate of heat transfer from surface 1 or the motor to the surroundings is given by

$$q_{rad,1\to surr} = \sigma\,\varepsilon\,A_1(T_1^4 - T_{surr}^4)\,, \tag{2-58}$$

from which the radiative heat transfer coefficient $h_{rad,ext}$ can be found by

$$h_{rad,ext} = \sigma\,\varepsilon_1\left(T_1 + T_{surr}\right)\left(T_1^2 + T_{surr}^2\right), \tag{2-59}$$

or

$$h_{rad,ext} = 4\sigma\,\varepsilon_1\,T_1^3\,, \tag{2-60}$$

if T_1 is nearly equal to T_{surr}.

2.5.4 Internal Thermal Radiation across Thin Gaps

The thermal radiation exchange between two diffuse, gray surfaces of areas A_1 and A_2, emissivities ε_1 and ε_2, uniform temperatures T_1 and T_2 and which form an enclosure can be found from

$$q_{rad,1\to 2} = \frac{\sigma(T_1^4 - T_2^4)}{\frac{1-\varepsilon_1}{\varepsilon_1 A_1} + \frac{1}{A_1 F_{12}} + \frac{1-\varepsilon_2}{\varepsilon_2 A_2}}, \tag{2-61}$$

where F_{12} is the view factor from surface 1 to surface 2. In such a two surface enclosure, all the radiative energy sent from one surface is received by the other. Equation (2-61) can be linearized in order to make it more compatible with thermal modelling, resulting in a radiative heat transfer coefficient of

$$h_{rad} = \frac{\sigma(T_1 + T_2)(T_1^2 + T_2^2)}{\frac{1-\varepsilon_1}{\varepsilon_1} + \frac{1}{F_{12}} + \frac{1-\varepsilon_2}{\varepsilon_2}\left(\frac{A_1}{A_2}\right)}. \tag{2-62}$$

Because of the extensive symmetry on the inside of a motor, there are several instances where this relationship is precise, and others where a two-surface enclosure can be assumed. Scowby et al. (2004) recognize the applicability of (2-61) to motor modelling. There are several instances where a two-surface enclosure can be assumed inside the motor, highlighted in Figure 2-14. The height of the stator core relative to the entire internal cavity, coupled with the thinness of the airgap, creates an enclosure with a very high aspect ratio, that is the height and width are both significantly greater than the thickness. This high aspect ratio effectively forms a two surface enclosure as almost all the radiative energy sent from the outer faces of the stator tooth and the windings is received by the flexispline. For such a situation, the view factor from the stator tooth face or winding face to the flexispline is unity, however the reverse is less due to the different surface areas. Because of the symmetry of the motor when rotating, adiabats can be drawn at 22.5° intervals, as seen in Figure 2-14, dividing the motor into one-sixteenth sections. Because no heat crosses an adiabat, all the radiation leaving two surfaces of the winding goes to the flexispline, while the innermost face of the winding goes into the stator yoke.

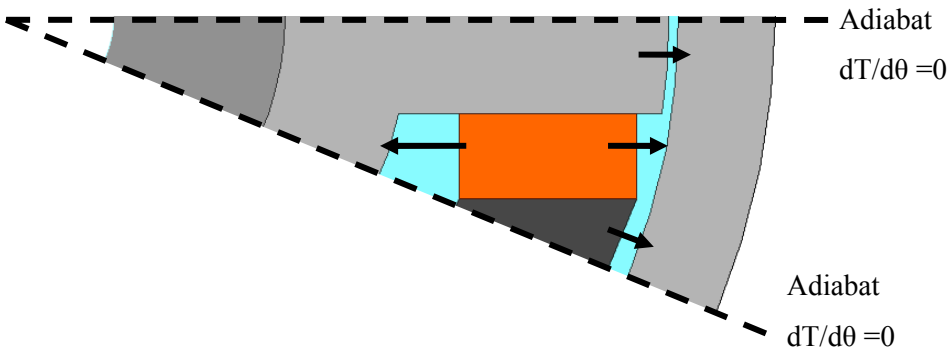

Figure 2-14: Primary radiative heat transfer paths due to symmetry in central section.

2.6 Contact Resistance

Contact resistance is one of the most difficult parameters to predict when constructing a thermal model as it depends on many factors that are difficult to control, including the surface roughness and contact pressure between surfaces, or the size of the air-gap between them. For the prototype motor, contact resistance will be significant in several interfaces: stator-shaft, shaft-manifold, manifold-flexispline, and flexispline-fieldbooster, as well as between the windings and the stator. Different models have different ways of accounting for thermal conductivity. In a finite element model, some software allows users to specify thermal resistance between domains, while others require a thin domain to be drawn between adjacent surfaces. In a lumped parameter model an additional thermal resistance is placed between two bodies. Regardless of the approach, some physical information is required to quantify the resistance.

The roughness of a surface causes small gaps at the contact interface which can be filled with air, thermal paste, or even a vacuum. These small pockets form a thin layer between two bodies which can be characterized by the root-mean-squared roughness of the materials. One approach to estimating contact resistance uses this roughness and the thermal conductivity of the medium between to estimate the contact resistance. Another approach would be to base the thickness on design tolerances. In mechanical design parts are specified to include small gaps on the order of tens to hundreds of micrometers (thousandths of an

inch) to assist with the assembly. A common manufacturing tolerance of 0.005 inches, or 127 μm on the diameter is equivalent to a separation of 64 μm. For the thermal model of the motor, the thermal contact resistances between components will be based on this separation, however the sensitivity of the model to this parameter will be analyzed. The maximum contact resistance between components can be determined analytically by

$$R''_{t,c} = \left[\frac{k_{air}}{\delta} + h_{rad} \right]^{-1}, \tag{2-63}$$

where δ is separation, between two components. Based on the design tolerance of 64 μm, surface temperatures of 300 K and an emissivity of 0.6, which corresponds to M-19, the thermal contact resistance is 2.439×10^{-3} m²K/W. Comparing this to the thermal contact resistances listed by Staton et al. (2005), it can be seen that this value is higher by an order of magnitude, therefore the sensitivity analysis for thermal contact resistance will focus on values below 2.5×10^{-3} m²K/W.

2.7 Thermal Capacity

Of critical importance to transient modeling is the thermal capacity of each component. The heat capacity of each component, together with its conductivity, dictates the speed of propagation of heat from the source to the sink. The heat capacity of an object is defined as the product of its mass and specific heat, therefore having appropriate values for both is of considerable importance. For some materials, the temperature dependence of the density and specific heat needs to be known such that this dependence can be incorporated into a model, or such that representative values at appropriate temperatures can be chosen for simplified models.

2.7.1 Summary of Densities

The only substance involved in the thermal analysis of the prototype motor which exhibits a significant change in density in the temperature range considered is the air. In a CFD simulation, accounting for the changing density of gasses enables buoyant flow, and thus heat transfer by free convection. In this case, the CFD solver has a built in method of

accounting for the density change, either by the ideal gas law or through a look-up table. The variation of the density of air with respect to temperature is shown in Figure 2-15. The air temperature will change significantly depending on location within or outside the motor, but for thermal storage considerations, the heat capacity of air is very low because its density is extremely low compared to the density of the solid components, notably the numerous steel components. For this reason, a value of 1.05 kg/m³ can be used with negligible impact on the overall result for non-CFD-based analyses.

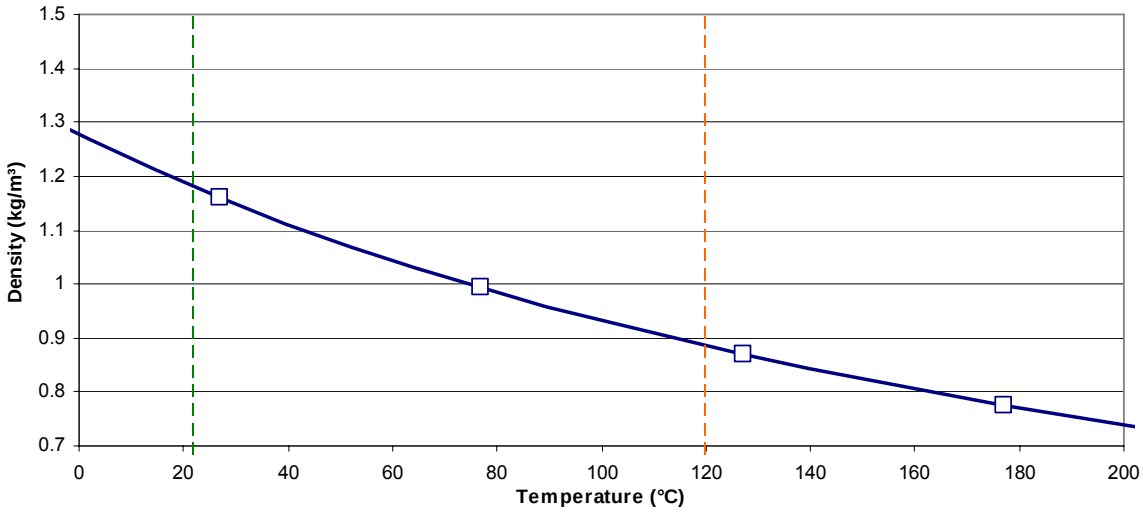

Figure 2-15: Density of air with respect to temperature, from Incropera and DeWitt (2002)

While the densities of the other materials do not exhibit temperature dependence, the M-19 and Copper components do have reduced densities which result from their composite nature. The equivalent density of the M-19 components behaves the same as its radial thermal conductivity, equation (2-24), and can be found using

$$\rho_{M-19,eq} = \rho_{M-19} n_s + \rho_{epoxy}(1 - n_s)\,. \qquad \textbf{(2-64)}$$

The density of M-19 is given by AK Steel (2007) to be 7650 kg/m³, and the stacking factor n_s is 0.95. The density of the epoxy used, 3M Scotch-weld 2290 epoxy is not given by 3M (2004), however Avallone and Baumeister (1996) gives a range of specific gravities of 1.11 to 1.40 for an unfilled casting resin or compound, which equates to a density between 1110

kg/m³and 1400 kg/m³. Using these values, equivalent densities of 7323 kg/m³ and 7337.5 kg/m³ can be found. Based on these values, an average density of 7330 kg/m³ was selected.

The density of copper given by Incropera and DeWitt (2002) is 8933 kg/m³, however the copper does not occupy the entire volume of the coils. The density of the coils can be found similarly to the density of the M-19 components, and is given by

$$\rho_{coils} = \rho_{cu,eq} = \rho_{cu} n_c + \rho_{epoxy}(1 - n_c), \quad \textbf{(2-65)}$$

If the epoxy density used for the M-19 components is again used, using the coil packing factor of 0.96 found in section 2.3.2, the density of the coils is found to be 8616 kg/m³.

The densities of the remaining materials can be found in various literature, and are summarized with the other materials in Table 2-3.

Table 2-3: Summary of densities of motor materials

Material	Density (kg/m³)	Source(s)	Comment
Air	1.05	[34]	Value at 60°C
Copper	8616	[6] , [34]	Equivalent
Thin Coating	1100	[34]	As soft rubber
Epoxy	1900	[18]	
6061-T6 Aluminum	2700	[46]	
M-19	7330	[2] , [6]	Equivalent
1045 Steel	7850	[44]	
4340 Steel	7850	[45]	

2.7.2 Summary of Specific Heats

While the specific heat of a material is temperature dependant, it is useful to consider its value to be constant. For the materials comprising and fluids surrounding the prototype motor, it can be demonstrated that there is insignificant change in this material property.

Beginning with the surrounding air, the specific heat changes from 1007 to 1014 J/kg·K between 27°C and 127°C, with a tabulated value of 1009 J/kg·K at 77°C as stated in

Incropera and DeWitt (2002). Because of the small change in value over the considered region, and the insignificance of the thermal capacity of the air, the value of 1009 J/kg·K will be used.

Over the 27°C to 127°C temperature range, the specific heat of copper ranges from 386 J/kg·K to 397 J/kg·K according to Çengel and Boles (2008) and Incropera and DeWitt (2002). Because of the high temperature of the copper in the coils, the value at 100°C, 393 J/kg·K will be used. The heat capacity of the epoxy used was not provided by the manufacturer, however a similar high temperature encapsulating and potting epoxy from MG Chemicals (2009a) has a specific heat of 1176 J/kg·K, and another, MG Chemicals (2009b), 1419 J/kg·K. If the effective specific heat is found in the same way the effective density was found, using

$$c_{coils} = c_{cu,eq} = c_{cu} n_c + c_{epoxy}(1 - n_c), \tag{2-66}$$

then specific heats of 424 J/kg·K and 434 J/kg·K can be found. Since this is representative of a large range of c_{epoxy}, an average value of 429 J/kg·K can be taken and should be accurate. For the Duralco 4525 epoxy used on the stator, the average value of 1300 J/kg·K will be used.

For M-19, an approach similar to that for the coils can be taken. From Touloukian (1967), specific heats over 100°C are available, and plotted in Figure 2-16. Extrapolating this data, a value of 505 J/kg·K can be found at 75°C, which is quite comparable to the values of the specific heat for 1045 steel, 486 J/kg·K from MatWeb (2009b), and 475 J/kg·K, from MatWeb (2009c) for 4340 steel. Using the equation

$$c_{M-19,eq} = c_{M-19} n_s + c_{epoxy}(1 - n_s), \tag{2-67}$$

with the previously used thermal conductivities of epoxy and the stacking factor of 0.95, specific heats of 538.6 J/kg·K and 550.7 J/kg·K can be found. An average value of 545 J/kg·K will be used.

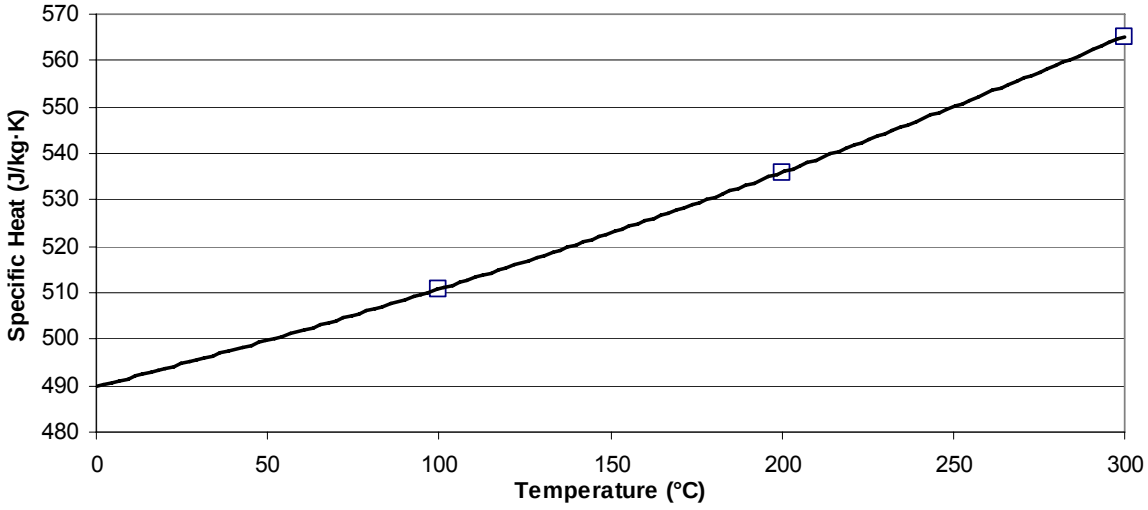

Figure 2-16: Specific heat of M-19, three data points and extrapolated curve-fit, from Touloukian (1967)

The remaining materials can simply be found in the literature. The thin coating, modeled as soft rubber, has a specific heat of 2010 J/kg·K from Incropera and DeWitt (2002). MatWeb (2009b) gives a value of 486 J/kg·K for the specific heat of 1045 Steel, the value for 4340 steel is given by MatWeb (2009c) to be 475 J/kg·K, and that of 6061-T6 aluminum was stated in MatWeb (2009d) to be 896 J/kg·K.

Table 2-4: Summary of specific heats of motor materials

Material	Specific Heat (J/kg·K)	Source(s)	Comment
Air	1009	[34]	
Copper	429	[12] , [34] , [48] , [49]	Equivalent
Thin Coating	2010	[34]	As soft rubber
Epoxy	1300	[48] , [49]	Average value
6061-T6 Aluminum	896	[46]	
M-19	545	[79] , [48] , [49]	Equivalent
1045 Steel	486	[44]	50-100°C
4340 Steel	475	[45]	

2.8 Thermal Model Heat Sources

An electric motor features three sources of thermal generation: coil joule losses, stator and rotor iron losses, and mechanical losses, such as the heat generated through viscous dissipation in bearings. Order-of-magnitude calculations were performed for the various thermal generations, the results of which are shown in Table 2-5. These results show that bearing losses are dwarfed by the iron and joule losses, and are further diminished when the volume is considered as the bearing fluid occupies significantly less space than either the iron or copper. For a low speed motor, the viscous dissipation in the rotor bearings will be negligible, and as a result the heat generation will be dominated by the joule losses in the coils, which is exponential with respect to the input current, with stator and rotor iron losses contributing noticeably to the heat generation when the motor is rotating.

Table 2-5: Order of Magnitude of Thermal Generation

Loss Type	Volumetric Magnitude	Total Magnitude
Bearing Losses	$10^{-1} \rightarrow 10^{1}$ W/m³	$<10^{-1}$ W
Iron Losses	$10^{2} \rightarrow 10^{3}$ W/m³	$10^{0} \rightarrow 10^{1}$ W
Joule Losses	$10^{5} \rightarrow 10^{6}$ W/m³	$10^{2} \rightarrow 10^{3}$ W

There are two operating modes of the motor of interest, a stationary holding mode, and a rotating mode. In the stationary case, a static magnetic flux is required to prevent rotation of the rotor, and in providing this magnetic flux, no core losses are generated as core losses are caused by a time-varying magnetic field. However, in this case, the two coils belonging to a single phase will be energized with a DC current, which will cause substantial joule losses in those coils. In the rotating case, all phases energize sequentially, twice per revolution of the magnetic field. The time-varying nature of this current waveform establishes a periodic magnetic flux waveform in the stator, which results in stator and rotor iron losses. The cyclical current waveform also results in a joule loss in each coil, the magnitude of this loss will be dependant upon the shape of the current waveform, which for the experimental setup will be trapezoidal.

Accurate prediction of how much heat is generated in the motor is critical. Because of the dependence of the heat generation on the current that is applied to the windings, the models that will be created will be used to determine the maximum current that can be applied in the different operating modes for the initial testing of the prototype motor. Testing will then be conducted to validate the model through the verification of the heat generation and temperature distribution. Accurate prediction of the heat generation as a function of the input current will be necessary for the development of an accurate model.

2.8.1 Joule Loss

Joule loss, also referred to as copper loss or I²R heating, is caused by the passing of current through a conductor with a resistance, in this case the copper wire of the coils. This loss accounts for the largest heat source of a motor when operating at low excitation frequency, and is the greatest source of inefficiency in a motor. For a single winding, the total resistance of the coil is

$$R_{e,coil} = \frac{\rho_e L_{coil}}{A_{wire}}, \tag{2-68}$$

where ρ_e is the electrical resistivity and L_{coil} is the total length of the wire having a conducting cross sectional area of A_{wire}. Over the anticipated temperature range of the motor, the resistivity of copper is linearly temperature dependant, and obeys the relationship

$$\rho_e(T) = \rho_{e,ref}[1 + \gamma(T - T_{ref})], \tag{2-69}$$

where T_{ref} refers to the reference temperature for which $\rho_{e,ref}$ is defined, usually 20°C. The temperature coefficient γ for copper is positive, corresponding to an electrical resistance that increases with a rise in temperature. Equation (2-69) can be simplified by defining what is called the temperature factor, n_T, given by

$$n_T = 1 + \gamma(T - T_{ref}). \tag{2-70}$$

Combining (2-68) and (2-69) yields

$$R_{coil}(T) = \rho_{e,ref} n_T \frac{L_{coil}}{A_{wire}}. \tag{2-71}$$

The instantaneous joule loss for one coil at a uniform temperature T can be found using the equation

$$q_{gen,coil}(t,T_{avg}) = i_{\phi}(t)^2 R_{coil}(T), \tag{2-72}$$

where I_{ϕ} is the phase current and R_{coil} is the resistance of a single coil. If the generation is normalized by the volume on which it is acting, the product of L_{coil} and A_{wire}, the volumetric generation will be

$$q'''_{gen,coil}(t,T) = \rho_e(T)\frac{i_{\phi}(t)^2}{A_{wire}^{\ 2}}, \tag{2-73}$$

where T now represents the local temperature at a point in the coil. Equation (2-73) can be simplified by replacing the current with the current density J, given by

$$J = \frac{I}{A}, \tag{2-74}$$

which represents the amount of current passing through an area. Combining (2-69), (2-73) and (2-74) yields

$$q'''_{gen,copper}(t,T) = \rho_{e,ref} n_T J(t)^2, \tag{2-75}$$

which represents the instantaneous thermal generation at a point of temperature T.

If the peak current does not change during the time of interest, for example during current-controlled operation, then the time dependence of (2-75) can be removed by considering the root mean square (RMS) current and current density, which for a periodic current waveform represents the equivalent constant current value required to impart the same thermal energy into the system. Equation (2-75) can now be expressed as

$$q'''_{gen,copper,rotating}(T) = \rho_{e,ref} n_T J_{rms}^{\ 2}, \tag{2-76}$$

where

$$J_{rms} = \frac{I_{rms}}{A_{wire}}, \tag{2-77}$$

which follows from (2-74).

In the alternate case where the voltage is constant, for a DC current it can be said that

$$IR = I_0 R_0 , \tag{2-78}$$

and since

$$R = n_T R_0 . \tag{2-79}$$

it can be said that

$$I = \frac{1}{n_T} I_0 . \tag{2-80}$$

or simply that the present current amplitude has decrease from the initial by the temperature factor n_T. This leads to the Joule loss for the constant voltage case of

$$q'''_{gen,copper,rotating}(T) = \frac{1}{n_T} \rho_{e,ref} J_{rms}{}^2 . \tag{2-81}$$

The RMS current can be calculated for any periodic current waveform *i(t)* using

$$I_{rms} = \sqrt{\frac{1}{t_2 - t_1} \int_{t_1}^{t_2} i(t)^2 \, dt} , \tag{2-82}$$

where t_1 and t_2 represent the start and end time of one period. Because of the prototype nature of the motor, the exact current waveform is unknown and likely to change frequently during development, but it is accurate to assume that the waveform will always resemble that of a typical switched reluctance motor. The waveform selected for analysis is based on Krishnan (2001), and can be seen in Figure 2-17. The phase current waveform initially rises slowly, remains at its peak value for a set time, then falls rapidly. It can be seen in Figure 2-17 that when one phase switches from on to off, the pole two-ahead begins its rise. It can also be seen that there are generally two phases active; there are never more than two phases active at the same time, as one phase disengages another begins ramping up. The overlapping of phase waveforms decreases torque ripple, and is required for smooth rotor motion in a switched reluctance motor.

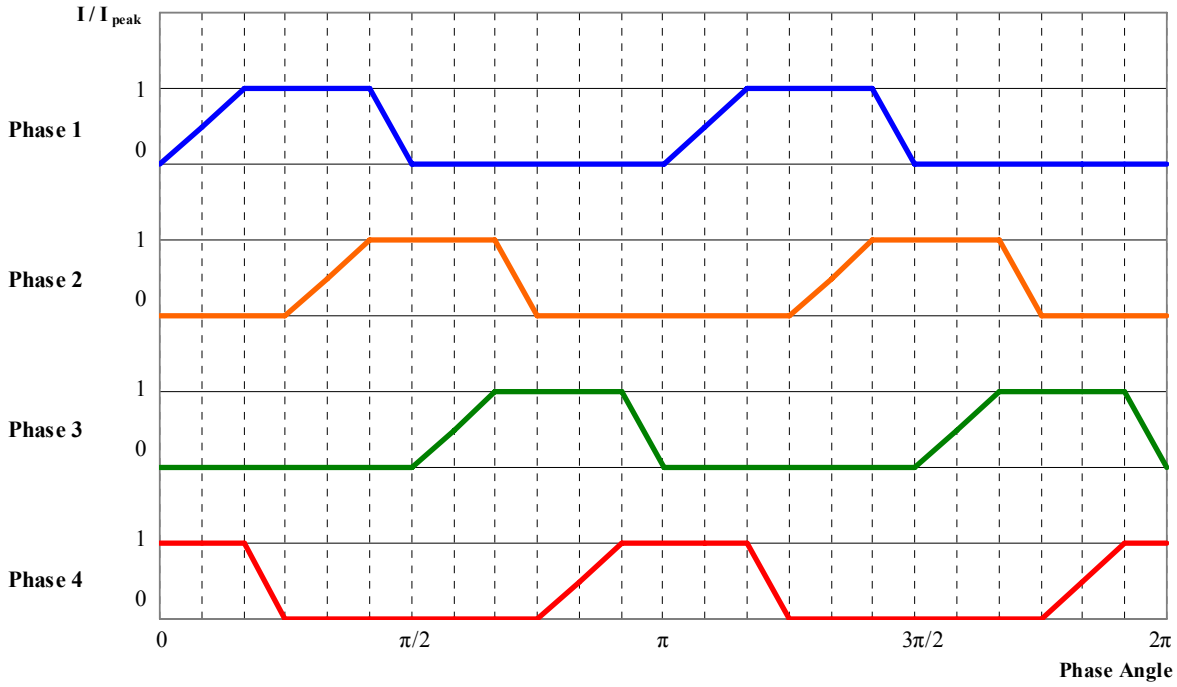

Figure 2-17: Switched reluctance motor waveform to be used in the motor model

The current waveform applied to a single phase is a piecewise function, therefore the integral in equation (2-82) will have to be separated to determine the RMS current. Solving (2-82) for the waveform presented in Figure 2-17 yields

$$I_{rms} = \frac{I_{peak}}{\sqrt{3}}. \tag{2-83}$$

For a time-varying input current, additional losses result due to the skin effect and the proximity effect. The skin effect refers to the AC phenomena where as the frequency increases, eddy currents created by the primary current cause the distribution of current in the wire to flow closer to the outer face, or skin, of the conductor. The proximity effect results when there are parallel conductors, such as in a motor winding. The alternating magnetic fields created by the alternating current interact with the fields created by adjacent conductors, and ultimately affects the distribution of current within those conductors. The two effects, skin and proximity, combine to create what is called the AC resistance, which Matveev (2006) notes can add few percent to the total resistance at low frequencies. The DC

resistance is simply a function of conductor geometry, resistivity, and temperature, however the AC resistance requires numerous geometric parameters to be considered.

To find the AC resistance, first a Fourier series decomposition was performed; this is detailed in Appendix A. The Fourier series decomposition transformed the piecewise SRM current waveform into a series of sines and cosines of increasing frequency, each an integer multiple of the fundamental frequency, 13.3 Hz, which sum to create an approximation of the original wave. The decomposition results in the modal magnitudes seen in Figure 2-18. It is necessary to perform the Fourier decomposition because the skin depth, which represents the distance at which the current density decays to 37% (e^{-1}) of the value at the surface of the conductor, diminishes with increasing frequency, causing higher frequency signals to travel on the surface of the conductor rather than in the middle, hence the name 'skin effect'.

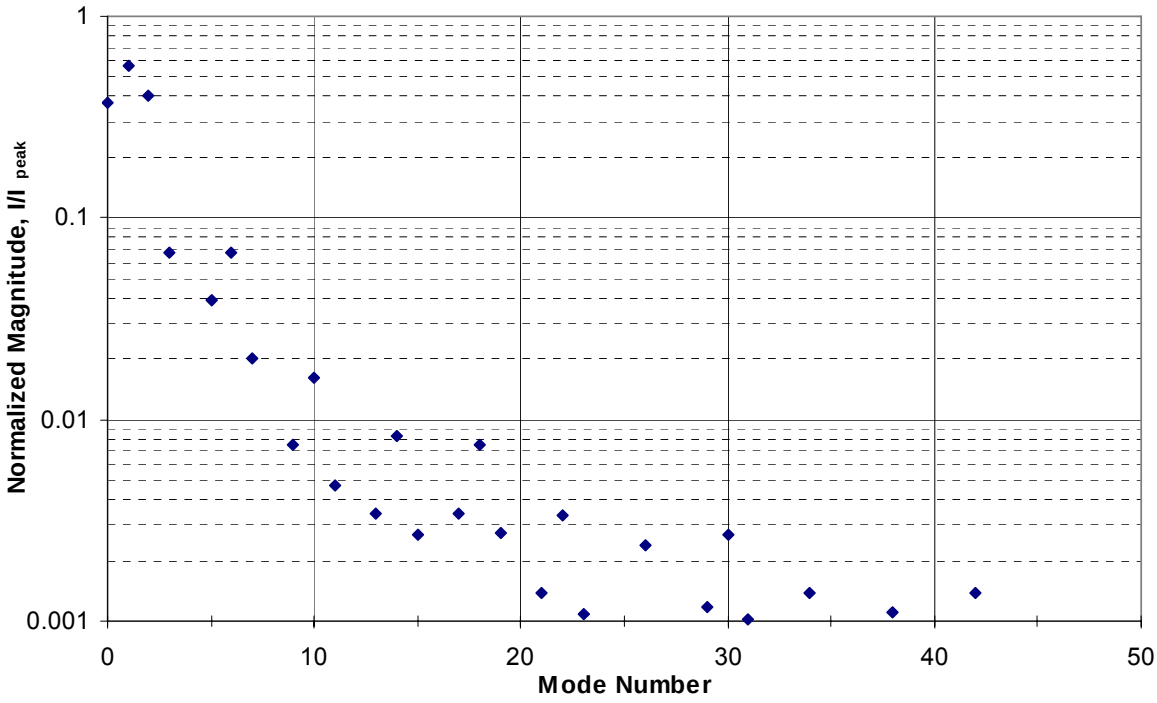

Figure 2-18: First 50 modal magnitudes of normalized SRM current waveform

The skin depth of the n^{th} mode is required, and can be found by

$$\delta_n = \sqrt{\frac{\rho_e}{\pi f_n \mu_0}}, \tag{2-84}$$

for a copper wire where f_n is the frequency of the nth mode, and μ_0 is the permeability of free space, $4\pi \times 10^{-7}$ N/A². The wire used in the prototype motor is sufficiently large that it would require that the frequency exceed 3 kHz before the skin effect becomes important. Nevertheless at the lower frequencies the motor will experience, the skin effect should still be considered. For the wire used in the prototype motor, the total loss can be found by

$$Q_{cu,S,P} = R_{DC}\left[I_0^2 + \sum_{n=1}^{m}\left(\frac{I_k}{\sqrt{2}}\right)^2\left(W_{S,n}\left(\frac{d}{\delta_n}\right) + \frac{4n_L^2 - 1}{3}W_{P,n}\left(\frac{d}{\delta_n}\right)\right)\right], \tag{2-85}$$

where I_0 is the current of the 0th harmonic, or the DC component of the waveform, n_L is the number of conductors in one layer, and $W_{S,k}$ and $W_{P,k}$ are the skin effect and proximity effect factors, given by

$$W_{S,n}\left(\frac{d}{\delta_n}\right) = \frac{d}{2\delta_n}\frac{\sinh(d/\delta_n) + \sin(d/\delta_n)}{\cosh(d/\delta_n) - \cos(d/\delta_n)}, \tag{2-86}$$

and

$$W_{P,n}\left(\frac{d}{\delta_n}\right) = \frac{d}{2\delta_n}\frac{\sinh(d/\delta_n) - \sin(d/\delta_n)}{\cosh(d/\delta_n) + \cos(d/\delta_n)}. \tag{2-87}$$

The skin effect and proximity effect factors increase the losses rapidly, for example the power loss at the 54th mode, 360 Hz is doubled and at the 93rd mode the power loss is quadrupled, however the modal magnitudes have diminished so much by these modes that the overall increase in power loss resulting from the SRM waveform is increased by only 0.78%. A factor can now be introduced such that

$$n_{S,P} = \frac{Q_{cu,S,P}}{I_{SRM,rms}^2 R_{DC}}, \tag{2-88}$$

which represents the increase in heat generation resulting from these effect, and it can be seen that $n_{S,P} = 1.0078$.

For the rotating case, all modification factors can be combined into one equation, such that

$$q'''_{gen,copper,rotating}(T) = \rho_{e,ref} n_c n_T n_{S,P} J_{rms}{}^2 . \quad \textbf{(2-89)}$$

For a the case of a holding torque, in which the current is a constant, or simply DC, the current will be the peak current applied to a single phase, and this will be the minimum current necessary to generate a full deformation of the flexispline. This current can be predicted using finite element analysis due to the high degree of non-linearity, and will be verified through experimentation. For this case, the current can be written as

$$I = I_{\min,hold} , \quad \textbf{(2-90)}$$

and similarly

$$J_{\min,hold} = \frac{I_{\min,hold}}{A_{wire}} \quad \textbf{(2-91)}$$

which can be substituted into (2-75), giving

$$q'''_{gen,copper,holding}(T) = \rho_{e,ref} n_c n_T J_{\min,hold}{}^2 . \quad \textbf{(2-92)}$$

2.8.2 Core Losses

Core losses, which consist of hysteresis loss and eddy current loss, are the other significant sources of heat generation in an electric motor. Hysteresis loss is caused when a magnetic material is subjected to a time-varying magnetic flux; the alignment, stretching, and rotation of magnetic domains of a magnetic material is an irreversible process, and some of the energy used to affect this change is converted to heat as the domains reorient. Eddy current loss occurs as a result of current loops formed around flux lines in each lamination. The magnitude of the eddy currents is dependant upon the thickness of the construction material which is the reason why stators are formed from a stack of thin laminations which helps to minimize the eddy loss.

The thermal generation in the core is the sum of the hysteresis and eddy current loss terms

$$q'''_{gen,core} = q'''_{gen,hysteresis} + q'''_{gen,eddy} , \quad \textbf{(2-93)}$$

which can be expanded using the empirically derived Steinmetz equation, which gives

$$q'''_{gen,core} = k_h f B_{\max}{}^{n} + k_e f^2 B_{\max}{}^{2}, \quad \textbf{(2-94)}$$

where k_h, k_e and n are coefficients specific to the material, f is the frequency of excitation and B_{max} is the peak magnetic flux. Though very popular, there are several limitations with this equation. The first limitation is that it is only valid for sinusoidal excitation. This drawback, however, can be addressed by decomposing a non-sinusoidal excitation into a series of sinusoidal excitations using Fourier decomposition and summing the losses, as demonstrated by Gradzki et al. (1990) and Severns (1991), or through an approach where an equivalent frequency is calculated for non-sinusoidal waveforms, as demonstrated by Reinert et al. (2001).

The approach taken to find the core loss depends on the information available for the M-19 steel which comprises the stator and fieldbooster. The vendor, Proto Laminations, Inc., provides core loss data in the form of specific core loss, SCL, in units of watts per pound. These losses are graphed for several frequencies and over a range of flux density amplitudes in Figure 2-19. Because the data was available in this form, the approach taken for this work was to perform a Fourier analysis on the flux density waveform to determine the magnitude of each mode of the induction, then the frequency and magnitude of each mode will be used to find the SCL of that mode, then a summation of the SCL of each mode will yield the total specific core loss for a waveform. The data is provided at several discrete frequencies, so before it can be used to find the core loss, a model must be developed that permits the loss at any frequency or induction to be found. The development of this model is detailed in Appendix B.

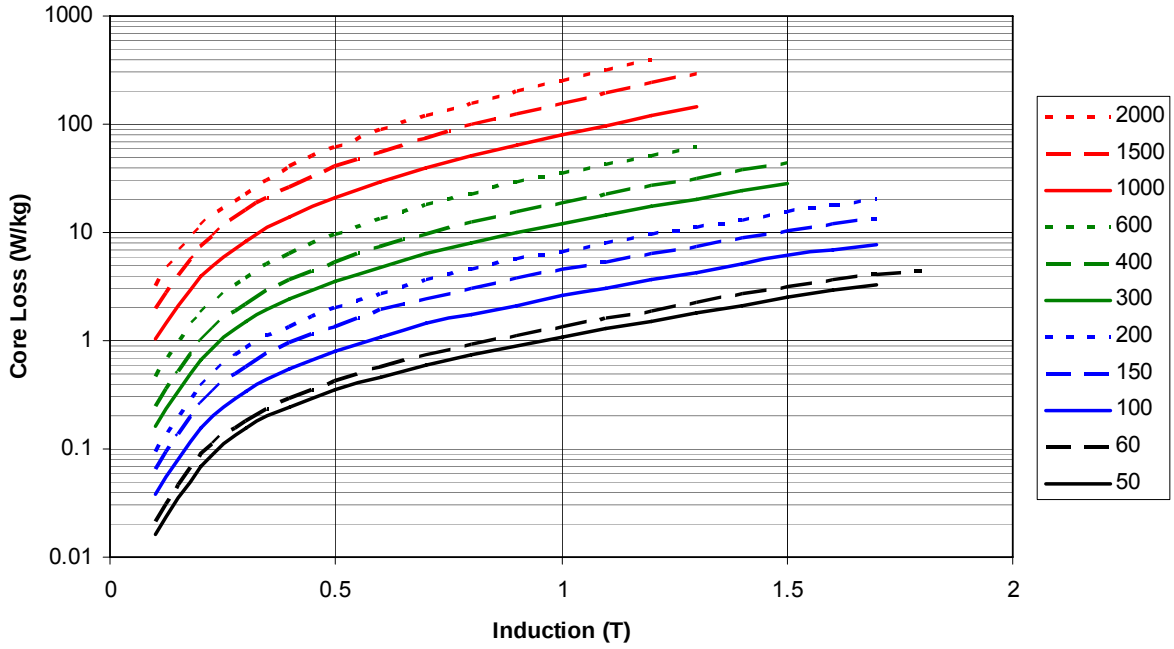

Figure 2-19: Specific Core Loss of 29 Gage, 0.014" Thick M-19 Silicon Steel under various Magnetic Flux Densities at various Frequencies, Sprague, Proto Laminations, Inc.

The model for specific core loss, as developed in Appendix B is

$$SCL = 10^{a(f)+b(f)\cdot\log(B_{\max})}, \tag{2-95}$$

$$a(f) = a_1 + a_2 \cdot \log(f) + a_3 \cdot (\log(f))^2 \tag{2-96}$$

$$b(f) = b_1 + b_2 \cdot \log(f) + b_3 \cdot (\log(f))^2 \tag{2-97}$$

where the coefficients are

$a_1 = -1.5639$ $\quad b_1 = 1.66204$

$a_2 = 0.70179$ $\quad b_2 = 0.07848$

$a_3 = 0.15148$ $\quad b_3 = 0.00060$

and *SCL* is in units of W/kg, B_{max} is in tesla, and *f* is in Hz. One benefit to the model is that it is not only accurate to within an average of 0.15% and RMS average of 5.34% for all the

values given by Proto Laminations, Inc. It also allows for core losses to be found for frequencies lower than the 50 Hz minimum from the source, which is important for the motor.

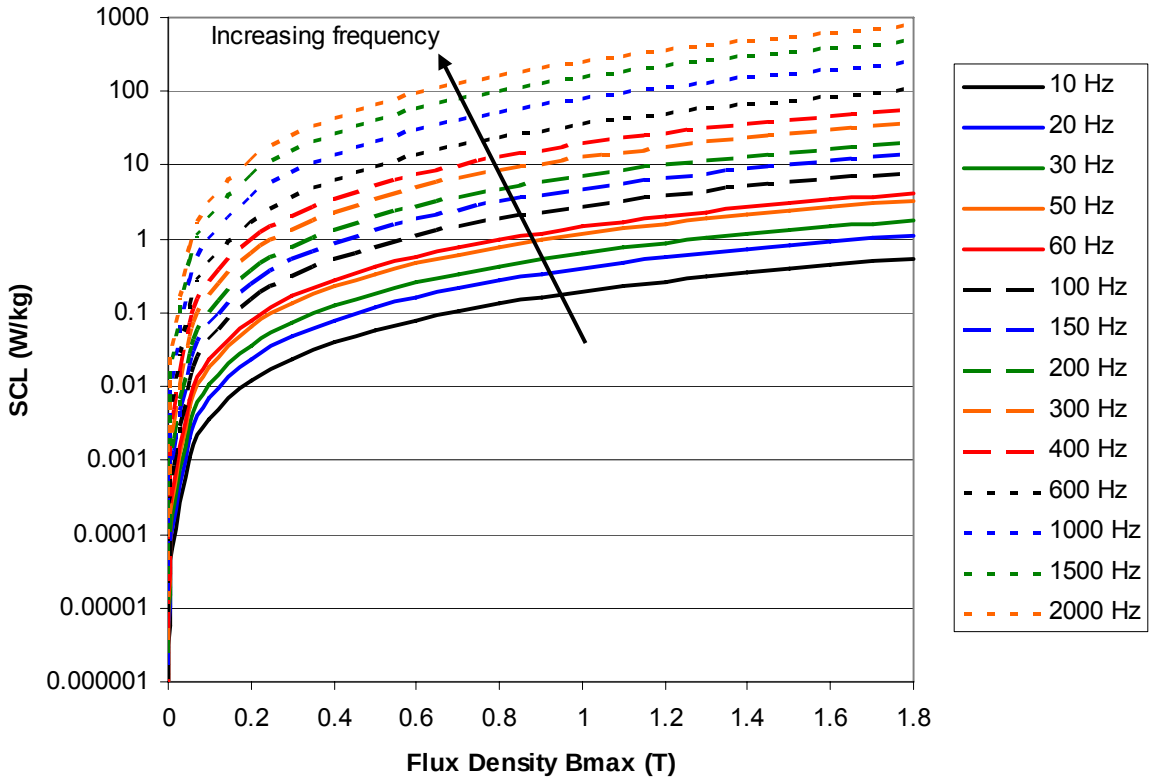

Figure 2-20: Core Loss Model

In switched reluctance motors, the stator yoke, stator poles and the rotor all experience different flux density waveforms, a fact noted by Krishnan (2001). If one of these components is considered, then the volumetric generation for one of these components can be found by the equation

$$q'''_{gen,core,\max} = \rho \sum_{k=1}^{n} SCL(f_k, B_k), \tag{2-98}$$

however first the flux density waveform is required. Appendix C analyzes the flux induction generated by an idealized switched reluctance waveform through analytic and finite element analysis, and presents the expected core loss for each component. The result is presented in

Figure 2-21, and shows that one need consider only the first 20 modes to find the approximate core loss.

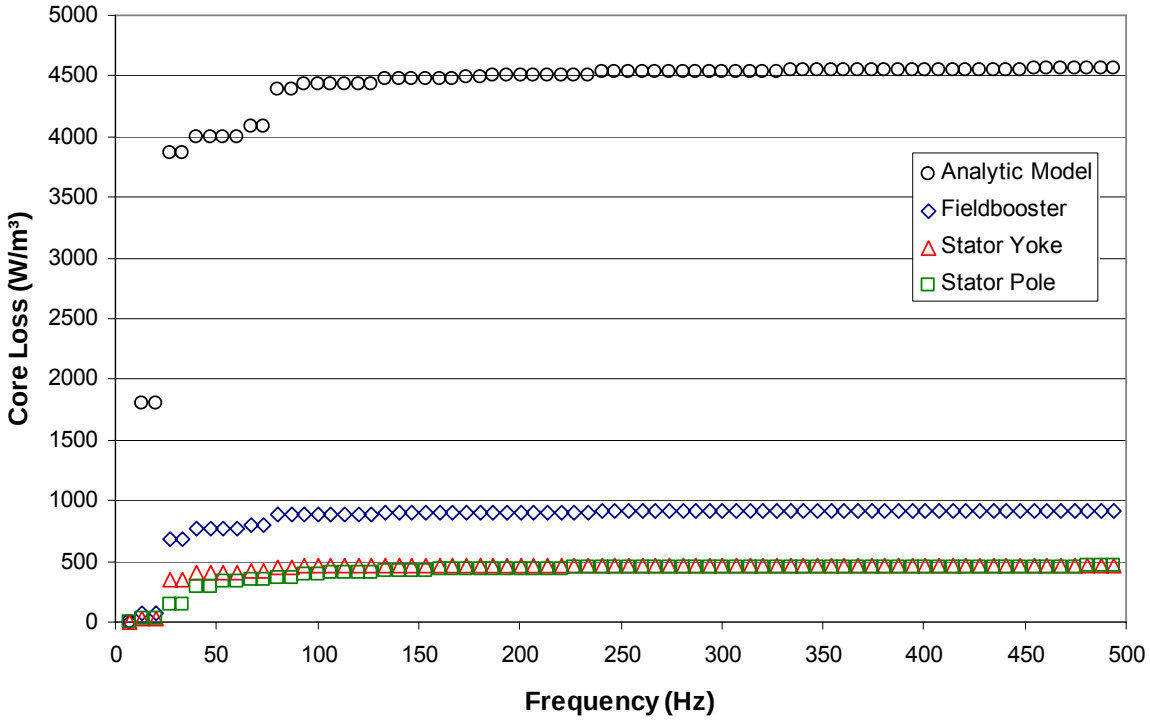

Figure 2-21: Core loss

The final source of loss that should be considered is that which is introduced through the use of pulse-width modulation (PWM). It has been observed by Mthombeni and Pillay (2005) that if the switching frequency is below 5 kHz that the losses increase, however the switching frequency of the control exceeds this, therefore no additional losses result from low speed switching.

Chapter 3

Thermal Modelling

With the material properties and mechanisms governing the heat generation and transfer well understood, models can now be constructed to predict the thermal behaviour of the motor. There are several approaches which can be taken to model the motor, each with advantages and disadvantages in terms of the time required to create a model, the accuracy of the model, computational speed, and the resolution of the solution. The types of models to be considered are finite element multiphysics models and lumped parameter circuit models.

3.1 Overview of Thermal Modelling Approaches

Both the finite element and lumped parameter models divide the motor into a number of constituent elements, however the primary difference is the scale at which this division is performed. A lumped parameter model makes several assumptions and reduces each component into a small number of geometrically primitive shapes while a finite element model might divide each component of the motor into hundreds or hundreds of thousands of elements. The difference in complexity is very large, while the motor could be divided into 26 simpler elements, finite element models consisted of approximately one million elements. With respect to the computational time, the time-dependant lumped parameter models which were developed could be solved in minutes, while a simple steady-state finite element

solution took hours to generate. Boglietti et al. (2005) note that this difference allows a lumped parameter model to be used for sensitivity analyses which is important when a designer considers that there is a large variability in several model parameters. The stark difference between these two approaches demonstrates that if an accurate lumped parameter model can be developed, it can be extremely useful both for performance prediction, but also for quickly finding the impact of a parameter change, for example coolant flow rate or the maximum current. Another use is in the design of motors. Since the motor is a prototype, a successful thermal model could be adapted into a design tool for future motors of this type.

3.1.1 Finite Element Multiphysics Model

A thermal model based on finite element analysis splits each component of the motor into hundreds or hundreds of thousands of elements each, depending on the complexity, and seeks to simultaneously solve the system of resulting equations. Because of the complex geometry of the prototype motor, it would be more accurate to fully model the air flow in and around the motor, thus giving rise to a multiphysics thermal simulation in which the heat flow through the solids is solved simultaneously with the air flowfield to determine the temperature. A multiphysics model is simply a layered approach to solving a finite element problem, where more than one system of equations is solved, and the solution of one system is required by another system. The strength of this type of modelling lies in the resolution and accuracy of the solution and ease of post-processing, however construction of the model can be time consuming. Solving the problem can require even more time; a simple steady-state solution can take hours to generate on modern computers while completing a single time-dependant simulation could take days, if not weeks to perform, and the number of variables to be changed between simulations only increases the required simulation time. While finite element analysis is a great tool for understanding the air-flow and the steady-state behaviour of the motor, it is impractical for generating time-dependant performance curves when there are several variables to be adjusted.

While solving the heat transfer and fluid flow equations simultaneously constitutes a multiphysics simulation, another layer which can be solved at the same time is the

electromagnetic simulation. When the magnetic field is incorporated into the simulation an exact treatment of the core loss can be considered, that is it can be allowed to vary spatially as a function of the local magnetic field strength. Obtaining an accurate model of the core loss does not require the use of multiphysics simulations, instead electromagnetic simulations can be performed from which the spatial loss data can be extracted.

3.1.2 Lumped Parameter Thermal Model

The simplest type of model is a lumped circuit model. In this type of model, the domain of interest is broken into smaller domains of primitive geometry which interact through thermal resistances while thermal capacitance governs the rate of temperature change for transient problems. This type of model can require less time to construct, depending on the complexity of the system to be modeled, requires less computation time, but suffers in the accuracy and resolution of the solution. The temperatures which will be found will represent an average temperature of a region, but the resolution can cause a loss of detail such as the hot-spot temperatures, which are of significant importance in the windings. With a lumped parameter model, it is difficult to simultaneously incorporate an electromagnetic model. Due to the highly non-linear behaviour of electromagnetism, the model could not be used to accurately predict the magnetic behaviour, and as such the iron thermal generation would have to be approximated. One significant advantage of this type of model is that if proven accurate, it can be used in a motor controller to determine thermal performance and be used to ensure safe operation of the motor.

3.1.3 Comparison and Summary

The objective of this work is to develop an accurate, adaptable thermal model, and for these criteria the optimal model is a lumped parameter model. Once developed, a lumped parameter model can be modified to work for the development of other motors, and due to its simplicity it can be integrated into a control scheme for said motors.

3.2 Lumped Parameter Thermal Model

A lumped circuit model based on the works of Mellor et al. (1991) and Bousbaine (1999) was developed. In order to construct the model, first the governing equations need to be established, then the geometry has to be adapted to fit the model. Next, the interactions between components needs to be investigated and fit into the framework of the model. Finally, initial conditions and boundary conditions can be specified and time-dependant solutions found.

3.2.1 Governing Equation of Lumped Parameter Model

In a lumped parameter thermal model the components of the motor assembly are simplified geometrically into basic shapes with well defined heat transfer equations. Once simplified, the relationships between components are defined, and a network of thermal resistances, capacities, and sources is created. The resulting network of heat flow can be expressed in the form

$$[C]\frac{d[T]}{dt} = [K][T] + [q_{gen}], \qquad \textbf{(3-1)}$$

where [C] is a column matrix of the nodal thermal capacitance, [K] is a matrix of inter-nodal conductances, while [q_{gen}] is a column matrix of the thermal generation at each node. Such a linear system can be solved by mathematics software such as MATLAB or Maple.

3.2.2 Solid Geometry Definition

The first step in the development of such a model is to simplify the geometry into primitive shapes which combine to approximate the true shape of the components. The shape of a motor lends itself to most components being modeled by one or more hollow cylinders, however some components or parts of components are better represented by rectangular elements. Some components were decomposed into two or three primitives to more accurately represent their true shape, as can be seen in Figure 3-1.

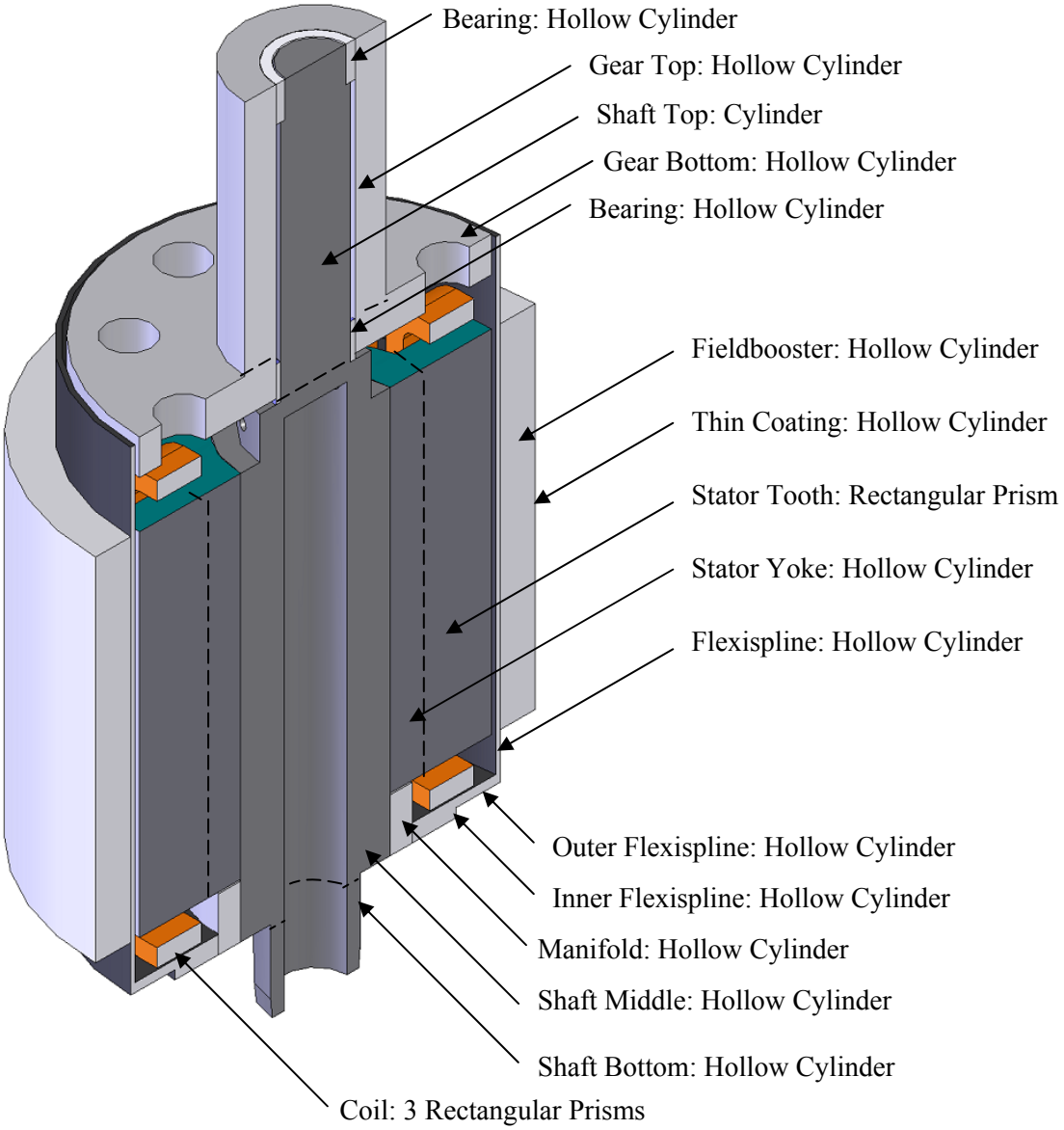

Figure 3-1: Identification of primitive components of motor

The construction of the thermal model is based upon the connections between nodes, so first the basic elements of the model must be developed. The lumped nature of the elements necessitates that some simplifications be made. Firstly, each surface is assumed to be at a uniform temperature which is represented by a two part subscript, for example $T_{x,1}$, wherein the first subscript designates the surface normal and the numerical subscript designates the inner or outer face. The center of the element is assumed to be at the average temperature $\overline{T}$,

which is found by mathematical weighting of the surface temperatures. This average temperature is the temperature at which material properties will be found for elements with temperature dependant properties, notably the resistivity of the copper coils. The two elements are shown in Figure 3-2.

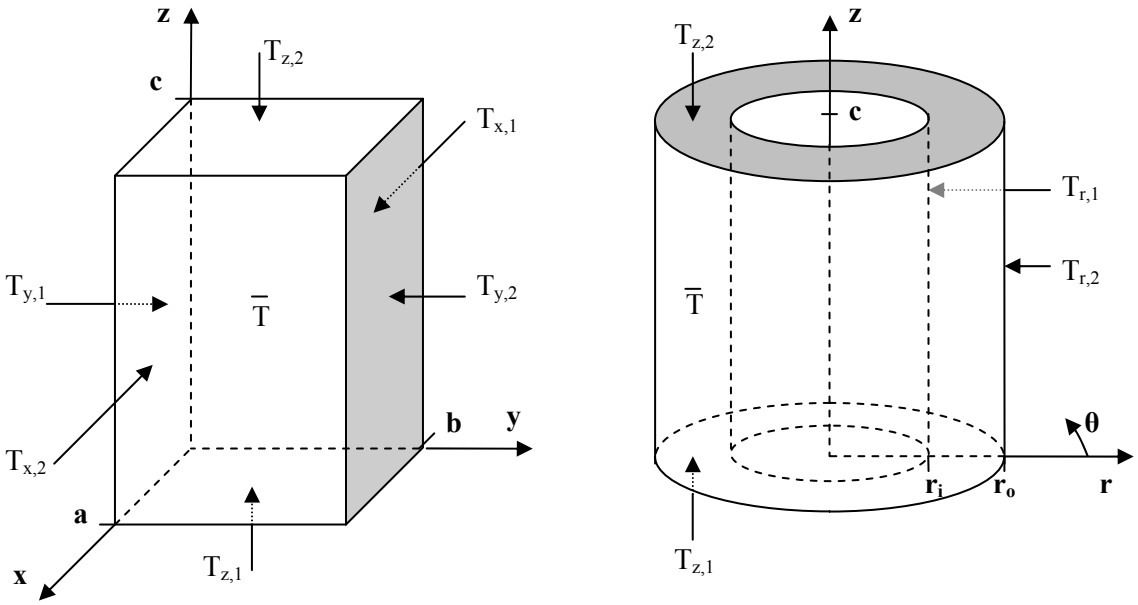

a) rectangular prismatic element

b) hollow cylindrical element

Figure 3-2: Lumped parameter geometry and nomenclature

For the rectangular element, heat is permitted to flow in all the coordinate directions and said heat flows are assumed to be independent. For this model, the cylindrical element will only have heat flows only in the radial and axial directions, limiting the model to the case where the motor is rotating. With each element there is an associated network of thermal resistances, capacitance, and sources of moderate complexity. The rectangular element can be represented by the thermal network seen in Figure 3-3. In a given direction there are two equal resistances between the two faces, at the union of which there is a third resistance which connects to the central node. The central node represents the mean temperature of the element, and it is here where the thermal storage, denoted by *C*, and the internal heat generation, denoted by Q, occur. As stated by Mellor et al. (1991), the superposition of heat generation and storage at the central node gives a mean temperature which is lower than it

actually is, and as a result the auxiliary thermal resistances $R_{x,m}$, $R_{y,m}$, and $R_{z,m}$ are negative, which compensate for this behaviour. The thermal resistances are given by the equations

$$R_{x,1} = R_{x,2} = \frac{a}{2k_x bc}, \tag{3-2}$$

$$R_{y,1} = R_{y,2} = \frac{b}{2k_y ac}, \tag{3-3}$$

$$R_{z,1} = R_{z,2} = \frac{c}{2k_z ab}, \tag{3-4}$$

and for the auxiliary resistances by

$$R_{x,m} = \frac{-R_{x,1}}{3}, \tag{3-5}$$

$$R_{y,m} = \frac{-R_{y,1}}{3}, \tag{3-6}$$

$$R_{z,m} = \frac{-R_{z,1}}{3}. \tag{3-7}$$

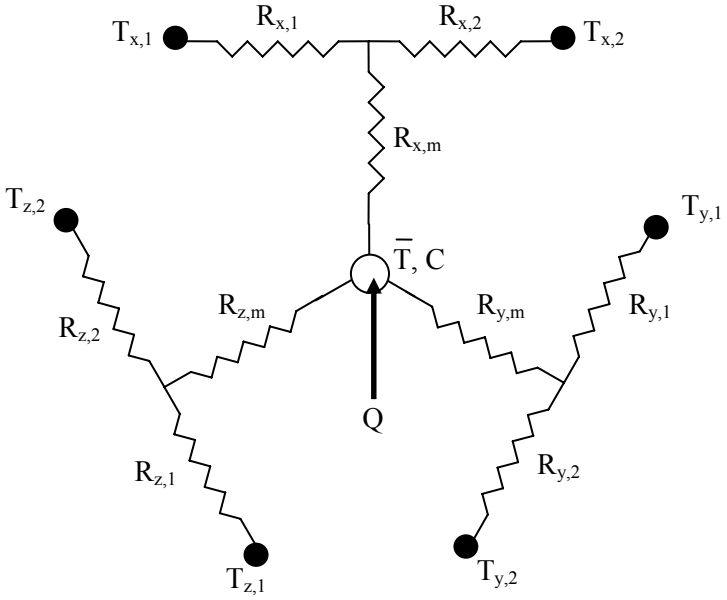

Figure 3-3: Thermal network model of rectangular prismatic component

The cylindrical element is somewhat simpler due to there being only two directions of interest, the radial and axial. The cylindrical element is represented by the thermal network pictured in Figure 3-4. The resistances comprising the network are given by the equations

$$R_{r,1} = \frac{1}{4\pi k_r c}\left[\frac{2r_o^2 \ln(r_o / r_i)}{(r_o^2 - r_i^2)} - 1\right], \tag{3-8}$$

$$R_{r,2} = \frac{1}{4\pi k_r c}\left[1 - \frac{2r_i^2 \ln(r_o / r_i)}{(r_o^2 - r_i^2)}\right], \tag{3-9}$$

$$R_{z,1} = R_{z,2} = \frac{c}{2k_z(r_o^2 - r_i^2)},$$

and for the auxiliary resistances by

$$R_{r,m} = \frac{-1}{8\pi k_r c(r_o^2 - r_i^2)}\left[r_o^2 + r_i^2 - \frac{4r_o^2 r_i^2 \ln(r_o / r_i)}{(r_o^2 - r_i^2)}\right], \tag{3-10}$$

$$R_{z,m} = \frac{-R_{z,1}}{3}. \tag{3-11}$$

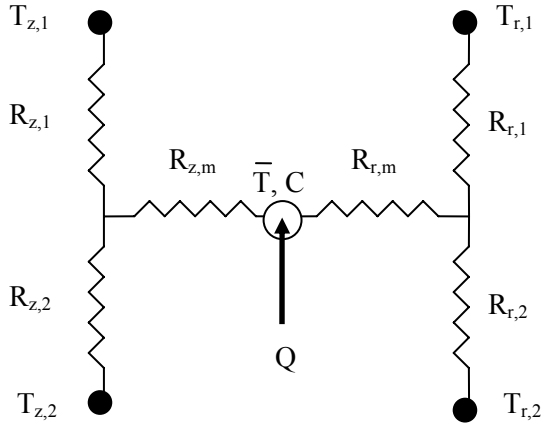

Figure 3-4: Thermal network model of hollow cylindrical component

The model was programmed such that the Mellor et al. (1991) type model is intact, however the option for another type of model was added. By simply setting the auxiliary resistances to zero, the model is effectively a standard type lumped parameter model.

For either the prismatic or cylindrical element, the thermal capacity is given by

$$C = \rho V c\,, \tag{3-12}$$

and the internal generation is given by

$$Q = V q'''_{gen}\,. \tag{3-13}$$

The geometry was set such that volume and surface areas were preserved when simplifying the components to ensure proper thermal storage, heat generation, and internodal thermal conductances.

3.2.3 Solid Domain Model Construction

Construction of the overall model is not a trivial exercise, the greatest challenge and most time-intensive part is generating the [*K*] matrix. Each element must be analyzed in turn and the connection to every other element determined. A sample connection between the shaft and the stator yoke is shown in Figure 3-5.

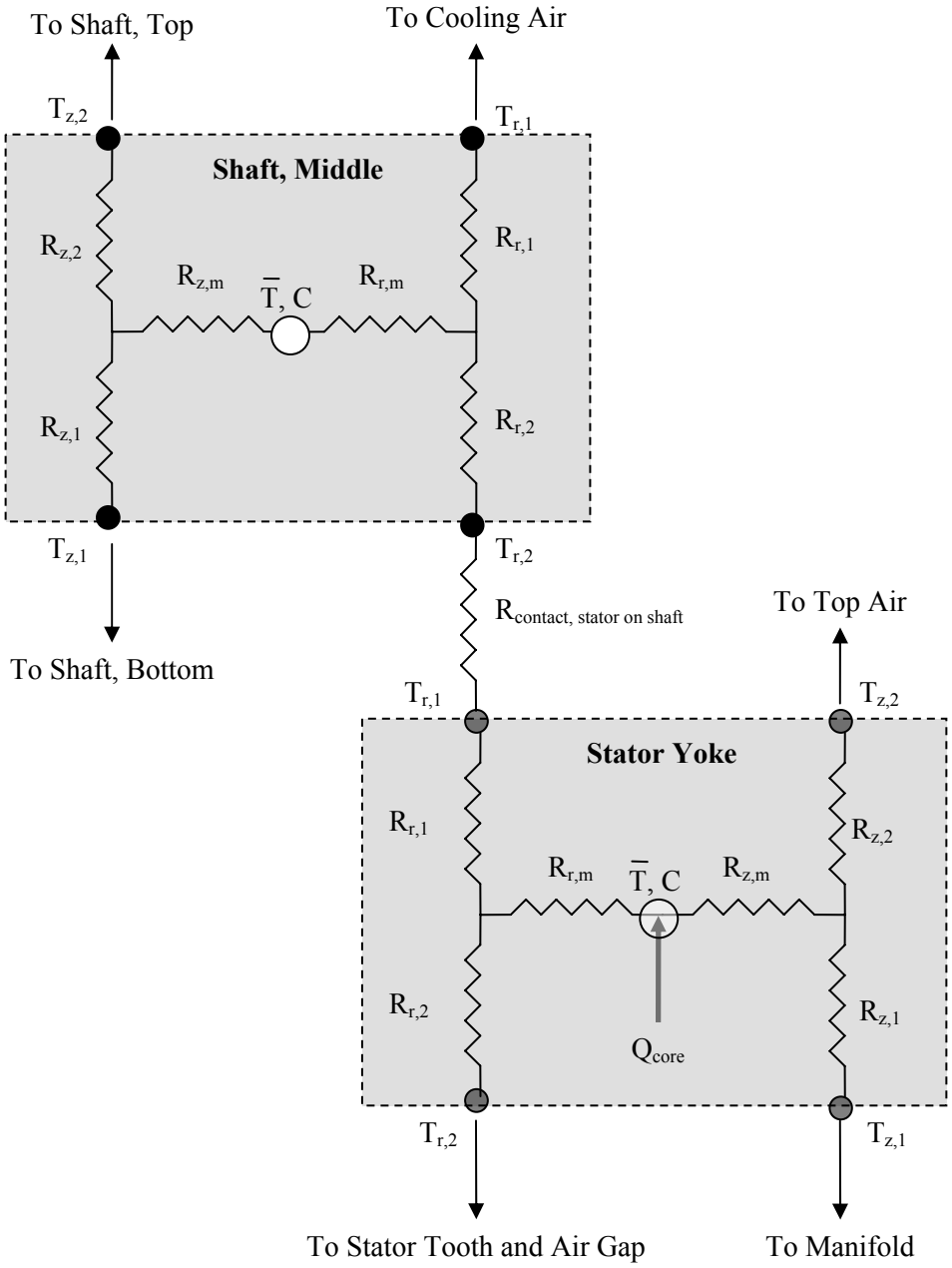

Figure 3-5: Sample elemental interaction from construction of lumped parameter model

The procedure begins by identifying two components, and then determining if a direct connection exists between the two components. If a path can be identified, the resistances are summed, then inverted to give the inter-nodal conductance. The most important rule is

that a direct path and therefore conductance between two elements only exists if heat can pass from one object to the other without first passing through another body. Complications exist here, for example the air surrounding components acts as a body into which heat flows from the warm neighboring components via convection, however heat can pass between from surface to surface through the air by radiation, for example from the stator tooth to the flexispline through the thin air gap. Once the [*K*] matrix has been found, equation (3-1) can be solved.

3.2.4 Fluid Domain

The motor is surrounded and filled with air, however even if there is no forced airflow, there will still be motion caused by the buoyancy of warm air relative to cooler air. This motion helps to transport heat out of the motor into the ambient air of the surroundings.

For the internal air, the airflow can be modeled as flow in a duct with multiple walls. Based on Incropera and DeWitt (2002), the mean temperature T_m along an N-sided duct with walls of constant temperature is given by the differential equation

$$\frac{dT_m}{dx} = \frac{1}{\dot{m}c_p}\sum_{n=1}^{N} P_{w,n}U_n\left(T_{s,n} - T_m\right), \tag{3-14}$$

where $P_{w,n}$ is the wetted perimeter and $T_{s,n}$ is the surface temperature of the of the n^{th} face, and U_n is the total heat transfer coefficient from that face to the flow which has a mass flow rate of $\dot{m}$ and a specific heat of c_p. The assumption of a constant surface temperature is important because it limits the maximum output temperature to one which approaches the surface temperature for the case of a fluid heated by the surface. The constant temperature assumption used here matches the constant temperature assumption that governs the solid domains, hence the physics is consistent.

For a duct which is enclosed by a single face at temperature T_s, Incropera and DeWitt (2002) give the solution

$$T_{m,o} = T_s - \left(T_s - T_{m,i}\right)\exp\left(-\frac{K}{\dot{m}c_p}\right), \tag{3-15}$$

where $T_{m,i}$ is the mean inlet temperature and $T_{m,o}$ is the mean outlet temperature and K is the conductance from the center of the solid into the flow. For the more general case of an N-sided duct, the solution to (3-14) is

$$T_{m,o} = \left(\frac{\sum_{n=1}^{N} K_n T_{s,n}}{\sum_{n=1}^{N} K_n} \right) - \left(\frac{\sum_{n=1}^{N} K_n T_{s,n}}{\sum_{n=1}^{N} K_n} - T_{m,i} \right) \exp\left(- \frac{\sum_{n=1}^{N} K_n}{\dot{m} c_p} \right). \quad \textbf{(3-16)}$$

If the airflow inside the motor is considered to be through a multisided duct, the interior air could be subdivided into several segments, as seen in Figure 3-6

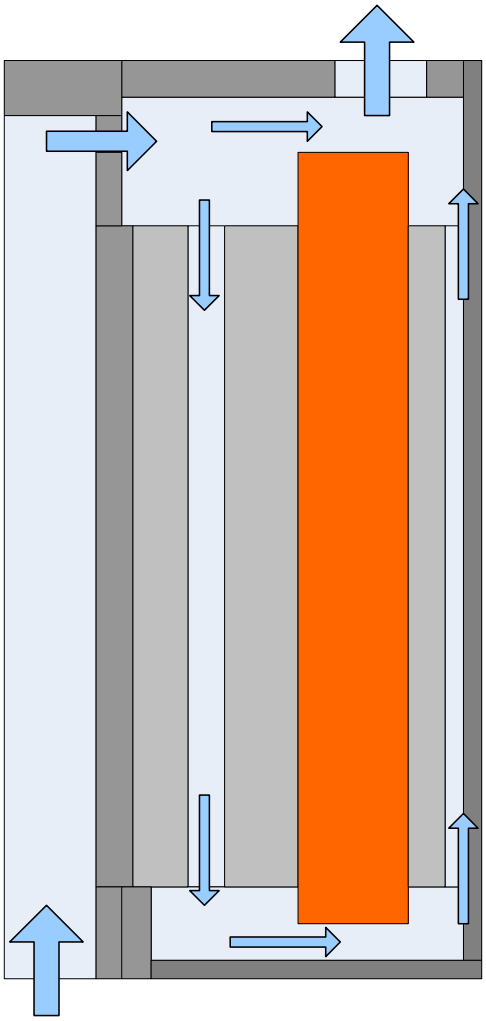

Figure 3-6: Assumed airflow inside motor

For this model, characteristic geometry must be supplied to provide hydraulic diameters and other critical dimensions. The air enters the top and divides; a portion leaves the motor while a portion stays within and flows to the bottom of the motor where it cools the exposed windings. The ratio of the air which leaves immediately versus that which flows to the bottom will be assumed to be based on the ratio of the square of their respective diameters,

$$\frac{Q_{top}}{Q_{bottom}} = \frac{A_{exit}}{A_{entrance,path}} = \frac{d_{exit}^2}{D_{h,path}^2}, \tag{3-17}$$

however a CFD-based approach could be incorporated in the future to improve the accuracy.

3.2.5 Model Solution

Because of the non-linearities which exist in a model, an appropriate way to solve the system of equations is through discretization, where a time step is specified and the temperature change at one node based on the influence of the surrounding nodes is computed. In order to compute the nodal temperature change per time step, equation (3-1) can be re-written in the fully explicit form

$$\Delta T_m = \frac{\Delta t}{C_m}\left[q_m + \sum_{n=1}^{N} K_{m,n}\left(T_n - T_m\right)\right], \tag{3-18}$$

where ΔT_m, C_m and Q_m are the temperature change, thermal capacitance and thermal generation at the mth node, Δt is the time step, $K_{m,n}$ is the conductance between nodes m and n, and T_m and T_n are the temperatures at the mth and nth nodes respectively. Once the changes in temperature at all the nodes are computed it is added to the temperatures from the previous iteration which results in the temperatures at that time step. Between time steps the air temperatures will change based on their new inlet and outlet temperatures, for simplicity and stability given by the average of the inlet and outlet temperatures deterined by (3-16),

$$\Delta T_{air} = \left(\frac{T_{air,in} + T_{air,out}}{2} \right) - T_{air,old}. \tag{3-19}$$

If the conductance between nodes and the thermal generation remained constant, then simply stepping through each time step until the desired end condition was met would

generate the temperature profile. The conductance however includes convection, and as the film temperature increases, so too does the convective conductance term. Because the temperature at each time is now known, the convective heat transfer coefficients can be re-calculated which will give higher accuracy to the transient results. In addition to the convection heat transfer coefficient, the temperature coefficient for the heat generation by joule loss can also be calculated and the temperature specific value applied for each iteration. Heat transfer by radiation is relatively simple to incorporate into this model. As the temperature increases by a small amount between time steps, so too does the radiative heat transfer coefficient. Other material properties such as kinematic viscosity will update between iterations, as will the film temperature used in the calculation of the Rayleigh numbers.

Chapter 4

Experimental Setup

In order to assess the accuracy of the motor thermal model, detailed experiments were run in which the motor was run and the temperatures at various locations on the motor were recorded with respect to time then compared to the pridictions of the thermal model. In order to perform these experiments, several pieces of equipment were utilized to record the inputs and responses generated. Thermal response was measured using thermocouples and heat flux sensors, the cooling air flow using a flow meter and a thermocouple, and the electrical input through the motor control system, while a data acquisition system recorded the measurements. In order to make use of the measurements, their accuracy was assessed based on rated accuracy and additional error was quantified based on physical models.

4.1 Sensors and Transducers

For thermal experiments, numerous inputs and outputs were measured: the input voltage and current, as well as the cooling air flow rate, and the resulting temperatures and heat fluxes. The current and voltage were recorded using the proprietary control system, and was used to determine the power input to the system. Assessing the overall thermal response requires sensors beyond those built-into the motor and its control system. The temperatures were measured by thermocouples mounted in strategic locations on the motor, heat flux was

measured using heat flux sensors mounted on various surfaces within the motor, and a flow meter was used to quantify the amount of cooling air input to the motor.

4.1.1 Thermocouples

A common method for recording temperature is through the use of a thermocouple. A thermocouple works by the Seebeck effect where a small voltage is generated in two wires of dissimilar metals when the junctions are at different temperatures, as seen in Figure 4-1. Different metals have different Seebeck coefficients which result in different voltage readings when measuring the same temperature difference, thus it is important to know the thermocouple type to make accurate temperature readings. By knowing the temperature at one end, the measured voltage can then be used to determine the temperature at the other end, thus allowing for the measurement of a specific point in space.

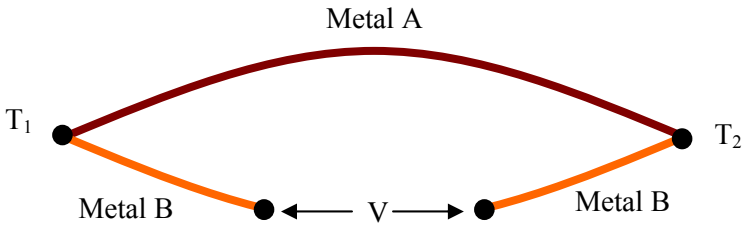

Figure 4-1: Principle of Thermocouple Operation

There exist numerous types of thermocouples, which differ in their constituent metals, and as a result offer a variety of operational temperature ranges, accuracies, voltage gains and permissible working environments. Because temperature measurements were made in a magnetic environment, it was important to ensure that the thermocouples were comprised of non-magnetic metals; for example the popular K-type thermocouple contains alumel, a nickel alloy which is magnetic, however a T-type thermocouple is composed of copper and constantan, neither of which are magnetic. The chosen thermocouple for this work was from a T-type thermocouple from Omega Engineering, Inc., model 5TC-GG-T-24-72. Based on Omega (2009b), these exposed junction type thermocouples which feature a glass braid insulation allow a temperature range of -73°C to 200°C, 24 AWG wires and 2 m lead wires.

The most important consideration is that they are built from special limit of error wire, which corresponds to a limit of error of the larger of 0.5°C or 0.4%.

Figure 4-2: Omega 5TC-GG-T-24-72 T-type Thermocouple

4.1.2 Heat Flux Sensor

Another method of acquiring thermal data is through the use of a heat flux sensor. A heat flux sensor is essentially a thermopile, which is comprised of several thermocouples connected in series whose junctions are separated by dielectric material of a known thickness, which can be used to determine the heat flux passing between them based on the voltage generated.

There are several important factors in the selection of a heat flux sensor. Heat flux sensors come in a variety of shapes, sizes, operational temperature ranges, thermal resistances, capacitances, and voltage gains. Perhaps the most important consideration in selecting a heat flux sensor is that the entire surface must have flux passing over it. For this reason, many heat flux sensors are flexible to enable them to cover a curved surface. The motor is expected to dissipate on the order of 1000W, and has a surface area on the order of 0.1 m^2, therefore the average heat flux is expected to be on the order of 10,000 W/m^2. The heat flux will unlikely be uniform, so a heat flux sensor should be able to measure a maximum value several times greater than the average, yet be sensitive enough to measure small heat fluxes accurately, therefore a higher gain is desirable. A low thermal resistance is best as the very presence of a heat flux sensor disrupts the natural thermal field, the lower this resistance the

more accurate the reading will be. Thermal capacitance determines how quickly the sensor reacts to a change in heat flux, therefore this property should be low to properly resolve transient heat flux variations.

A search was performed to identify potential sources of heat-flux sensors, the result being that there are few companies that manufacture heat flux sensors, and their purposes vary significantly. Hukseflux, Vatell Corporation, RdF Corporation, and Omega are four manufacturers of heat flux sensors, each of which targets different applications and offers a variety of products. One heat flux sensor that meets the outlined needs is the HFS-4 sensor from Omega. This 35 mm x 25 mm sensor is flexible, offers a working temperature range between -200°C and 150°C, has a nominal gain of 1.8 $\mu V/(W/m^2)$, and offers a low nominal thermal resistance of 1.8×10^{-3} m^2K/W.

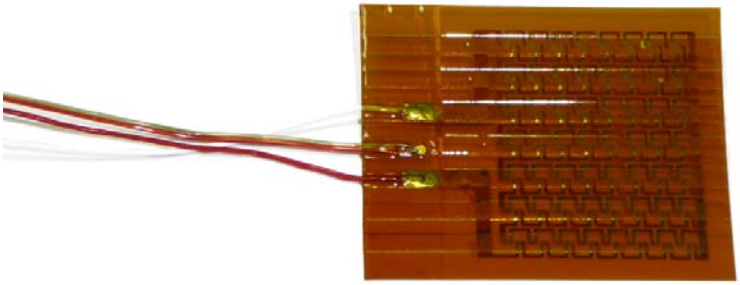

Figure 4-3: Omega HFS-4 Heat Flux Sensor

Six HFS-4 sensors were purchased, the individual sensitivities ranged from 1.56 to 1.94 $\mu V/(W/m^2)$ at 21°C. In addition to being able to measure heat flux, the HFS-4 has an integrated K-type thermocouple to measure the average temperature of the heat flux sensor, however these thermocouples were cut out of the sensors to remove the magnetic material since their presence could lead to undesirable effects inside a motor. The calibration reports accompanying the heat flux sensor included a multiplication factor to compensate for the temperature dependence of the thermal conductivity of the thermal barrier as well as the Seebeck coefficient of the thermopiles. A highly accurate measurement of the heat flux can therefore be obtained by multiplying the measured heat flux by the compensation factor, seen in Figure 4-4, at the average heat flux sensor temperature read off the thermocouple.

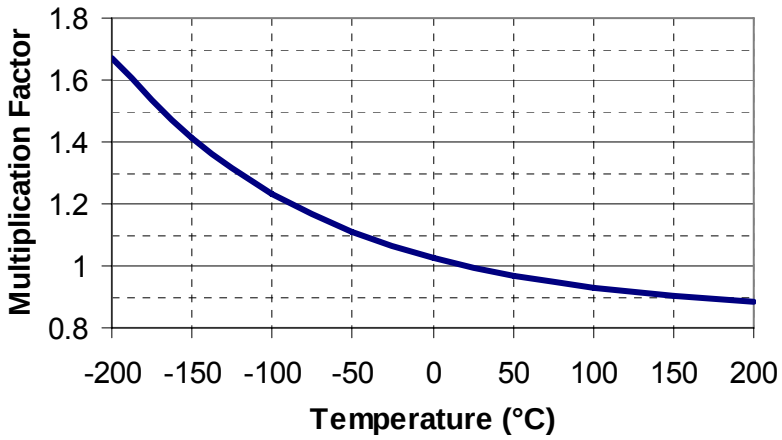

Figure 4-4: Output Multiplication Factor of Heat Flux Sensor HFS-4 by Omega, (2008)

The compensation factor given by the calibration report from Omega (2008), was given in the form of a graph. Data was read from this graph and a curve was fit to the data using CurveExpert 1.3. The exponential curve fit

$$f = 0.8413 + 0.2127 \cdot e^{-0.004146 \cdot T}, \tag{4-1}$$

where T is the temperature in degrees Celsius was found to match the data extremely well, and an implementation of this factor can be seen in Appendix E.

4.1.3 Flow Meter

In order to quantify the cooling airflow input to the motor, a flow meter was used to record the flow rate of air which was logged using LabVIEW. The flow meter used is from Omega Engineering, Inc., model FLR6725D, which is capable of recording 2 to 25 SCFM (standard cubic feet per minute), or approximately 1 to 12 L/s, as stated in the User's Guide, Omega (2005). For the central shaft into which the airflow first enters the motor, which has a diameter of 30.5 mm, this corresponds to Reynold numbers between 2480 and 31,000 at 300 K, therefore the flow meter should be sufficient to measure both transitory flow and fully developed turbulent pipe flow.

Figure 4-5: Omega FLR6725D Flow Meter, from Omega (2005)

The FLR6725D offers both a digital read-out of the flow rate, as well as a voltage output for data logging. An advantage of the dual-outputs is that the flow rate recorded using a data-logger can be corrected based on the readout, compensating for any signal degredation. As stated in Omega (2005), the voltage output can be set at either 0-5 V_{DC} or 0-10 V_{DC}, and the maximum and minimum voltages correspond to the maximum and minimum flow the unit can record, or they can be manually set to chosen limits. To maintain a stronger signal the 0-10 V_{DC} range was used.

4.2 Data Acquisition and Logging

To read the analog signals generated by the sensors and transducers, data acquisition (DAQ) hardware was required. Once these signals were interpreted by the DAQ, a digital signal was sent to a computer for processing or recording. There are numerous solutions to acquiring and processing analog data. Companies such as National Instruments (NI) offer DAQ hardware and a software interface which allows the user to generate virtual instruments to analyze data in real-time in order to monitor or control a system. Other companies offer hardware which generates digital signals which can be read from the serial or USB port of a computer using custom software or ready-made software such as MATLAB's Data Acquisition Toolbox. During the development and testing of the motor, LabVIEW was

chosen as the environment in which the control system was to be developed, and with LabVIEW came NI DAQ hardware. In order to ensure seamless integration when necessary, it was decided that thermal data acquisition would also be made using NI hardware and LabVIEW.

4.2.1 Thermocouple Data Acquisition

For thermocouple measurement, National Instruments' NI USB-9211A portable USB-based DAQ for thermocouples was chosen, and can be seen in Figure 4-6. As stated in National Instruments (2006), the module is compatible with J, K, R, S, T, N, E, and B type thermocouples, offers 24-bit resolution, and features a voltage range of -80 mV to 80 mV, allowing for temperatures well over 1000°C to be read from any thermocouple type. Each unit allows for the connection of four thermocouples with an asynchronous sampling rate of 12 samples per seconds (S/s), for a maximum frequency of 3 Hz per channel. The module features built-in cold-junction temperature compensation, meaning that the base temperature is measured internally, improving accuracy.

Figure 4-6: NI USB-9211A Thermocouple DAQ, National Instruments (2009A)

4.2.2 Multifunction Data Acquisition

For thermopile and air flow measurements, National Instruments' NI USB-6221 multifunction DAQ was chosen, and can be seen in Figure 4-7. As stated in National Instruments (2006a), this 16-bit unit has 16 analog and 24 digital inputs at an asynchronous

sampling rate of 250 kS/s, with input voltage ranges of ±200 mV, ±1 V, ±5 V, and ±10 V. On the minimum setting, The minimum voltage range is -200 mV to 200 mV with an accuracy of 112 µV which for a thermopile with a nominal gain of 1.8 µV/(W/m^2) corresponds to a maximum recordable heat flux of 111 kW/m^2 at an accuracy of 62.2 W/m^2, however, the maximum recommended heat flux for the sensors is 95 kW/m².

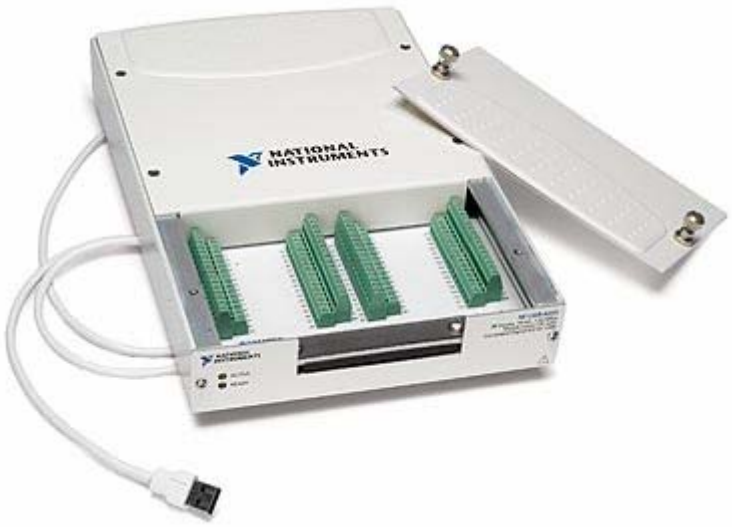

Figure 4-7: NI USB-6221 Multifunction DAQ, National Instruments (2009B)

Table 4-1: Heat Flux Range, Accuracy and Sensitivity based on a nominal thermopile gain of 1.8 µV/(W/m^2) National Instruments (2006A)

Voltage Range	Heat Flux Range	Voltage Accuracy	Heat Flux Accuracy	Voltage Sensitivity	Heat Flux Sensitivity
±200 mV	± 4000 W/m^2	112 µV	62.2 W/m^2	5.2 µV	2.89 W/m^2
±1 V	± 20,000 W/m^2	360 µV	200 W/m^2	12.0 µV	6.67 W/m^2
±5 V	± 100,000 W/m^2	1.62 mV	900W/m^2	48.8 µV	27.1 W/m^2
±10 V	± 200,000 W/m^2	3.1 mV	1722 W/m^2	97.6 µV	54.2 W/m^2

4.2.3 LabVIEW Virtual Instruments

To compliment the NI DAQ hardware, LabVIEW was used for programming and data logging. Due to its nature, LabVIEW requires that virtual instruments be constructed by the

user to meet the specific needs of an experiment. A Virtual Instrument was built in LabVIEW for the purpose of monitoring the thermal response to the motor operation. Figure 4-8 shows the graphical user interface of the instrument, but behind the scene is an instrument built using LabVIEW's proprietary graphical programming language; this structured program can be seen in Appendix E.

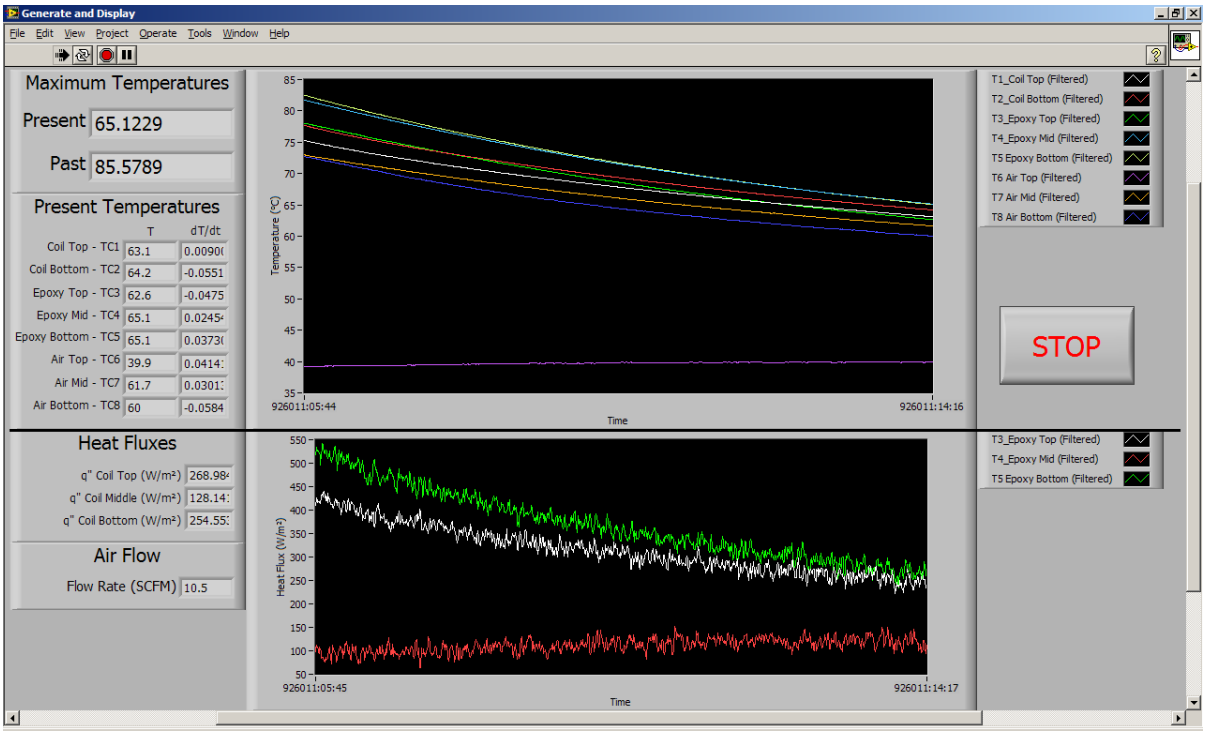

Figure 4-8: Motor thermal Virtual Instrument panel during operation

The thermal VI is responsible for processing the data from the sensors, and as such graphs and numerical readouts are present for the temperatures and heat fluxes it records, and a numerical display of their derivatives are also presented to observe the change in these properties with respect to time. For processing of the data, it is important to log the raw data from the sensors; data manipulation can be performed after the data was collected and it is more accurate to work with raw data than data that has been filtered, for example.

4.3 Sensor Installation

To measure the motor performance, numerous thermocouples and heat flux sensors were employed. Based on the available data acquisition hardware, one USB-6221 and two USB-9211 modules, the maximum number of simultaneous measurements is 16, eight of which must be thermocouples, while the remaining eight can be thermocouples of heat flux sensors. The setup used for the experiments is shown in Figure 4-9 and described in Table 4-2 and Table 4-3.

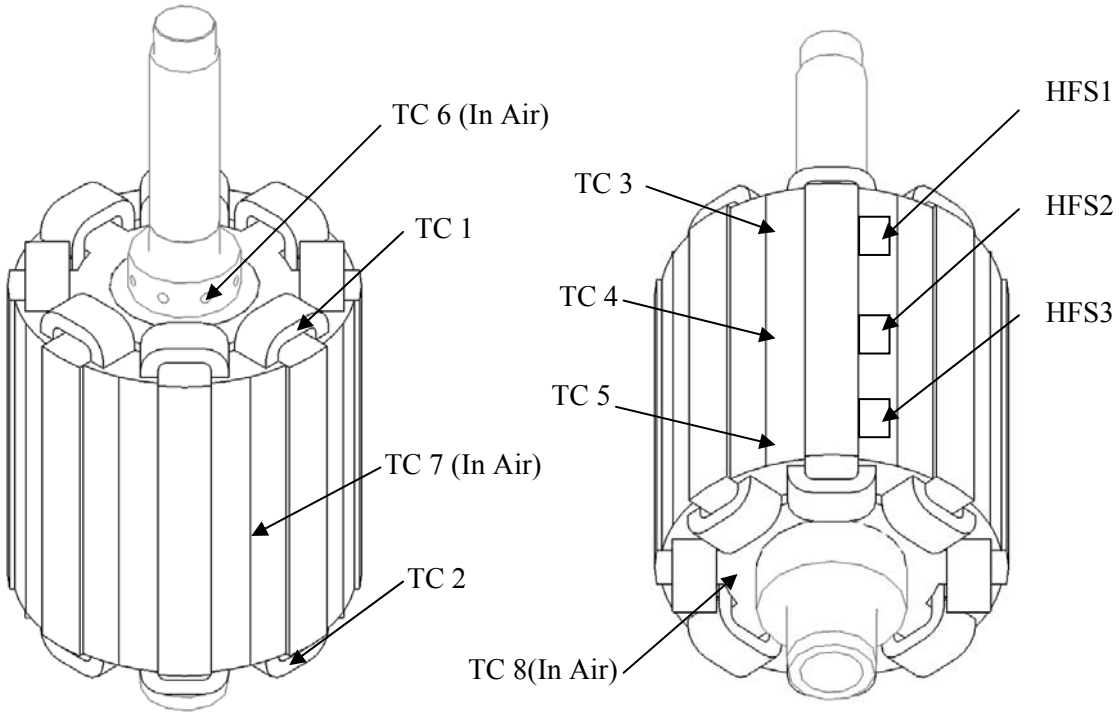

Figure 4-9: Thermocouple and heat flux sensor locations

Table 4-2: Thermocouple Locations

Sensor	Location	Description
TC1	Coil Top	Warm spot
TC2	Coil Bottom	Presumed hottest location

TC3	Epoxy Top	Used with top heat flux sensor
TC4	Epoxy Mid	Used with middle heat flux sensor
TC5	Epoxy Bottom	Used with bottom heat flux sensor
TC6	Air Top (Inlet)	Inlet air temperature
TC7	Air Middle (Air Gap)	Ambient temperature for heat flux calculations
TC8	Air Bottom	Ambient at bottom near hottest spot

Table 4-3: Heat Flux Sensor Locations

Sensor	Gain	Location
HFS1	1.78 μV/(W/m^2)	Epoxy Top
HFS2	1.84 μV/(W/m^2)	Epoxy Wedge
HFS3	1.56 μV/(W/m^2)	Epoxy Bottom

4.3.1 Methods of Attachment

In order to attach the thermocouples and heat flux sensors to surfaces in experiments, Kapton™ tape was employed. The tape, manufactured by kaptontape.com, is 68.6 μm (2.7 mils) thick including the silicone adhesive, and is rated for use up to 250°C. The thermal conductivity of Kapton™ varies only slightly between 20°C and 100°C with a nominal value of 1.44 W/m·K based on Boedeker Plastics (2009), and additionally has an emisivity of 0.57 based on Electro Optical Industries (2009). This combines for a thermal resistance of 4.76 $\times 10^{-5}$ m²K/W.

To ensure good heat flow from surfaces to thermocouples and heat flux sensors, a thermal paste was employed. The paste used was a silicone grease, type OT-201-2 from Omega Engineering, Inc., which offers a high thermal conductivity of 2.3 W/m·K, and is formulated for temporary bonds at temperatures between -40°C and 200°C.

Chapter 5

Thermal Model Completion through Experiment

The lumped parameter thermal model was developed based on dimensional information and material properties. In order to determine the accuracy of this approach, experiments were performed to gain an understanding of the actual performance of the motor in a laboratory environment.

5.1 Approach

For the thermal model, there are two important numerical inputs: the current and the flowrate. In order to validate the model using experimental data, three different current levels were used and each was tested under three different coolant flow rates. These same inputs were then applied to the thermal model so the results could be compared.

5.1.1 Experimental Current Level

At the time of the experiments, it was not possible to specify a desired current level, however the speed and duty cycle could be set which resulted in a unique, repeatable waveform from which the RMS current could be found. The three waveforms had nominal peaks of 30 A, 40

A and 60 A, as can be seen in Figure 5-1 which shows the current waveforms as output by the control VI.

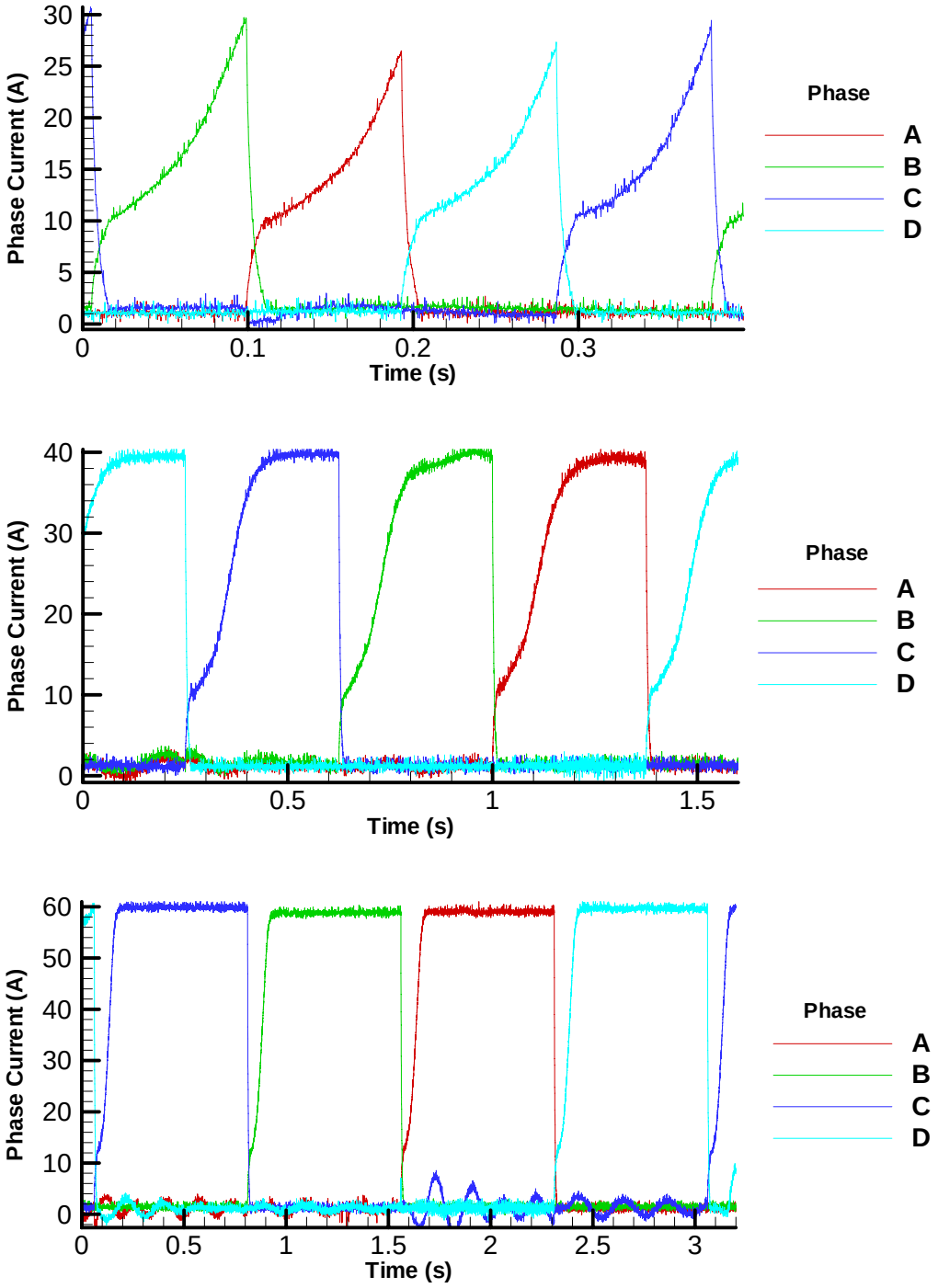

Figure 5-1: Waveforms for Low (Top), Medium (Middle), and High Current (Bottom)

In order to determine the effective current of each waveform, the RMS current must be found. For discrete data, the RMS currents for the three waveforms was found using

$$I_{rms} = \sqrt{\frac{1}{n}\sum_{m=1}^{n} i_m^{\,2}}, \tag{5-1}$$

evaluated over one period. The three currents each had different periods, as determined by the field speed, which is detailed in Table 5-1. The sampling rate for the current was 5 kHz, which corresponds to 1875, 7500, and 15,000 samples for the low, medium and high currents respectively. Solving (5-1) using MATLAB, RMS currents of 8.4 A, 16.4 A, and 28.2 A were found. It should be noted that there was noise present during testing, best exemplified by phase C between 1.5 and 3.0 seconds in the high-current case of Figure 5-1, hence the waveforms deviate from the ideal. Additionally, in the low current case, significant difference in the peak values of each phase can be seen. The RMS current values were found for each phase, and the average value is what will be used in the model.

Table 5-1: Summary of input currents

Level	Current		Field Speed	Period	Duty Cycle
	A, Nominal	A, RMS	RPM	s	%
Low	30	8.4	80	0.375	29
Medium	40	16.4	20	1.5	26
High	60	28.2	10	3.0	37

5.1.2 Experimental Airflow Level

Similar to the current, three levels of cooling were also used. For a baseline, no cooling airflow was provided which represents the minimum amount of cooling, and corresponds to the maximum temperatures for each current. Two levels of airflow were used to generate data about forced convective cooling, a low flowrate of 10.7 CFM, and a high rate of 24.4 CFM. Throughout the experiments the airflow was recorded, and a maximum deviation of 1.56% from the average was recorded over the six test cases with forced cooling.

5.2 Motor Experiments

In order to assess the validity, and improve of the thermal model, data from the motor performance was collected. Each experiment consists of two phases: heating-up and cooling-down. The heating up phase lasted either 2.5 hours, or until the highest temperature reading was 85°C. For the six experiments at low and medium current, the heating phase lasted the full 2.5 hours, while for the high current case the maximum allowable temperature was reached between half and one hour. The duration of the cool-down phase varied. Several experiments were left to cool down overnight, allowing the motor to return to thermal equilibrium with the environment, while other experiments were allowed to cool to approximately 5°C above ambient in order to maximize the number of experiments that could be fit into the limited time for experimentation.

5.2.1 Results

Each experiment generated a history of the temperatures at five surface locations of the motor, a sample of which can be seen in Figure 5-2, and at three locations in the air within the motor. The most important of the measured temperatures is the maximum of those recorded. Depending on the experiment, the highest temperatures occurred either at the bottom of the coil, or at the bottom for the epoxy, two close locations both furthest away from the cooling airflow. For purposes of preliminary model validation, the temperatures at the bottom of the coil were considered; advanced validation incorporated the other temperature readings. One reason for the choice to consider only the coil bottom temperatures at first is because the thermal model has the resolution to output this temperature accurately, whereas the epoxy segment is not subdivided into three. Another reason for this selection is due to the lower amount of noise present on the signal. It can be seen from Figure 5-2 that a significant amount of noise was recorded on some signals during the experiments. At its greatest extent, the noise resulted in a fluctuation of 10°C. The noise on the signals is discussed in Section 5.2.2.

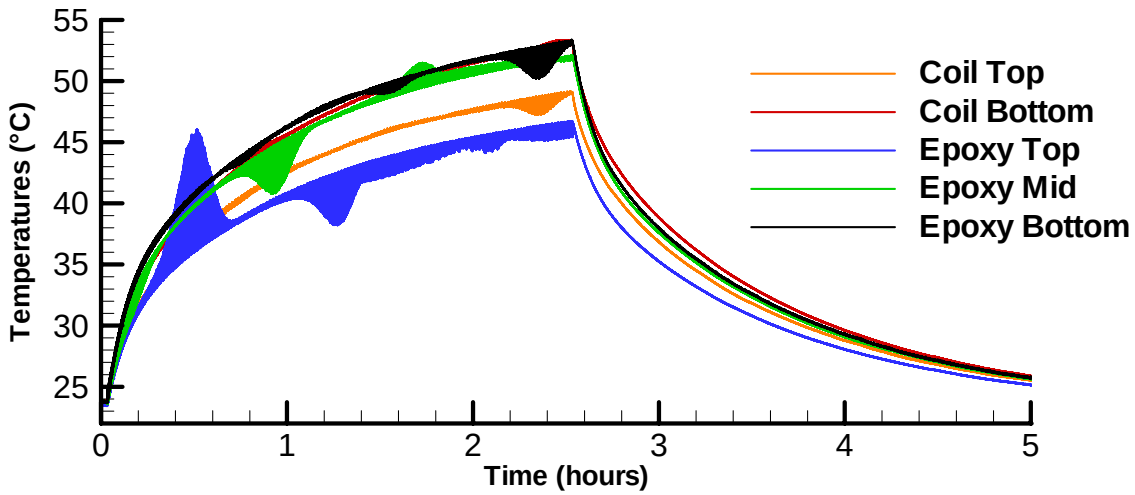

Figure 5-2: Sample of thermal data from medium current, high cooling experiment

Each experiment was begun with the motor at different temperatures, as is summarized in Table 5-2. In order to provide a common metric for comparison, it is useful to find an offset time to shift the curves such that they all share a common starting temperature. In order to determine this offset time, an exponential curve fit of the form

$$T_i(t) = a_i e^{b_i \cdot t} + c_i e^{d_i \cdot t}, \tag{5-2}$$

was applied to the first fifteen minutes of data, or 1800 data points, for the bottom of the coils. From the curve fits, the time at which the temperature of the bottom coils was, or would have been 22.8°C was found, and is listed in Table 5-2.

Table 5-2: Summary of heating portion of experiments

Experiment	Current	Airflow (CFM)	Average Initial Temperature (°C)	Offset Time (s)
1	Low	0 (Natural)	22.8	+31.94
2	Low	10.7	23.4	-71.17
3	Low	24.4	22.9	+1.45
4	Medium	0 (Natural)	25.8	-115.50
5	Medium	10.6	25.1	-80.38
6	Medium	24.4	23.6	-42.43
7	High	0 (Natural)	26.8	-28.88
8	High	10.7	28.4	-79.52
9	High	24.4	23.4	-12.54

With the offset times determined, the temperature plots from the nine experiments can be made.

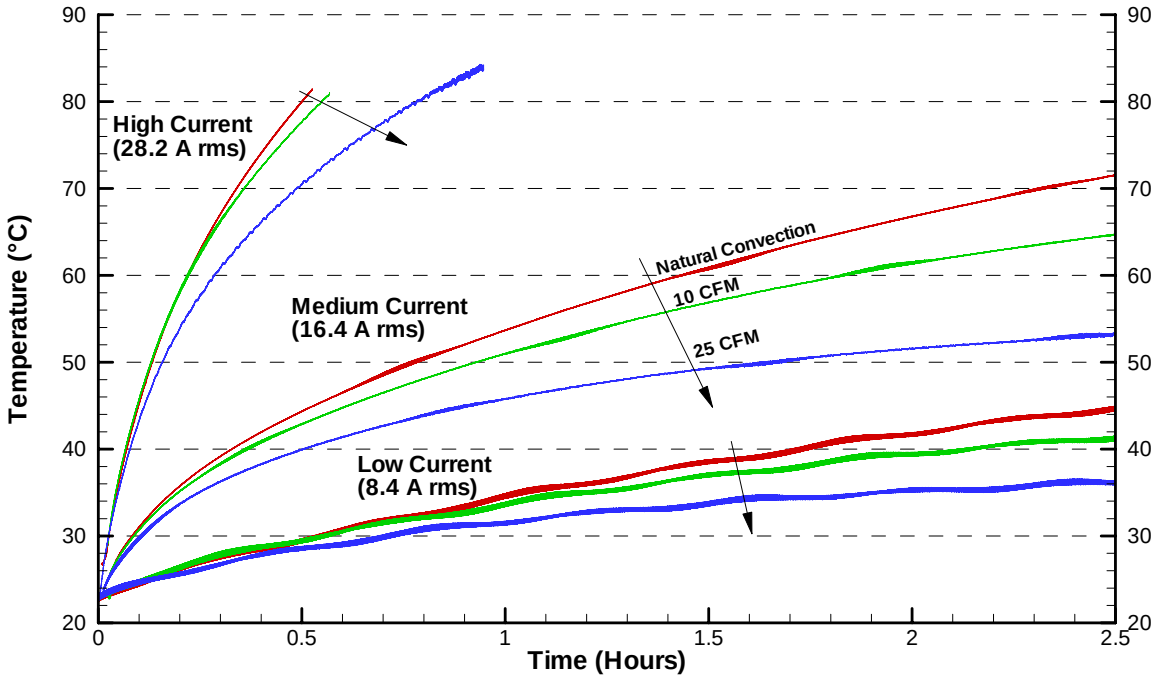

Figure 5-3: Coil bottom temperatures during heat-up phase of experiments

5.2.2 Noise

The noise present in the thermocouple measurements is a consequence of operating thermocouples in an environment with time-varying magnetic fields and of the fact that the thermocouples were not shielded. What is interesting about the noise is that it is present despite the filtering built-into the USB-9211A thermocouple DAQ module. Examining a single noisy signal, seen in Figure 5-4, it can be seen that there are three distinct signals, the high and low signals as well as a signal in between which is believed to be the true temperature measurement.

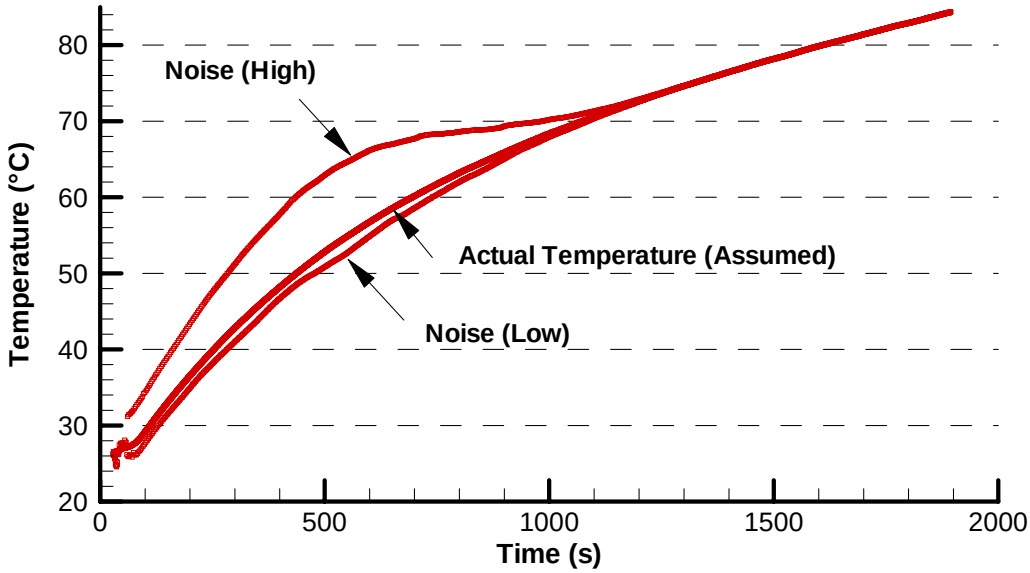

Figure 5-4: Noisy signal from high current (10 RPM field speed), no cooling experiment

The tri-form noise signal was not typical however, there was a definite relation between the motor speed and the type and frequency of noise. Figure 5-5 and Figure 5-6 show typical noise experienced during runs with the other current waveforms.

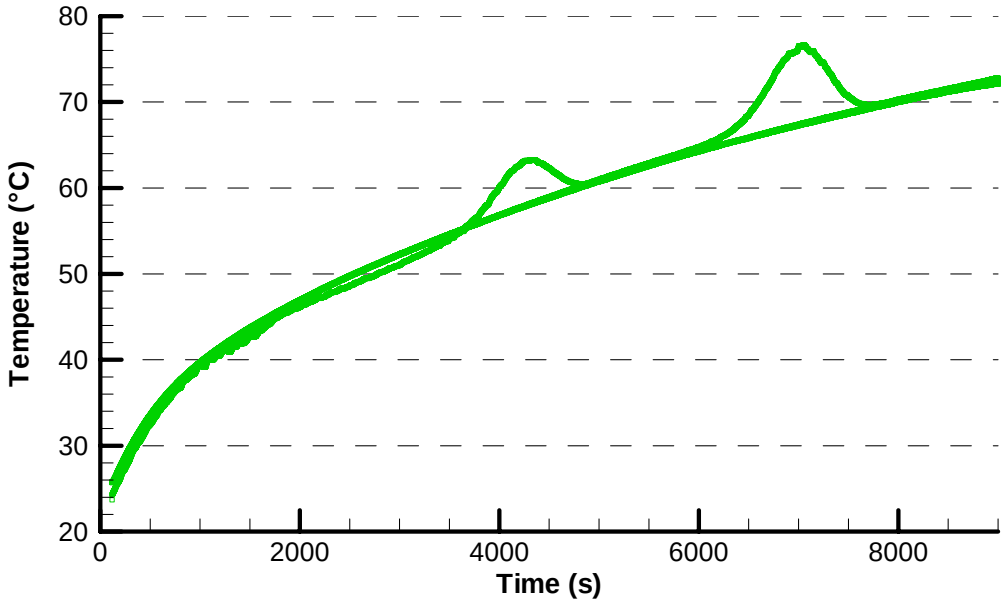

Figure 5-5: Noisy signal from medium current (20 RPM field speed), no cooling experiment

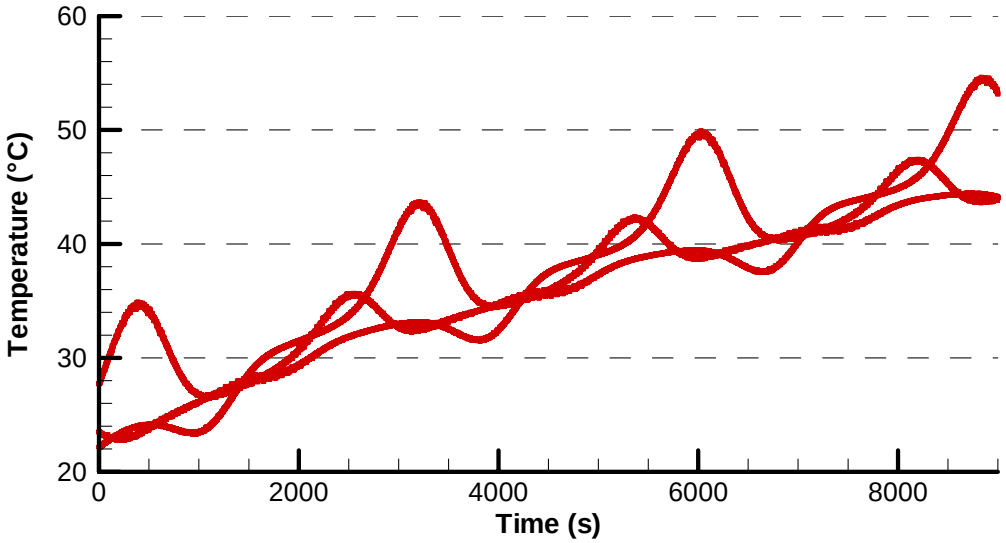

Figure 5-6: Noisy signal from low current (80 RPM field speed), no cooling experiment

The presence of noise on the signal obscures the true temperature, however there are methods to compensate for this. An example of a real-time application would be that the VI to monitor the motor's temperature employed a time-averaging filter to smooth the

temperature waveform to improve the accuracy of the temperature display. For post processing, the waveforms can be analyzed to find the true temperature, which should lie within the extremes that result in the noisy signal. This can be accomplished either by inspection, as seen in Figure 5-4, or through the use of filtering such as time-averaging or software low-pass filters. More work is required to fully address the noise issue, however.

5.2.3 Quantifying Experimental Error

One source of error that arises is at the thermocouple itself, where the thermocouple itself is not in thermal equilibrium with its surroundings as a result of the flow of heat. If conduction through the lead wires is neglected, a thermocouple can be modeled as a small sphere. This can be considered based on the low diameter wire gage of the thermocouple, and also based on the assumption that the temperature of the wires is constant near the junction, resulting in negligible heat transfer. There are two cases of interest, one in which the thermocouple is mounted to a surface, and the other where it is exposed in air.

If an energy balance on the thermal paste used to attach the thermocouple at T_{TC} to a surface at T_s is considered, the actual surface temperature can be found to be

$$T_s = T_{TC} + q'' \frac{\delta_{paste}}{k_{paste}}, \tag{5-3}$$

where q'' is the heat flux passing from the surface through the paste into the thermocouple. The heat flux can be found to be

$$q'' = \left(T_{TC} - T_{air}\right)\left[\frac{\delta_{paste}}{k_{paste}} + \frac{\delta_{tape}}{k_{tape}} + \frac{1}{h}\right]^{-1}, \tag{5-4}$$

where h is the sum of the convective and radiative heat transfer coefficients. Based on the properties of the Kapton tape and thermal paste presented in Section 4.3.1, a large assumed thermal paste thickness of 1 mm and h of 20 W/m²K, a relationship of the form

$$T_s = T_{TC} + \left(T_{TC} - T_{air}\right) \cdot 8.61 \times 10^{-3} (°C)^{-1}. \tag{5-5}$$

was found. Based on an extreme temperature difference between the surface and the air where the surface is at 80°C and the air is at 20°C, a difference between the actual temperature and the thermocouple temperature of 0.516°C was found.

If an energy balance is performed on a thermocouple at a uniform temperature T_{TC} in the air, the resulting equation

$$h\pi d^2\left(T_{air,actual} - T_{TC}\right) = \varepsilon\sigma\pi d^2\left(T_{TC}^4 - T_{surr}^4\right), \quad \textbf{(5-6)}$$

can be used to find an equation for the actual air temperature based on the measured temperature,

$$T_{air,actual} = T_{TC} + \frac{\varepsilon\sigma}{h}\left(T_{TC}^4 - T_{surr}^4\right). \quad \textbf{(5-7)}$$

Omega Engineering Inc., the manufacturer of the thermocouples used in the experiments, provided emissivity values for copper summarized in Table 5-3.

Table 5-3: Emissivity values of thermocouple metals

Metal	Highly Polished	Polished	Roughly Polished	Reference
Constantan			0.09	[22]
Copper	0.02	0.03	0.07	[58], [62]

Based on the highest emissivity of 0.09, an assumed convective heat transfer coefficient of 20 W/m²K, and extreme temperatures of 80°C for the surroundings and 20°C for the thermocouple, an error of -2.1°C arises, meaning the air temperature is actually cooler than the reading given by the thermocouple.

5.2.4 Additional Uncertainty

As stated in Section 4.1.1, the thermocouples used were T-type and made from special limit of error wire, which corresponds to a maximum error which is the greater of 0.5°C or 0.4%. The highest temperature recorded was 85°C, which corresponds to a difference between the base and junction of 62.2°C, which gives an error of 0.25°C, hence the uncertainty associated with the thermocouples is 0.5°C.

The thermocouples were read with NI USB-9211A modules, for which National Instruments (2006) presents a graph to quantify the error associated with T-type thermocouples. The maximum temperature error in the range of interest, 22°C to 85°C is 2.3°C, however a typical error of 1.2°C is given. This error is stated to be associated with "gain errors, offset errors, differential and integral nonlinearity, quantization errors, noise errors, and isothermal errors", and it is noted that this error is independent of any error associated with the thermocouple itself.

5.3 Improving the Model based on Preliminary Results

One shortcoming of the initial model, which was recognized when first run against the experimental data, was that the windings heated up too quickly. The reason for this, it was discovered, was that an average temperature was assumed, and the model let the average temperature rise uniformly. In actuality, however, the internal temperature of the windings is higher than the outside temperature, and part of the thermal generation must heat the inside to the hotter internal temperatures. As a result, it was discovered that by increasing the heat capacity of the coils by a factor of two could compensate for this. While an effective solution for this case, the factor of two is not without a basis in the literature. Gerling and Dajaku (2006) propose methods of modeling solids with a heat generation term and suggest that decreasing the loss term by half results in correct central temperature.

Another change which was made to the model was an implementation of a convection correlation which is commonly applied to totally enclosed fan cooled motors. Staton et al. (2005) observe several instances where convective heat transfer coefficients in the end space are found from correlations of the form

$$h = a_1 + a_2 v^{a_3}, \tag{5-8}$$

where a_1 is the convective heat transfer coefficient and a_2 and a_3 are two additional factors which control how the local velocity v affects the heat transfer. Because the local convective heat transfer coefficients were found based on dimensional information, a modification of this approach was used, where

$$\left[h_{fc}\right] = a_{1\,fc}\left[h_{fc,geom}\right], \tag{5-9}$$

and

$$\left[h_c\right] = \left(a_{c,1} + a_{c,2} CFM^{\,a_{c,3}}\right)\left[h_{c,geom}\right], \tag{5-10}$$

where CFM represents the volume flow rate of the cooling air in cubic feet per minute. This is a reasonable correction factor given that without the correction the free convection coefficients are on the order of 5 W/m²K to 8 W/m²K, while Staton et al. (2005) present coefficients ranging from 15 W/m²K to as high as 40 W/m²K. Based on curve fitting, the following coefficients were found:

$a_{fc} = 3.5$ $\quad$ $a_{c,1} = -0.03196$

$a_{c,2} = 0.21517$

$a_{c,3} = 0.82812$

The curve fits yield a forced convection correction factor of 0 at 0.1 CFM, the value used for free convective simulations. The use of this correction factor is similar to the approach used by Boglietti et al. (2005) where the geometrically determined heat transfer coefficients were multiplied to match model predictions to experimental data. One reason when the factor is higher in this work, up to 3.5, than in Boglietti et al. (2005) which has factors up to 1.95, could be due to the motion of the flexible spline component of the motor which disrupts the boundary layers of the adjacent flow, enhancing the heat transfer.

5.4 Comparison of Models to Experimental Results

With the thermal capacitance and convection modifiers integrated in the thermal model, the model is complete and can now be compared to the experimental results. Based on the model presented in Appendix D, curve fits are presented in Figure 5-7 for the nine cases organized by constant cooling which shows very good agreement between the predictions and the experimental data. It can be seen that the model over-predicts temperatures during high-current runs, while under-predicting temperatures for low-current runs. This is preferable to the opposite because a degree of safety is introduced for higher-current runs as a result, while lower current operation never reaches dangerous temperatures.

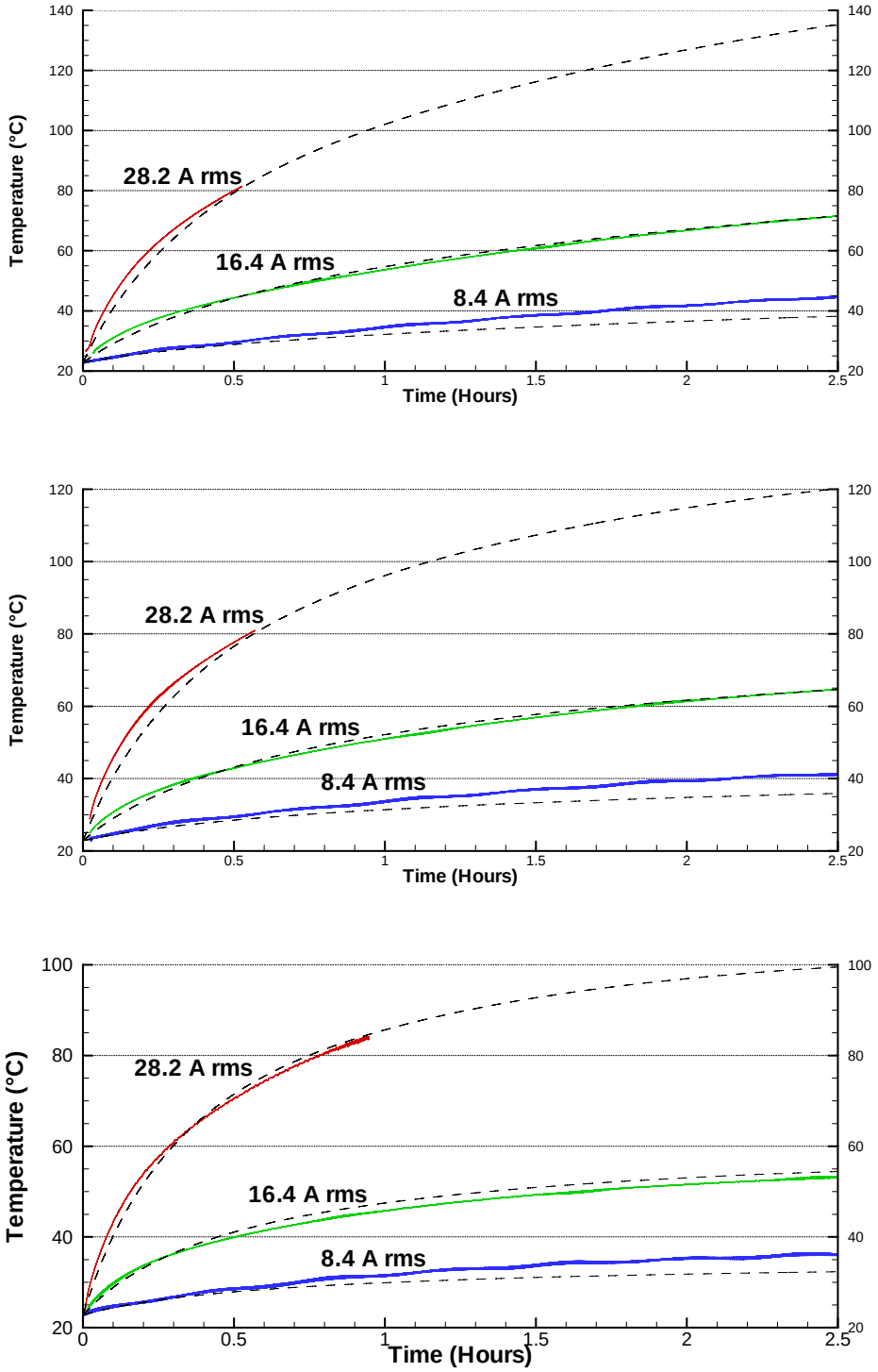

Figure 5-7: Comparison of model predictions (dashed lines) to results with natural cooling (top), forced cooling at 10.7 CFM (middle), and 24.4 CFM (bottom)

An alternative view of the model's predictions can be obtained by looking at the cases with constant current.

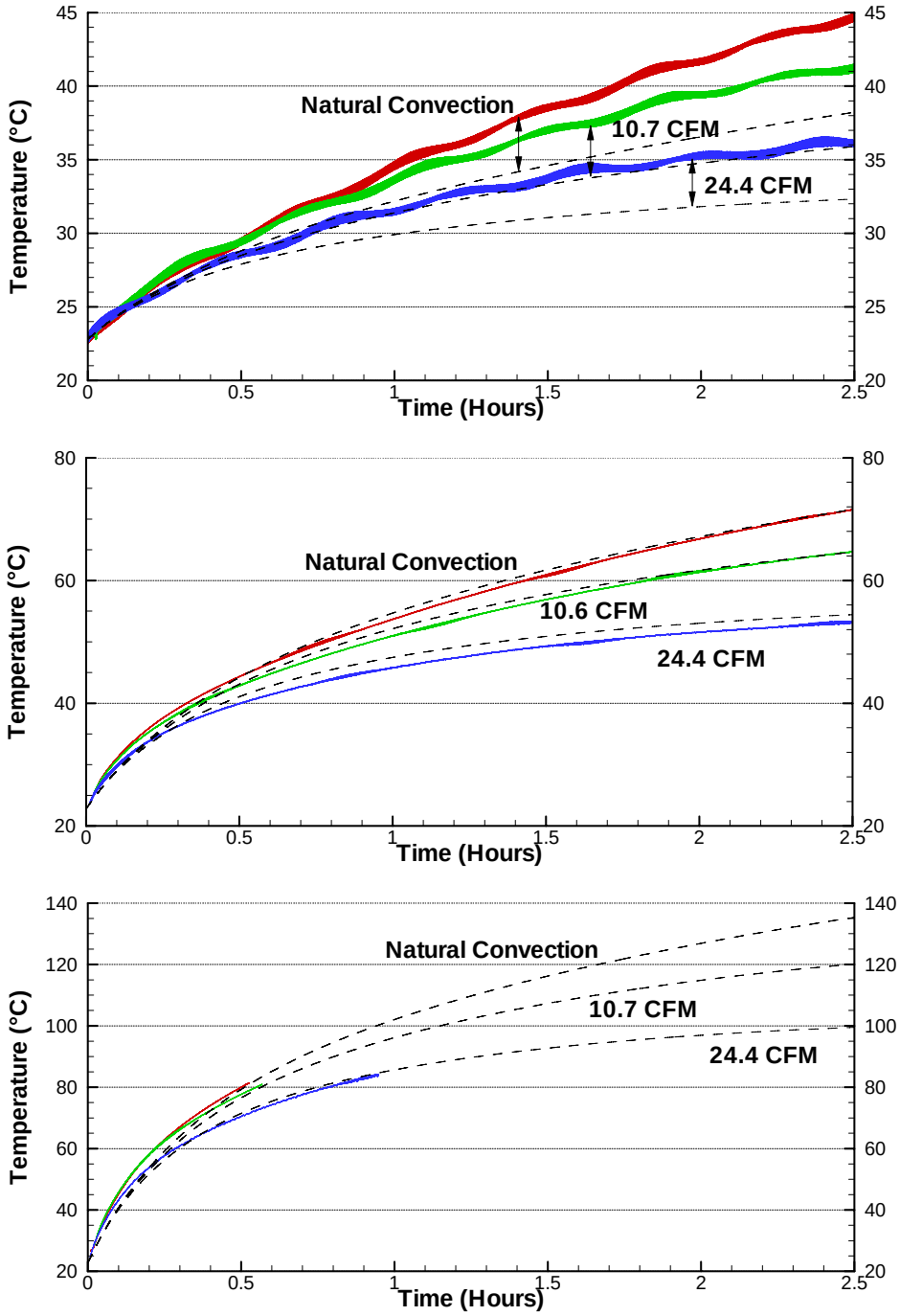

Figure 5-8: Comparison of model predictions (dashed lines) to results at low current, 8.4 A_{rms} (top), medium current, 16.4 A_{rms} (middle), and high current, 28.2 A_{rms} (bottom)

It can be seen from Figure 5-8 that the low current case has the greatest error as a percentage of the temperature rise. The maximum difference between the model's predictions and the experimental results are summarized in Table 5-4.

Table 5-4: Deviation of model from experimental results

Experiment	Max Over (°C)	Max Under (°C)
1	0	-6.1
2	0	-5.0
3	0	-4.5
4	1.1	-2.0
5	1.2	-1.8
6	4.5	-1.2
7	-0.9	-4.8
8	-1.0	-4.1
9	2.1	-2.5

5.5 Preliminary Sensitivity Analyses

The axial thermal conductivity of M19 was decreased from the regular value of 4.61 W/m·K to 0.371 W/m·K. The difference in temperatures will vary based on the heat generation, however for a significant current of 20 A at a cooling rate of 20 CFM the difference in temperature was 0.4°C, or 0.55% after 2.5 hours, which can be seen in Figure 5-9. This preliminary investigation seems to confirm that the axial thermal conductivity of the stator material does not have a significant impact on the overall temperature rise.

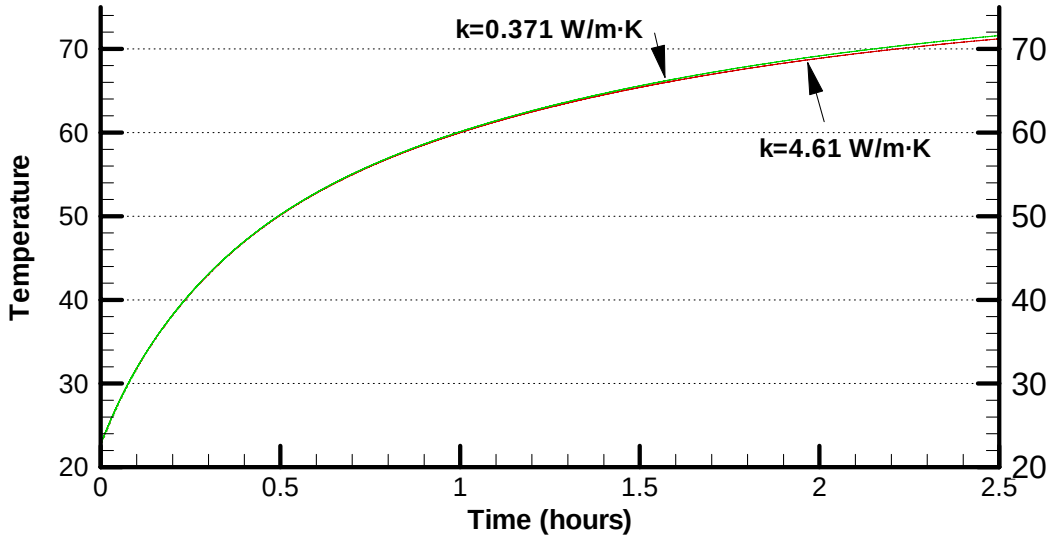

Figure 5-9: Effect of M-19 on peak coil temperature under 20A load with 20 CFM air cooling

Simulations were performed with the contact resistance between most materials equal to $1\times10^{-4}\,m^2K/W$. This was increased by an order of magnitude to $1\times10^{-3}\,m^2K/W$ which was found to increase the peak temperature by 0.05°C, or 0.055%. This preliminary work indicates that the contact resistance due to machine tolerances does not have a significant effect on the maximum temperature.

The contact resistance between the windings and the stator core used for the validation testing was $3\times10^{-2}\,m^2K/W$. This was varied over a range from $1\times10^{-3}\,m^2K/W$ to $1\times10^{-2}\,m^2K/W$, and the effect on the surface temperature at the bottom of the coils can be seen in Figure 5-10. From the based value of $3\times10^{-2}\,m^2K/W$, the range corresponds to an increase in resistance of 67%, to 3% of the value. With an increase in resistance of 67%, the ΔT changes by +2.4%, however if the resistance decreases to 3% ΔT changes by -9.2%, While these changes are large, the range of values for the thermal resistance is also large, hence for the purposes of modeling, an analytic approach to finding $R''_{coil-iron}$ is sufficient.

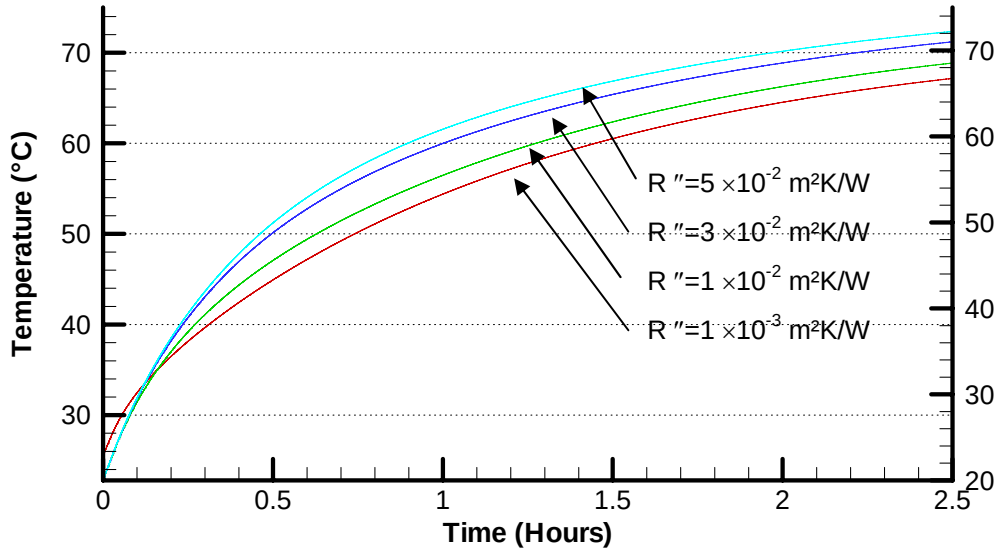

Figure 5-10: Effect of thermal resistance between windings and stator pole on temperature distribution at 20A_{rms} and 20 CFM

The effect of an increased core loss impacted the maximum temperature. The core loss values of 1000 W/m³ and 500 W/m³ for the fieldbooster and stator respectively was increased by a factor of 10 which resulted in an increased temperature of 1.8°C.

Chapter 6

Conclusion

This thesis presents an approach to the thermal modeling of an inner stator type reluctance motor. It has been demonstrated that a lumped parameter thermal model can be developed based on dimensional information that will provide reasonably accurate results over a large range of operating conditions, however completion of the model required experimental data. Since a factor was introduced to increase the convective heat transfer coefficients, care must be taken when applying this model to other motors. Nevertheless, for similar sized motors of similar construction, the developed model should be able to provide an easy first approximation of the time dependant temperature. For the nine test cases for the model, the model was shown to at no point exhibit an absolute error greater than 6.1°C, and it generally shows good agreement with the experimental data.

The tendency of the model to provide more accurate results at higher currents is beneficial for designers looking to find the operational limit of similar motors.

The various sensitivity analyses have demonstrated that future designers do not need to determine exact thermal properties for certain instances, for example the axial stator thermal conductivity in order to accurately predict the temperature.

6.1 Recommendations

There remains considerable work which can be done to validate the thermal model and improve the accuracy of the thermal model. Eight thermocouples were used in the experiments, but the preliminary model was based on only one thermocouple's measurement, the hot-spot. An improved modeling approach which would be more time-intensive would be to attempt to ensure the model's predictions are accurate for each component and segment of air, both for heating-up and cooling-down of the motor, validation which can be aided by the data recorded from the heat flux sensors.

To better quantify the accuracy of the model, curve fits could be applied to the experimental data and the difference between the steady state temperatures predicted by the model and observed in experiments could be analyzed. In addition to the steady-state error, maximum and minimum error, the RMS error could also be useful.

Other work which remains is to validate the model for the holding case. Experiments should be performed with the motor locked to ensure model is accurate for entire range of operation of prototype motor.

The noise present on the measurements remains an issue which must be investigated.

References

[1] 3M, 2004, Epoxy and Hot Melt Adhesives for Electronics, Products and Specifications, Accessed 16-July-2009
http://multimedia.3m.com/mws/mediawebserver?66666UuZjcFSLXTtlXTyMX&XEVuQEcuZgVs6EVs6E666666--

[2] AK STEEL, 2007, Product Data Bulletin: Selection of Electrical Steels for Magnetic Cores, http://www.aksteel.com/pdf/markets_products/electrical/Mag_Cores_Data_Bulletin.pdf

[3] ALBACH, M., DURBAUM, T., BROCKMEYER, A. 1996 Calculating core losses in transformers for arbitrary magnetizing currents, Power Electronics Specialists Conference, PESC '96 Record., 27th Annual IEEE, Volume 2, 23-27 June 1996 pages 1463-1468

[4] ARPACI, V. S., KAO, S.-H., SELAMET, A. 1999 *Introduction to Heat Transfer*, Upper Saddle River, New Jersey: Prentice-Hall.

[5] ARPACI, V. S. & LARSEN, P.S. 1984 *Convection Heat Transfer*, Englewood Cliffs, New Jersey: Prentice-Hall.

[6] AVALLONE, E. A. & BAUMEISTER, T. 1996 *Marks' Standard Handbook for Mechanical Engineers*, New York: McGraw-Hill.

[7] BOEDEKER PLASTICS. DuPont Kapton Polyimide Film Database, Accessed 22-Sept-2009
http://www.boedeker.com/kapton_p.htm

[8] BOGLIETTI, A., CAVAGNINO, A., STATON, D. A. 2008 Determination of Critical Parameters in Electrical Machine Thermal Models, *IEEE Transactions on Industry Applications* **44** (4), 1150–1159.

[9] BOGLIETTI, A., CAVAGNINO, A., PARVIS, M., VALLAN, A. 2006 Evaluation of Radiation Thermal Resistances in Industrial Motors, *IEEE Transactions on Industry Applications* **42** (3), 688–693.

[10] BOGLIETTI, A., CAVAGNINO, A., STATON, D. A. 2005 TEFC induction motors thermal models: a parameter sensitivity analysis, *IEEE Transactions on Industry Applications* **41** (3), 756–763.

[11] BOUSBAINE, A., 1999 Thermal Modelling of Induction Motors Based on Accurate Loss Density Distribution, *Electric Power Components and Systems*, **27** (3), 311–324.

[12] ÇENGEL, Y.A., BOLES, M. A. 2008 *Thermodynamics: An Engineering Approach*, New York: McGraw-Hill.

[13] ÇENGEL, Y.A. 1997 *Introduction to Thermodynamics and Heat Transfer*, New York: Irwin McGraw-Hill.

[14] CHEN, Y., PILLAY, P. 2002 An Improved Formula for Lamination Core Loss Calculations in Machines Operating with High Frequency and High Flux Density Excitation, Industry Applications Conference, 2002. 37th IAS Annual Meeting. Conference Record of the, Volume 2, Issue , 2002 Page(s): 759–766 vol.2

[15] CHURCHILL, S. W., CHU, H. H. S. 1975B Correlating Equations for Laminar and Turbulent Free Convection from a Vertical Plate, *International Journal of Heat and Mass Transfer* **18**, 1323–1329.

[16] CHURCHILL, S. W., CHU, H. H. S. 1975A Correlating Equations for Laminar and Turbulent Free Convection from a Horizontal Cylinder, *International Journal of Heat and Mass Transfer* **18**, 1049–1053.

[17] COMSOL.AB 2005 COMSOL Multiphysics User's Guide,

[18] COTRONICS CORPORATION 2009 Duralco 4525, http://www.cotronics.com/vo/cotr/pdf/4525.pdf

[19] DAVISON, E. 2004 Harmonic Drive Motor, WIPO Patent WO 2004/025815 A1

[20] DRIESEN, J., BELMANS, J.M., HAMEYER, K. 2001 Finite-Element Modeling of Thermal Contact Resistances and Insulation Layers in Electrical Machines, *IEEE Transactions on Industry Applications* **37** (1), 15-20

[21] ENCYCLOPÆDIA BRITANNICA. 2009 Harmonic Drive, In Encyclopædia Britannica Online, Accessed June 2009, http://www.britannica.com/EBchecked/topic/255508/Harmonic-Drive

[22] ELECTRO OPTICAL INDUSTRIES, INC. Emissivity of Materials, Accessed 18-June-2009 http://www.electro-optical.com/html/bb_rad/emissivity/matlemisivty.asp

[23] GERLING, D., DAJAKU, G. 2006 *Thermal Calculation of Systems with Distributed Heat Generation,* Thermal and Thermomechanical Phenomena in Electronic Systems, ITHERM '06, The Tenth Intersociety Conference on, 645-652.

[24] GNIELINSKI, V. 1976 *New equations for heat and mass transfer in turbulent pipe and channel flow,* International Chemical Engineering, **16**, 359-368

[25] GRADZKI, P. M., JOVANOVIC, M. M., LEE, F. C. 1990 Computer aided design for high-frequency power transformers, IEEE APEC'90, pp. 336-343.

[26] GREENBERG, M.D. 1998 *Advanced Engineering Mathematics*, Upper Saddle River, New Jersey: Prentice Hall.

[27] GUO, Y. G., ZHU, J. G., WU, W. 2005 Thermal analysis of soft magnetic composite motors using a hybrid model with distributed heat sources, *IEEE Transactions on Magnetics* **41** (6), 2124–2128.

[28] HAALAND, S.E. 1983 Simple and Explicit Formulas for the Friction Factor in Turbulent Pipe Flows, *Journal of Fluids Engineering* **105** (1), 89–90.

[29] HAYASHI, Y., MILLER, T. J. 1995 A New Approach to Calculating Core Losses in the SRM, *IEEE Transactions on Industry Applications* **31** (5), 1039–1046.

[30] HENNEN, M. D., DE DONCKER, R. W., Comparison of Outer- and Inner-Rotor Switched Reluctance Machines, Power Electronics and Drive Systems, 2007. PEDS '07. 7th International Conference on, November 2007, pp 702-706

[31] HUANG, Y., LI, K., & HU, Q., YYYY Research on Computational Model of Iron Losses in SPWM Fed Induction Motors, Electrical Machines and Systems, 2005. ICEMS 2005. Proceedings of the Eighth International Conference on Publication Date: 29-29 Sept. 2005 Volume: 3, On page(s): 2002-2004 Vol. 3

[32] HUANG, Y., ZHU, J., GUO, Y., HU, Q., 2007 Core Loss and Thermal Behavior of High-Speed SMC Motor Based on 3-D FEA. Electric Machines & Drives Conference, IEMDC '07. IEEE International Volume 2, 3-5 May 2007 Page(s):1569 – 1573

[33] HUKSEFLUX THERMAL SENSORS, Heat Flux Measurements, http://www.hukseflux.com/thermalScience/heatFlux.html, Accessed 16 October 2008

[34] INCROPERA, F.P., DEWITT, D.P. 2002 *Fundamentals of Heat and Mass Transfer*, John Wiley & Sons.

[35] JANNA, W.S. 1988 *Engineering Heat Transfer*, New York: Van Nostand.

[36] KAPTONTAPE.COM. 2009 *1 Mil Polyimide Tapes Technical Data Sheet*, Accessed 22-Sept-2009 http://www.kaptontape.com/1mil_polyimide_sheets.php

[37] KRISHNAN, R. 2001 *Switched Reluctance Motor Drives*, CRC Press.

[38] KUESER, P.E. ET AL. 1965 *Research and Development Program on Magnetic Electrical Conductor, Electrical Insulation, and Bore Seal Materials*, NASA Lewis Research Center, Contract NAS3-4162.

[39] LEE, Y., HAHN, S.-Y., KAUH, S. K. 2000 Thermal Analysis of Induction Motor with Forced Cooling Channels, *IEEE Transactions on Magnetics* **36** (4), 1398–1402

[40] LUSSIER, D.T., ORMISTON, S.J., MARKO, R. MK. 2003 Theoretical Determination of Anisotropic Effective Thermal Conductivity in Transformer Windings, *International Communications on Heat and Mass transfer* **30** (3), 313–322

[41] MA, L., SANADA, M., MORIMOTO, S., TAKEDA, Y. 2003 Prediction of Iron Loss in Rotating Machines With Rotational Loss Included, *IEEE Transactions on Magnetics* **39** (4), 2036–2041

[42] MATVEEV, A., 2006, Development of Methods, Algorithms and Software for Optimal Design of Switched Reluctance Drives, PhD thesis, Technische Universiteit Eindhoven

[43] MATWEB, AISI 1040 Steel, water quenched from 845°C (1550°F), 650°C (1200°F) temper, 100 mm (4 in.) round, accessed 25 February 2009a
http://www.matweb.com/search/DataSheet.aspx?MatGUID=8b41dc3d7f1045fe9350f8bb1dc7783e

[44] MATWEB, AISI 1045 Steel, cold drawn, high temperature, stress relieved, 16-22 mm (0.625-0.875 in) round, accessed 25 February 2009b
http://www.matweb.com/search/DataSheet.aspx?MatGUID=cfc9bdab1dbf4fb19d6b3e5e1be8c9bb

[45] MATWEB, AISI 4340 Steel, oil quenched 845°C, 650°C (1200°F) temper, tested at 25°C (77°F), accessed 25 February 2009c

http://www.matweb.com/search/DataSheet.aspx?MatGUID=55f1ea0232324aef8bccc1ad1db7ad82

[46] MATWEB, Aluminum 6061-T6; 6061-T651, accessed 25 February 2009d

http://www.matweb.com/search/DataSheet.aspx?MatGUID=1b8c06d0ca7c456694c7777d9e10be5b

[47] MELLOR, P. H., ROBERTS, D., TURNER, D. R., Lumped parameter thermal model for electrical machines of TEFC design, IEE Proceedings B, Electric Power Applications, Vol. 138, Issue 5, September 1991

[48] MG CHEMICALS, Thermally Conductive Epoxy Encapsulating & Potting Compound, accessed 26 February 2009a, http://www.mgchemicals.com/products/832tc.html

[49] MG CHEMICALS, High Temperature Epoxy Encapsulating and Potting Compound, accessed 26 February 2009b, http://www.mgchemicals.com/products/832ht.html

[50] MOTOR DESIGN LTD. 2009 Motor-CAD v5.1 Release,

http://www.motor-design.com/downloads/Motor-CAD_v5.pdf

[51] MOTOR DESIGN LTD. 2007 SPEED Software,

http://www.motor-design.com/downloads/SPEED_Software%20Leaflet.pdf

[52] MTHOMBENI, T. L., PILLAY, P. 2005 Lamination Core Losses in Motors with Non-sinusoidal Excitation with Particular Reference to PWM and SRM Excitation Waveforms, *IEEE Transactions on Energy Conversion* **20** (4), 836-843.

[53] MTHOMBENI, L. T., PILLAY, P., SINGAMPALLI, N. A. 2003 Lamination Core Loss Measurements in Machines Operating with PWM or Non-sinusoidal Excitation, Electric Machines and Drives Conference, 2003. IEMDC'03. IEEE International , Volume 2, pp. 742-746

[54] NATIONAL INSTRUMENTS. 2006B Operating Instructions NI 9211 4-Channel Thermocouple Input Module.

[55] NATIONAL INSTRUMENTS. 2006A NI 622x Specifications.

[56] NATIONAL INSTRUMENTS. 2009A NI USB-9211A – Portable USB-Based DAQ for Thermocoupels, Accessed on 21-May-2009, http://sine.ni.com/nips/cds/view/p/lang/en/nid/201881.

[57] NATIONAL INSTRUMENTS. 2009B M Series Multifunction DAQ for USB – 16-Bit, 250 kS/s, up to 80 Analog Inputs – Data Sheet – National Instruments, Accessed on 21-May-2009, http://sine.ni.com/ds/app/doc/p/id/ds-10/lang/en.

[58] OMEGA ENGINEERING INC., 2009b, Color Codes for Thermocouples, Wire and Connectors, tolerances, special limits of error, reference guide, accessed 7-June-2009,

http://www.omega.com/toc_asp/frameset.html?book=Temperature&file=TC_GEN_SPECS_REF

[59] OMEGA ENGINEERING INC. 2009a, Flow Meter Process Control Information Systems, Accessed on 08-July-2009, http://www.omega.com/ppt/pptsc.asp?ref=FLR-D

[60] OMEGA ENGINEERING INC., 2008, Omega Engineering Heat Flux Sensor Calibration Report

[61] OMEGA ENGINEERING INC. 2005, User's Guide: FLR5000, 6000, 7000, 8000, and 9000 SERIES Flow Transmitter

[62] OMEGA ENGINEERING INC., Emissivity of Common Materials, Accessed on 05-March-2009

http://www.omega.com/literature/transactions/volume1/emissivitya.html

[63] OMEGA ENGINEERING INC., High Temperature and High Thermally Conductive Paste,

http://www.omega.com/Temperature/pdf/OT-201.pdf

[64] OMEGA ENGINEERING INC., Ready-Made Insulated Thermocouples with Stripped Leads

http://www.omega.com/Temperature/pdf/5TC.pdf

[65] OMEGA ENGINEERING INC., Thin-Film Heat Flux Sensors

http://www.omega.com/Temperature/pdf/HFS-3_HFS-4.pdf

[66] REINERT, J., BROCKMEYER, A., DE DONCKER, R. W. A. A. 2001 Calculation of Losses in Ferro- and Ferrimagnetic Materials Based on the Modified Steinmetz Equation, *IEEE Transactions on Industry Applications* **37** (4), 1055–1061.

[67] ROUHANI, H., FAIZ, J., LUCAS, C. 2007 Lumped thermal model for switched reluctance motor applied to mechanical design optimization, *Mathematical and Computer Modelling* **45** (5-6), 625–638.

[68] RYFF, P. F. 1994, *Electric Machinery*, Upper Saddle River, New Jersey: Prentice Hall Career and Technology.

[69] SCOWBY, S. T., DOBSON, R. T., KAMPER, M. J. 2004 Thermal modelling of an axial flux permanent magnet machine, *Applied Thermal Engineering* **24**, 193–207.

[70] SEVERNS, R., HF-core losses for non-sinusoidal waveforms, Proc. HFPC, 1991, pp. 140-148

[71] SPRAGUE, S., Magnetic Materials Comparison Version 2.0a, Lamination Steels Charting Program, Proto Laminations, Inc., 30 January 1999

[72] SPRAGUE, S. 2009, Personal Communication, Re: M19 Properties - Questions, February

[73] SPARROW, E.M., GREGG, J.L. 1956 Laminar Free Convection from a Vertical Flat Plate, *Transactions of the ASME*, 78, 435

[74] SPRUNG-BRETT RDI. 2007 High Torque High Efficiency Motor, STTR Phase 1 Final Report

[75] SPRUNG-BRETT RDI. 2008 High Torque High Efficiency Motor, STTR Phase 2 Design Review Report

[76] STATON, D. A., CAVAGNINO, A. 2006 Convective Heat Transfer and Flow Calculations Suitable for Analytical Modelling of Electric Machines, *IEEE Industrial Electronics, IECON 2006 – 32nd Annual Conference on*, 4841-4846

[77] STATON, D., BOGLIETTI, A. & CAVAGNINO, A. 2005 Solving the More Difficult Aspects of Electric Motor Thermal Analysis in Small and Medium Size Industrial Induction Motors. *IEEE Transactions on Energy Conversion*, **20** (3), 620–628.

[78] THOMPSON, K., 2009 Personal Conversation, 3M Electronic Markets Materials Division, Technical Support, February.

[79] TOULOUKIAN, Y.S. 1967 Thermophysical properties of high temperature solid materials

[80] TRIGEOL, J.-F., BERTIN, Y., LAGONOTTE, P. 2006B Coupling control volume modeling in fluid and lumped thermal model – Application to an induction machine, *IEEE Industrial Electronics, IECON 2006 - 32nd Annual Conference on*, 4829 – 4834

[81] TRIGEOL, J.-F., BERTIN, Y., LAGONOTTE, P. 2006A Thermal Modeling of an Induction Machine Through the Association of Two Numerical Approaches, *IEEE Transactions on Energy Conversion*, **21** (2), 314-323

[82] TUTTLE, T.D. 1992 Understanding and Modeling the Behavior of a Harmonic Drive Gear Transmission, Masters thesis, Massachusetts Institute of Technology

[83] VALENTICH, J. 1965 New Values for Thermal Coefficients, *Product Engineering* **36** (15) 63-71

[84] WERE, M. 1996 Analysis and Control of Kinematic Error in Harmonic Gear Drive Mechanisms, Masters thesis, Rice University

[85] YOON, M.K., JEON, C.S., KAUH, S.K. 2002 Efficiency Increase of an Induction Motor by Improving Cooling Performance, *IEEE Transactions on Energy Conversion* **17** (1), 1–6.

Appendix A

Fourier Series Analysis of SRM Current Waveform

In order to incorporate the switched reluctance motor current waveform into various stages of the modelling, it was necessary to decompose the waveform using a Fourier series analysis. This approach transforms a periodic

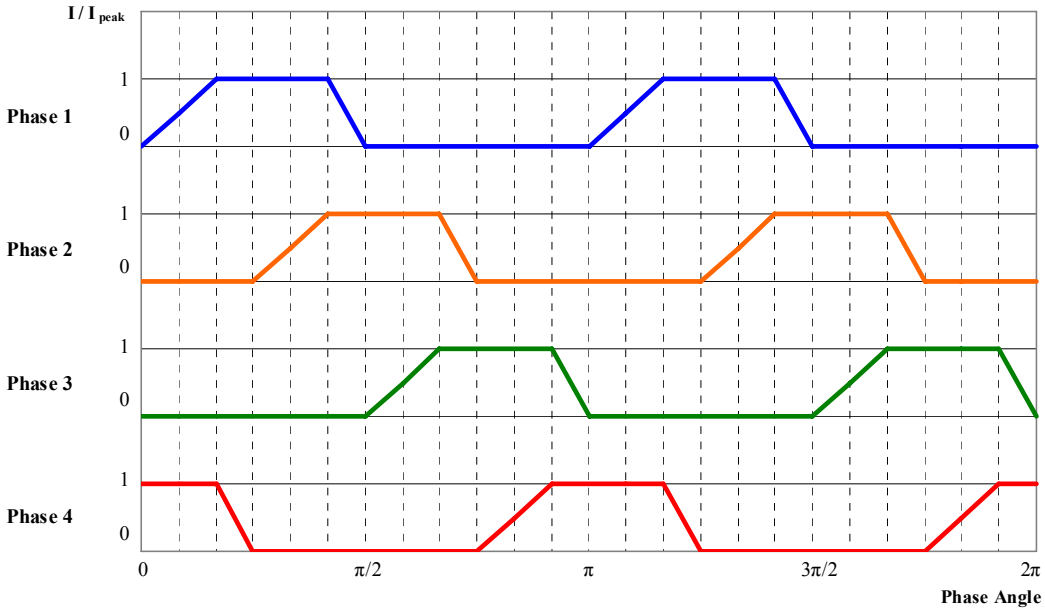

Figure A-1: Switched reluctance motor current waveform

Appendix A Fourier Series Analysis of SRM Current Waveform

The analysis begins with a Fourier series analysis of the normalized SRM current waveform. From Greenberg (1998), the Fourier series of a function *f(θ)* which is periodic on an interval of 2π is defined as

$$FS\ f = a_0 + \sum_{n=1}^{\infty} \left[a_n \cos(n\theta) + b_n \sin(n\theta) \right], \tag{A-1}$$

where the coefficients are

$$a_0 = \int_{-\pi}^{\pi} f(\theta) d\theta\,, \tag{A-2}$$

$$a_n = \int_{-\pi}^{\pi} f(\theta) \cos(n\theta) d\theta\,, \tag{A-3}$$

$$b_n = \int_{-\pi}^{\pi} f(\theta) \sin(n\theta) d\theta\,. \tag{A-4}$$

For a given mode, there is a sine and a cosine component of magnitudes a_n and b_n. Because these waves are π/2 radians out of phase, the magnitudes of two components can be summed using the Pythagorean Theorem to find the modal magnitude

$$M_n = \sqrt{a_n^2 + b_n^2}\,. \tag{A-5}$$

The modal magnitude M_n for the SRM flux density waveform is plotted in Figure C-3. It should be noted that a_0 represents the average value of the waveform.

Appendix A Fourier Series Analysis of SRM Current Waveform

First, a Fourier series analysis of the normalized SRM current waveform was performed, the results of which can be seen in Figure A-2. The modal decay is quite rapid, with all modal magnitudes greater than 1% of the total occurring at or before the 16th mode, and 0.1% by the 64th mode.

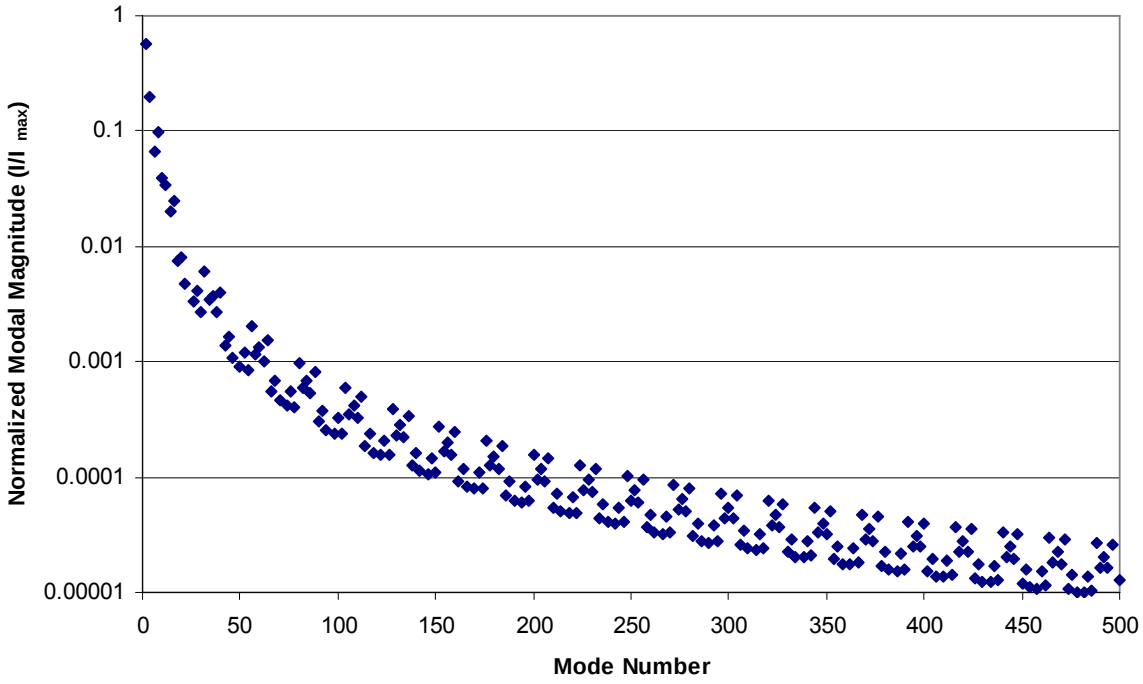

Figure A-2: Model magnitudes for SRM current waveform

Appendix B

Core Loss Model

The data used to construct a model of the core loss was provided by Proto Laminations Inc., the company which fabricated the laminations in the prototype motor. The data was in the form of a graph, seen in Figure B-1 below. When displayed on a log-log graph, the log-linear nature of core loss is apparent.

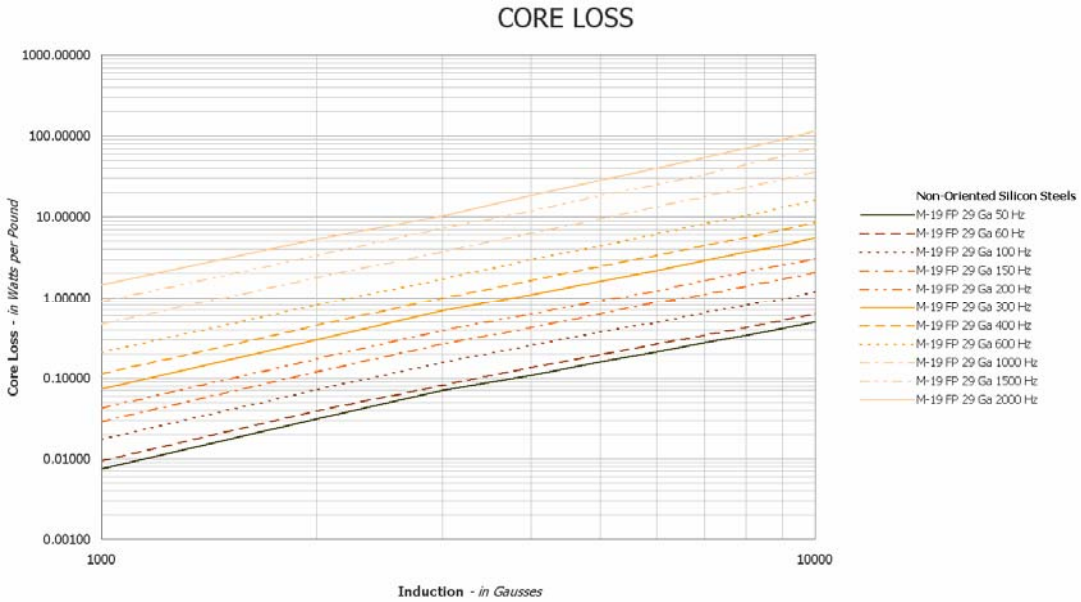

Figure B-1: Core Loss in 29 Ga. M-19 Silicon Steel Undergoing Sinusoidal Excitation of Various Frequencies

Appendix B Core Loss Model

In order to use the core loss data, a model was constructed such that for a sinusoidal flux waveform of given amplitude and frequency, the specific core loss of that waveform could be found. First, data was read from the chart manually at steps of 0.1 T (1 kG) for each curve. The axes of the chart were stepped in very small increments to ensure fidelity of the data for the 167 data points. Next, the specific core loss values were converted from watts per pound to watts per kilogram, and induction was converted from gauss to tesla, and the results were plotted logarithmically as seen in Figure B-2. Next, the tabulated values of log(SCL) and log(B_{max}) were input into CurveFinder 1.3, and a linear model was created for each frequency of the form

$$\log(SCL) = a(f) + b(f) \cdot \log(B_{\max}), \qquad \textbf{(B-6)}$$

where *a(f)* and *b(f)* represent the y-intercept and slope for the linear model, which are said to be functions of the excitation frequency in order to be as general as possible.

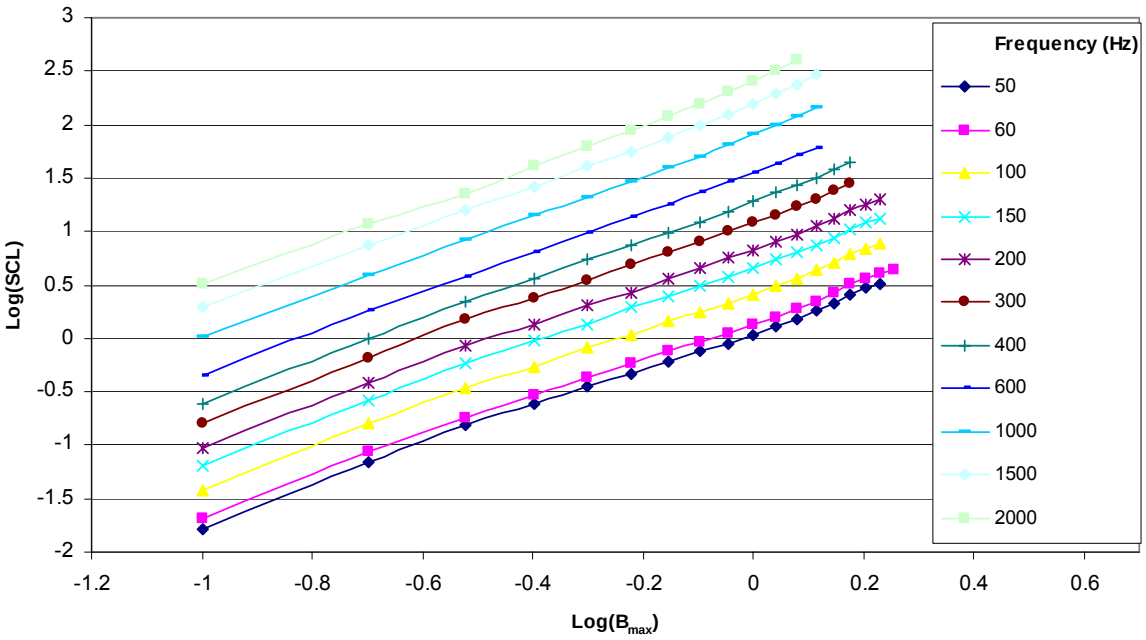

Figure B-2: Linear relationship of log(SCL) vs log(B_{max})

The curve fit produced the coefficients seen in Table B-1. Both the intercept and slope coefficients *a(f)* and *b(f)* varied with the frequency. It was apparent that the coefficients themselves behaved log-linearly, as seen in Figure B-3.

Table B-1: Coefficients of Linear Curve Fit

Frequency (Hz)	***a(f)***	***b(f)***
50	0.068087	1.798666
60	0.164428	1.803993
100	0.441120	1.819716
150	0.679734	1.833585
200	0.853031	1.847676
300	1.099682	1.853894
400	1.290144	1.873660
600	1.557278	1.889650
1000	1.907074	1.901034
1500	2.199378	1.920132
2000	2.396029	1.924784

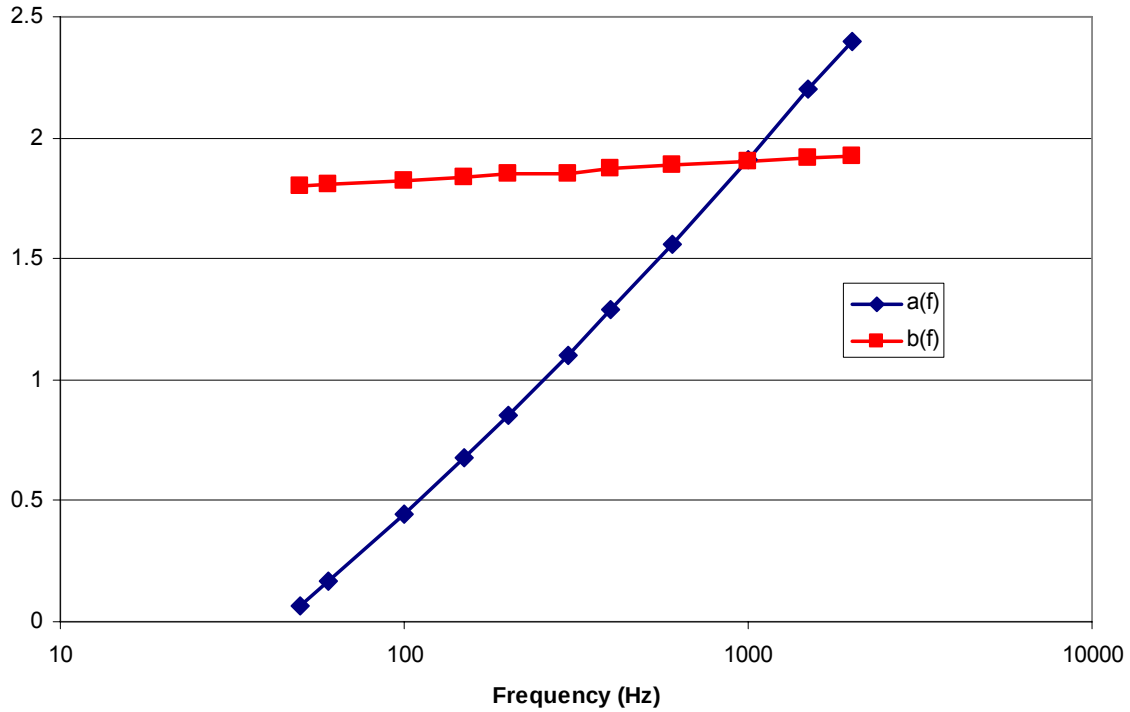

Figure B-3: Behaviour of coefficients a(f) and b(f)

Using CurveExpert 1.3, various curves were applied to the coefficients *a(f)* and *b(f)*, the results of which are summarized in Table B-2.

Table B-2: Various potential SCL odels

	Model Order		Error			
Model Number	***a(f)***	***b(f)***	**Max**	**Min**	**Average**	**RMS**
1	1	1	18.53%	-23.48%	0.60%	9.79%
2	2	1	12.54%	-13.18%	0.15%	5.34%
3	2	2	12.48%	-13.12%	0.15%	5.34%
4	2	3	12.02%	-13.39%	0.14%	5.35%

From this modeling, it can be observed that second order models for *a(f)* and *b(f)* produced strong agreement with the source data. The model for specific core loss, is therefore as follows:

$$SCL = 10^{a(f)+b(f)\cdot\log(B_{\max})}, \quad \textbf{(B-7)}$$

$$a(f) = a_1 + a_2 \cdot \log(f) + a_3 \cdot (\log(f))^2 \quad \textbf{(B-8)}$$

$$b(f) = b_1 + b_2 \cdot \log(f) + b_3 \cdot (\log(f))^2 \quad \textbf{(B-9)}$$

where the coefficients are as follows

$a_1 = -1.5639$ $\quad b_1 = 1.66204$

$a_2 = 0.70179$ $\quad b_2 = 0.07848$

$a_3 = 0.15148$ $\quad b_3 = 0.00060$

and B_{max} is in tesla and f is in Hz.

An important aspect of the model is that as either the frequency or the flux density approach zero, the specific core loss approaches zero, without becoming negative. This model satisfies these criteria because 10^n cannot be negative, and the SCL does decay sharply at low Bmax, as seen in Figure B-4.

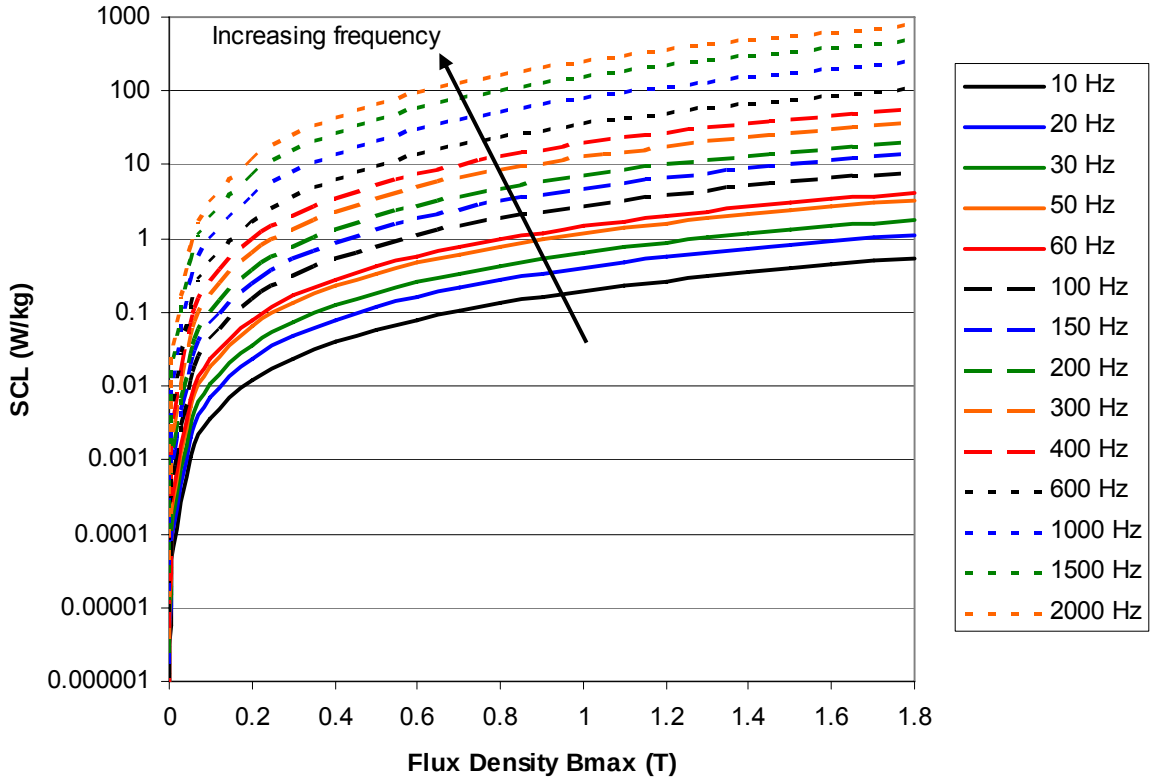

Figure B-4: Core Loss Model

Appendix C

Volumetric Heat Generation by Core Loss

The core loss model developed in Appendix B is dependant upon the frequency and amplitude of the flux density waveform at a given point, however incorporating the core loss model into a thermal model is not a trivial exercise. First, exactly how the frequency and amplitude of the flux density are found and provided to the core loss model must be decided. The most accurate way to predict the flux density waveform is by numerical analysis, however real-time extraction of frequency-dependant information, such as in a multi-physics model, would require that a Fast Fourier Transformation be integrated into the solver. The numerical model can be simplified significantly by performing separate electromagnetic and thermal simulations, as opposed to constructing a more complicated multiphysics model, and using the results predicted by the electromagnetic simulation, namely the core loss in the thermal model. The procedure will be as outlined in Figure C-1, first a numerical simulation will be performed in COMSOL Multiphysics 3.2 to find the flux density waveform, the numerical data of which will be decomposed using the Fast Fourier Transform algorithm, then the Core Loss Model will be used to estimate the actual core loss. To provide a benchmark for comparison, a simplified, assumed waveform will also be analyzed.

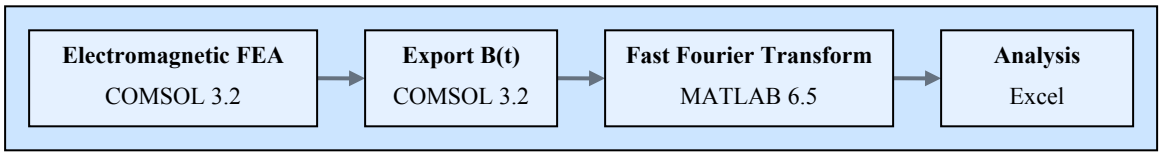

Figure C-1: Method of Determining Core Loss

To provide a baseline, the SRM current waveform seen in Appendix A will be considered. If the first phase is considered, initially there is zero current locally, however the adjacent fourth phase is energized, and the flux it generates returns through the adjacent poles. If half the flux from phase four is considered to return through pole one, and likewise when phase two is energized, then an assumed, normalized flux density waveform could be assumed to be given by

$$\frac{B_1(t)}{B_{\max}} = \frac{I_1 - \frac{1}{2}(I_2 + I_4)}{I_{\max}}, \tag{C-10}$$

which produces the normalized flux density waveform seen in Figure C-2.

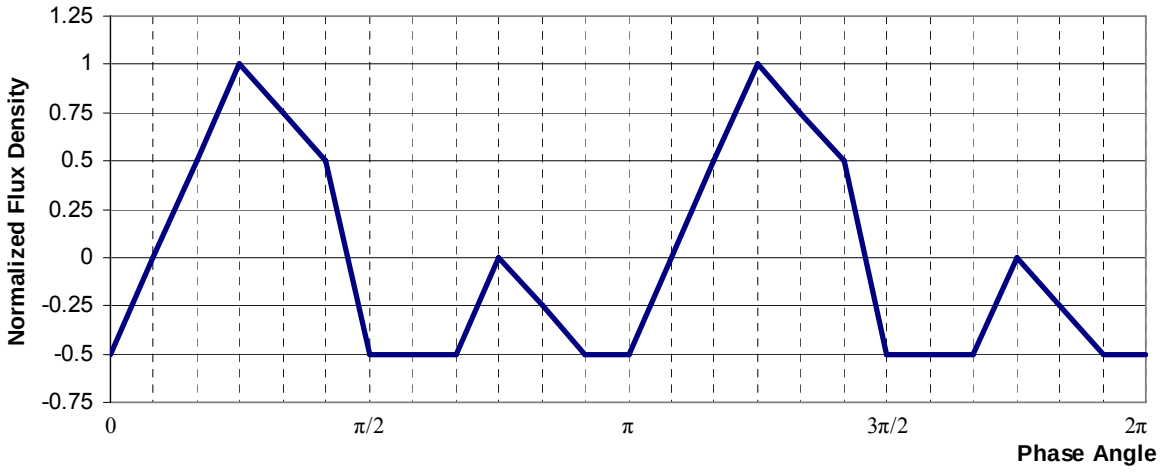

Figure C-2: Assumed flux density in stator pole

To find the core loss which results from this waveform, a Fourier series analysis was performed following the procedure outlined in Appendix A, which produced the results seen in Figure C-3.

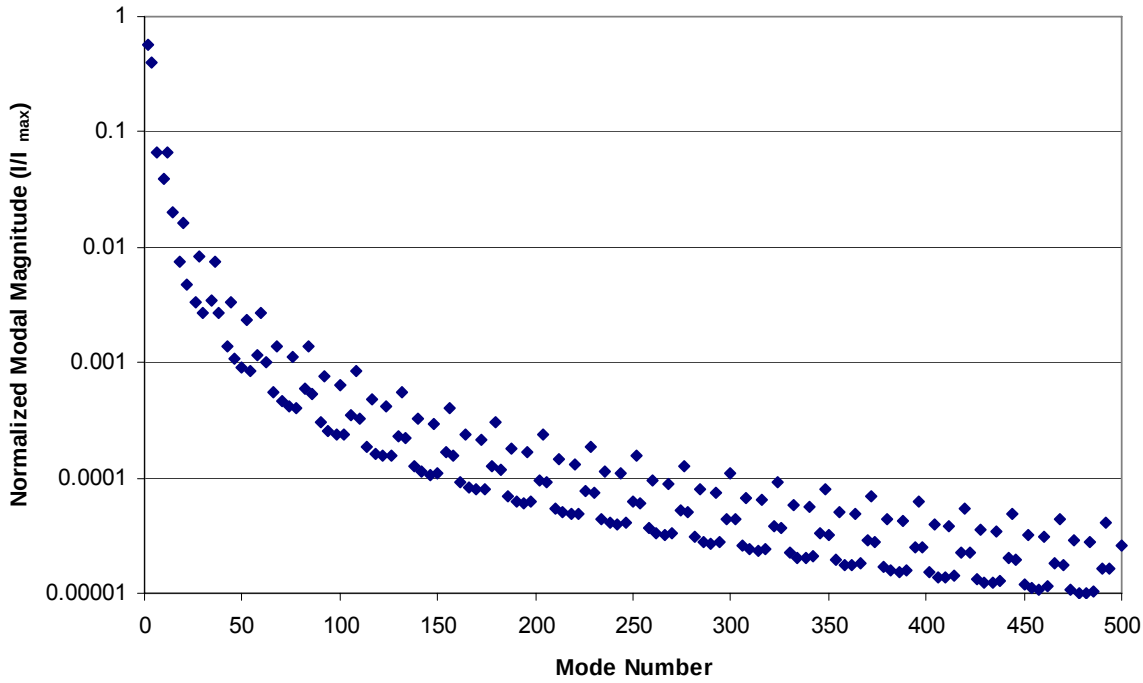

Figure C-3: Model magnitudes for assumed SRM flux density waveform

With the modal magnitudes known, the volumetric core loss can now be found using the uniform flux approximation. The core loss model developed in Appendix B yields the specific core loss in units of W/kg. The volumetric heat generation the stator can be found by

$$q'''_{core,w} = n_B n_s \cdot \rho_{M19} \cdot \sum_{n=1}^{m} SCL(f_n, B_n), \qquad \textbf{(C-11)}$$

where n_B is the core loss saturation factor, n_s is the stator stacking factor, 0.95, and ρ_{M19} is the density of the M-19 steel, 7650 kg/m³. The saturation factor is unknown, and for this model is considered to be unity to represent the upper limit of core loss. With a peak flux density of 1.7 T and a fundamental frequency of 6.67 Hz, it can be seen in Figure C-4 that as the number of modes considered increases, the volumetric heat generation caused by core loss asymptotically approaches 4696.1 W/m³.

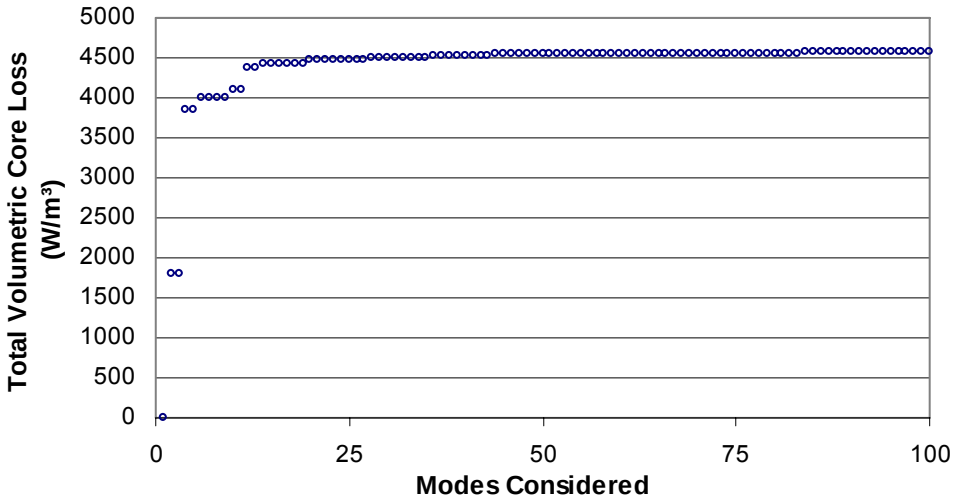

Figure C-4: Cumulative core loss resulting from a flux density SRM waveform with amplitude of 1.7 T and fundamental frequency of 6.67 Hz as a function of the number of modes considered

The advantage of this approach is that it is quite simple, and requires only the software to perform the Fourier series analysis of the waveform. The main disadvantage of this approximation approach is that the resulting core loss will be potentially much higher than the actual value because saturation is assumed throughout the iron components.

The second approach is to perform an electromagnetic finite element analysis on the motor which should produce the most accurate prediction of the core loss as saturation and geometric effects are properly accounted for. The biggest disadvantage of this numerical approach is that specialized software is required to perform such an analysis. The electromagnetic simulation will be performed in COMSOL Multiphysics 3.2.

Determining the core loss using the numerical approach is much more complicated, requiring the use of several pieces of software. The analysis began with a time-dependant finite element model with a 2D geometry constructed in COMSOL Multiphysics 3.2. For this model, linear magnetic behaviour of the M-19 was considered; the relative permeability of 7493 used corresponds to the relative permeability at 1 T, as seen in Figure C-5. To ensure the flux density remained in the linear region, a low-amplitude 5A current used considered. The waveform used was the SRM current waveform, previously developed.

Though the software has the capability of implementing piece-wise function such as the current waveform seen in Figure C-2, it is noted in the user manual [17] that the discontinuous nature of such functions can lead to convergence and reliability issues in both transient and steady state simulations. This issue was avoided by using the data from the Fourier series analysis as the current input to the finite element model. In the finite element model, the SRM current waveform was incorporated by using the Fourier series approximation of the SRM current wave with the previously generated coefficients a_n and b_n from Appendix A. For practical reasons, it was decided to only include the coefficients a_n or b_n if its magnitude exceeded 0.1% of the total amplitude. The time-dependant simulation was performed with a time-step of 0.0003 seconds, which for a period of 0.15 seconds produced 500 data points. This time-step corresponds to a sampling frequency of 3333.3 Hz, which will allow a discrete Fourier transform to find modal amplitudes at frequencies up to 1666.7 Hz for a total of 250 modes.

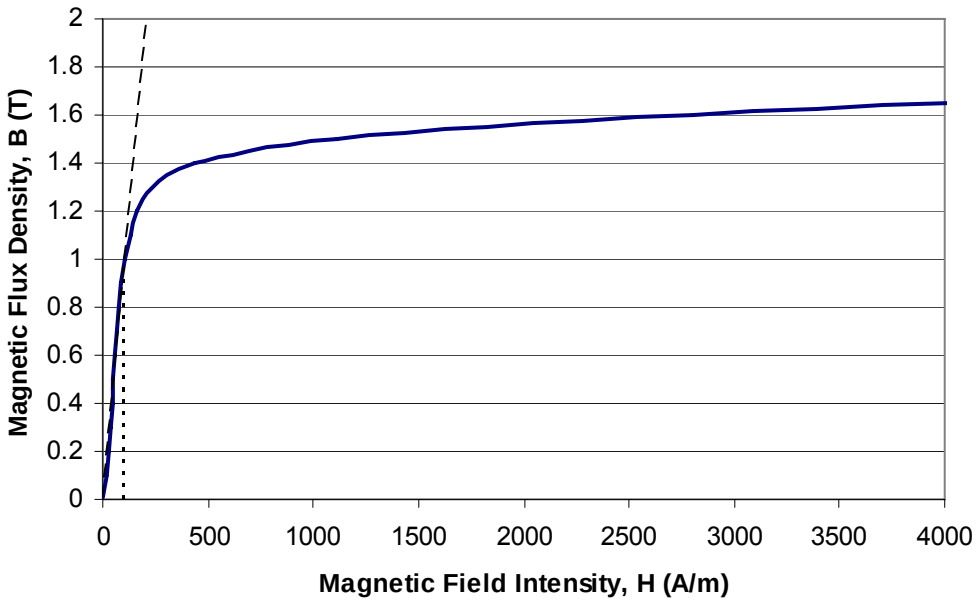

Figure C-5: Linear Region of M-19 Silicon Steel

Switched reluctance motor literature indicates that the flux density waveform is different in various locations of the iron. Following the simulation, the resulting flux density waveforms at three locations of interest, the stator yoke, the stator tooth, and the fieldbooster, were

observed, taken from the locations indicated in Figure C-6, and subsequently exported to MATLAB for further analysis. The resulting waveforms are shown in Figure C-7, and can be seen to exhibit an irregular, periodic shape. A Fast Fourier Transform was performed using MATLAB on the discrete data. The results were normalized such that the flux density waveform had an amplitude of 1.7 T. The modal amplitudes and frequencies found using the Fast Fourier Transform were input into the core loss model, and the resulting core loss in the three components were found, and are plotted against the results of the analytic prediction in Figure C-8.

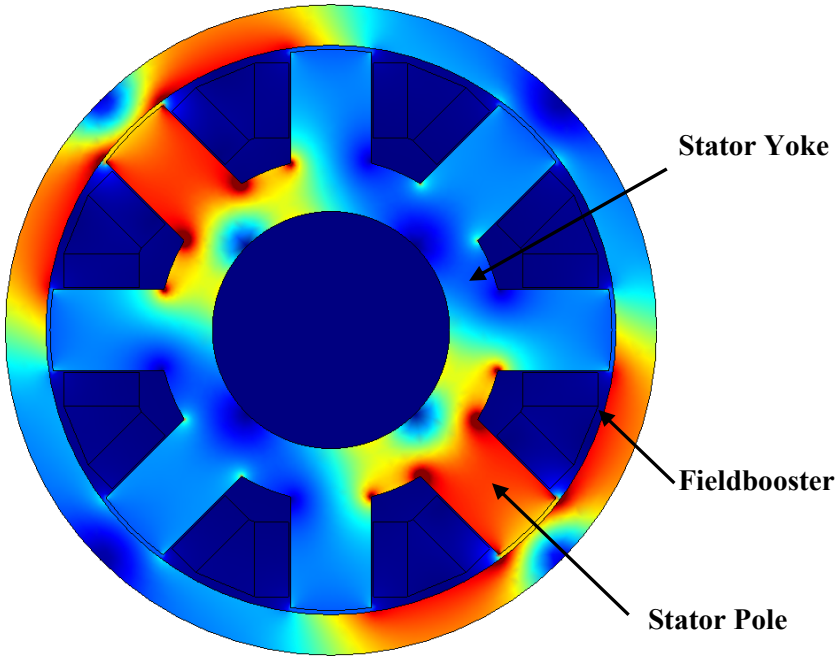

Figure C-6: Locations of interest shown during excitation, red indicates strongest magnetic field

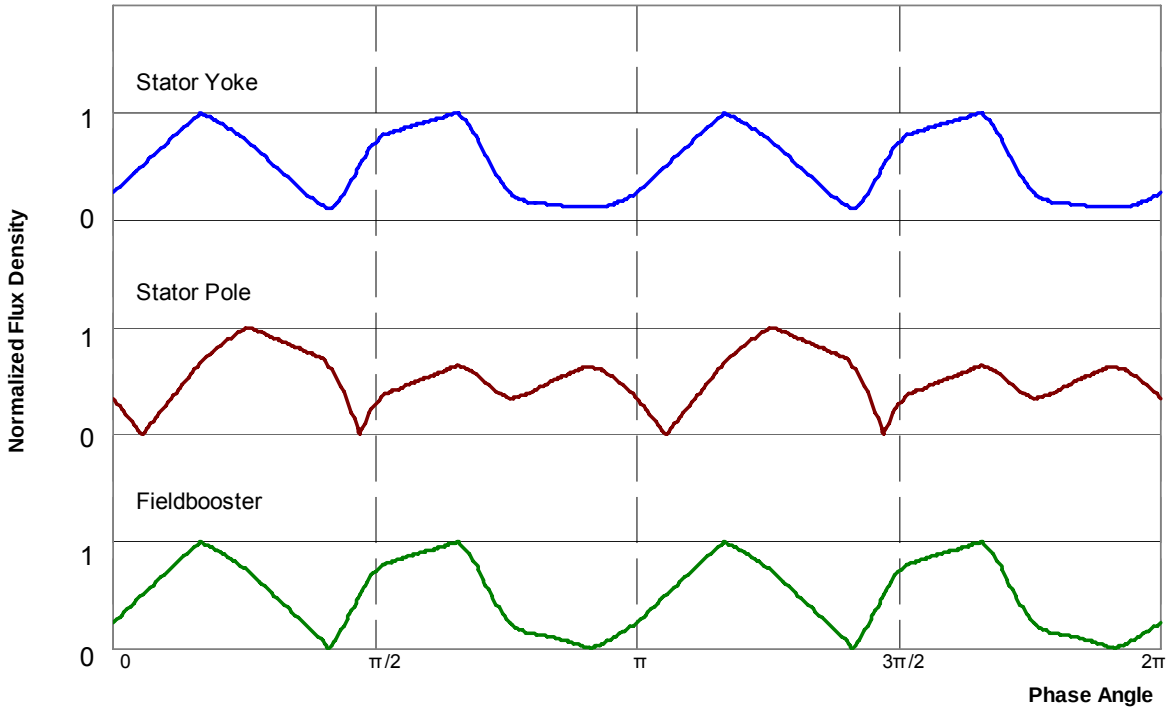

Figure C-7: Magnetic flux density waveforms at various locations

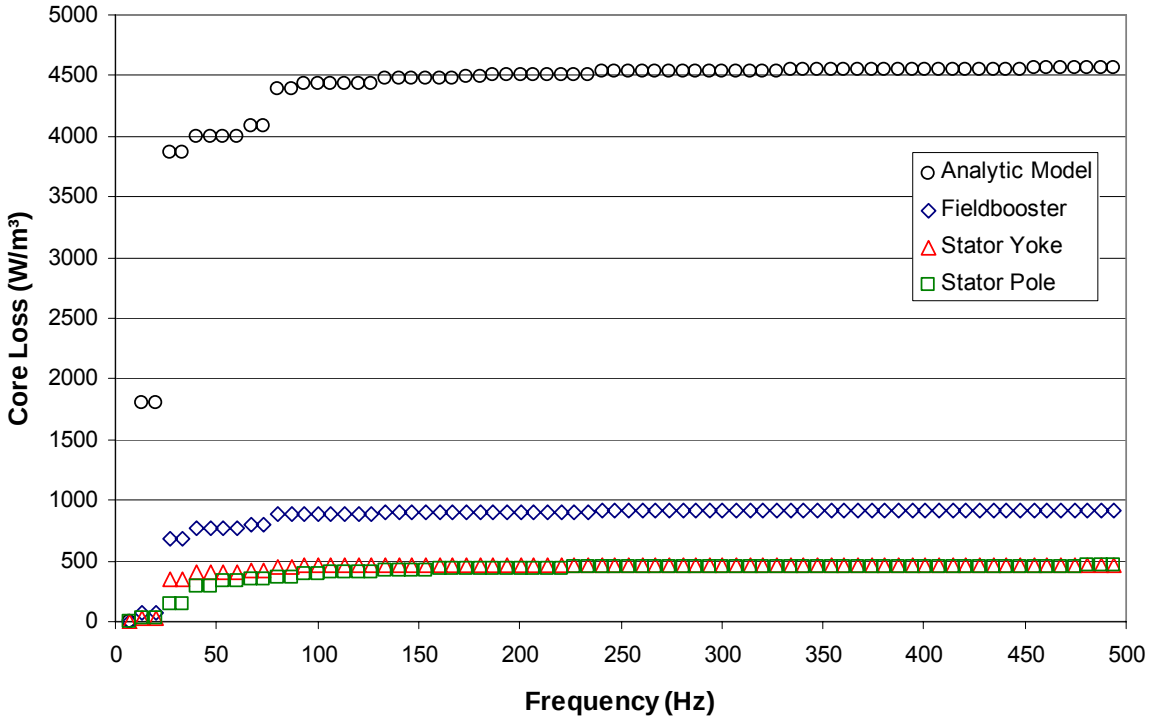

Figure C-8: Core loss

It can be seen in Figure C-8 that the core loss predicted using an analytic model and a finite element model is substantial, and the difference lies entirely in the shape of the waveform. In terms of total heat generation, the difference is substantial; the heat generated in the stator and fieldbooster respectively is predicted to be 1.44 W and 1.67 W respectively, for a total iron loss of 3.11 W, while the analytic model predicted an iron loss of 22.29 W, a difference of a factor of 7.2.

Appendix D

Lumped Parameter Model MATLAB Code

air_alpha.m

```
function [alpha] = air_alpha(T);
alpha=1.8840211e-5 + 1.3384286e-7 .* T + 1.4642857e-10 .* T.^2;
```

air_k.m

```
function [k] = air_k(T);
k=0.024141656  + 7.9137143e-5 .* T - 2.7142857e-8  .* T.^2;
```

air_nu.m

```
function [nu] = air_nu(T);
nu=1.3409261e-5 + 9.0042857e-8 .* T + 9.6428571e-11 .* T.^2;
```

air_Pr.m

```
function [Pr] = air_Pr(T);
Pr=air_nu(T)./air_alpha(T);
```

air_rho.m

```
function [rho] = air_rho(T);
rho=1.2834801  + 4.4489600e-3 .* T - 8.9971429e-6  .* T.^2;
```

Appendix D Lumped Parameter Model MATLAB Code

LPM.m

```
% Lumped Parameter Thermal Model of Prototype Motor
% By Michael J. Pieterse
% Created: 30-March-2009
% Revised: 26-August-2009

% Rotating Case, 1/16th Model
% OR
% Holding Case, 1/4 Model

tic;
disp(' ')

run LPM_pre_1_geometry;

% Solver Information---------------------------------------------- %

% - Inputs
hours = 2.5;            % hrs       Simulation Time
I_rms     = 28.2;       % A         Maximum Current
T_coolant = 22.8;       % degC      Coolant Temperature
CFM       = 37.2;       % ft^3/min  Air Flow Rate
a_fc = 3;
a_c  = 1+0.13629*CFM^0.84085;

% - Simulation Type
On = 1;                 % Motor On/Off (Heating Up/Cooling Down)
Rotating = 1;           % Rotating/Holding
Radiation  = 1;         % On/Off (Include Radiation)
ContactRes = 1;         % On/Off (Include Contact Resistance)
ForcedConv = 1;         % On/Off (Include Convection Cooiling)
ConstVoltage=1;         % Voltage or Current is Constant

% - Air Flow Information
V_dot=CFM/2118.88;      % m^3/s     Air Flow Rate
M_dot=V_dot*air_rho(T_coolant);
                        % kg/s      Air Total Mass Flow Rate
v_inlet=V_dot/(pi*0.01524^2);
                        % m/s       Air inlet velocity
Re_inlet=v_inlet*2*0.01524/air_nu(T_coolant);
                        %           Coolant Reynolds Number

% - Simulation Timescale

Time = hours*3600;      % s         Total Simulation Time
%Time = 5;
t_step = 0.1;         % s         Initial Time Step
steps  = uint32(Time/t_step+1);  % -         Number of Steps at Init. t
step
```

```
step=ones(1,1,'uint32');
n_record = 5;          % s          Frequency of Temp. Recording
recordings=(steps-1)/n_record+1;
t_record = n_record*t_step;

% - Thermal Parameters
T_max = 200;            % degC      Maximum Desirable Motor Temp.
T_air= 22.8;              % degC      Air temperature
dT_dt_min=0.001;        % degC/s    Tolerance for when steady state

% Constants ------------------------------------------------------ %
sigma = 5.67e-8;        % W/m^2*K^4

rho_e = 1.72e-8;        % ohm*m
alpha = 0.0039;         % degC^-1
T_ref = 20;             % degC

Poles = 8;              %           Number of Motor Poles
f_symm=0.5;             %           Factor of Symmetry
SYM=Poles/f_symm;       %           Portion of Motor to be Modelled
angle=2*pi/SYM;         %           Angle of cylindrical components

% Display Simularion Parameters ---------------------------------- %

disp('--------------------------------------')
disp('           Input Parameters')
disp('--------------------------------------')

if On==1;
    disp('Operating Condition:  Heating Up')
else
    disp('Operating Condition:  Cooling Down')
end

if Rotating==1;
    disp('Operating Mode:  Rotating')
    parts=1;
else
    disp('Operating Mode:  Holding')
    parts=4;
end

if Radiation==1;
    disp('Thermal Radiation:    Included')
else
    disp('Thermal Radiation:    Neglected')
end

if ContactRes==1;
    disp('Contact Resistance:   Included')
else
```

```
    disp('Operating Condition:  Neglected')
end

if ForcedConv==1;
    disp('Cooling Mode:         Forced Convection')
    disp(['Airflow:              ',num2str(CFM), ' SCFM'])
    disp(['Air Temperature:      ',num2str(T_coolant),...
        setstr(176),'C'])
else
    disp('Forced Air Cooling:   Natural Convection Only')
end

disp(' ')
disp(['RMS Input Current:    ',num2str(I_rms), ' A'])
disp(['Initial Temperature:  ',num2str(T_air), setstr(176),'C'])
disp(['Maximum Temperature:  ',num2str(T_max), setstr(176),'C'])
disp(['Number of Time Steps: ',num2str(steps)])
disp(['Length of Simulation: ',num2str(Time/60), ' minutes'])
disp(' ')

% - Load Program Segments ------------------------------------- %
run LPM_pre_2_matrix_init;
run LPM_pre_3_material_properties;
run LPM_pre_4_assemble;
run LPM_pre_5_conduction;
run LPM_pre_6_thermal_gen;
run LPM_pre_7_contact_res;
run LPM_pre_8_conv_geometry;
run LPM_pre_9_radiation;

fcl=(D_h(26)/0.0254)^2;  % Fraction of coolant going to lower part
m_dot1=(1-fcl)*M_dot/SYM;
m_dot2=fcl*M_dot/SYM;

t_toshutoff = inf;

if Rotating==0;
    R(:,:,2)= R(:,:,1);
    R(:,:,3)= R(:,:,1);
    R(:,:,4)= R(:,:,1);
end

% ---------------------- Loop Starts Here ---------------------- %
r_step=ones(1,1,'uint32');
t=0;

T_i23 = T_coolant;

T(20,:)=T_i23;
T(21,:)=T_i23;
T(22,:)=T_i23;
T(23,:)=T_i23;
```

```
T(26,:)=T_i23;

% T(:)=T_i23;

if Rotating==1;
    Tt(:,r_step)=T;   % Set Initial Temperatures
else
    Tt(:,r_step,1)=T(:,1);
    Tt(:,r_step,2)=T(:,2);
    Tt(:,r_step,3)=T(:,3);
    Tt(:,r_step,4)=T(:,4);
end

t_plot(r_step)=0;

on=1;
t_ss=0;

while step <= steps;

    step=step+1;

    t=t+t_step;

    % - Temperature Dependant Joule Loss, W
    if ConstVoltage==1;
        n_T = 1/(1 + alpha*(T(17,1)-T_ref));
    else
        n_T = 1 + alpha*(T(17,1)-T_ref);
    end

    if on==1;
        for n=16:18;
            Q(n,1) = Q3joule*n_T*X(n)*Y(n)*Z(n);
        end
    else
        Q(:,:)=0;
    end

    % Temperature Dependant Convection Coefficients, W*m^2/K -----%

    run LPM_main_1_free_conv;

    if ForcedConv==1;
        run LPM_main_2_forced_conv;
    end

    if Radiation==1;
        run LPM_main_3_radiation;
    else
        h_rad_ext(n,24,parts)=0;
```

```
    end

    for o=1:parts;
        U(:,:,o)=h_fc(:,:,o)+h_rad_ext(:,:,o)+h_c(:,:,o);
    end

    % Find Internodal Resistances --------------------------------%

    run LPM_main_4_R_matrix;

    for o=1:parts;
        K(:,:,o)=1./R(:,:,o);
    end

    % -Temperature Change Algorithm------------------------------%

    dT   =zeros(domains,parts); % Change in nodal temperature from
                                % one iteration to the next
    % For Solid Components
    for o=1:parts;
        for i=1:19;
            m=solids(i);
            for n=1:domains;
                dT(m,o)=dT(m,o)+...
                    t_step*K(m,n,o)/C(m)*(T(n,o)-T(m,o));
            end
            dT(m,o) = dT(m,o) + Q(m,o)*t_step/C(m);
        end
    end

    if Rotating ==0;
        for m=1:domains;
            dT(m,1)=dT(m,1)+t_step*K_bc(m,m)/C(m)*(T(m,2)-T(m,1));

            dT(m,2)=dT(m,2)+t_step*K_bc(m,m)/C(m)*(T(m,1)-T(m,2));
            dT(m,2)=dT(m,2)+t_step*K_bc(m,m)/C(m)*(T(m,3)-T(m,2));

            dT(m,3)=dT(m,3)+t_step*K_bc(m,m)/C(m)*(T(m,2)-T(m,3));
            dT(m,3)=dT(m,3)+t_step*K_bc(m,m)/C(m)*(T(m,4)-T(m,3));

            dT(m,4)=dT(m,4)+t_step*K_bc(m,m)/C(m)*(T(m,3)-T(m,4));
        end
    end

    % For The coils

%     dT(16:18,:)=0;
%     coils=[16,17,18];
%     for i=1:3;
%         m=coils(i);
%         KT=0;
```

```
%         for n=1:domains;
%             KT=KT+K(m,n)*(T(m)-T(n));
%         end
%         KT;
%         dT_min_coil(i)=(Q(m)-KT)*t_step/C(m);
%
%         Q3eff=Q(m)*n_T/V(m);
%
%         T_coils(i,3)=T_coils(i,3)+dT_min_coil(i);   % New T Min
%         T_coils(i,1)=T_coils(i,3)+...
%             (6)*R_tc_coil*Q3eff*d_wire+...
%             (9/2)*Q3eff*d_wire^2/k(m);              % New T Max
%
%         dT(m)=T_coils(i,1)-T(m);
%
%     end
T_coils;
    % For Fluid Domains

    % -Inlet Portion, Inside Shaft
    T_23a=T(3)-(T(3)-T_i23)*exp(-K(3,23)/((M_dot/SYM)*cp_air));
    T_o23=T(2)-(T(2)-T_23a)*exp(-K(2,23)/((M_dot/SYM)*cp_air));

    % -Into Top of Motor
    T_i22=T_o23;

    % --Flows over part of gear and the stator yoke
    KT=((K(10,22)/2*T(10)+K(14,22)*T(14))/(K(10,22)/2+K(14,22)));
    T_22a=KT-(KT-T_i22)*...
        exp(-(K(10,22)/2+K(14,22))/(M_dot/SYM*cp_air));
    % --Part flows over gear, epoxy, stator tooth, and coil top
    KT=((K(10,22)/2*T(10)+K(15,22)*T(15)+K(16,22)*T(16)+...
        K(25,22)*T(25))/(K(10,22)/2+K(15,22)+K(16,22)+K(25,22)));
    T_22b=KT-(KT-T_22a)*...
        exp(-(K(10,22)/2+K(15,22)+K(16,22)+K(25,22))/...
        (m_dot1/SYM*cp_air));

    % -Remainder enters "air path" between epoxy and stator
    T_i26=T_22a;

    % --Flows over stator yoke, middle of coil, and epoxy
    KT=((K(14,26)*T(14)+K(17,26)*T(17)+K(25,26)*T(25))/...
        (K(14,26)+K(17,26)+K(25,26)));
    T_o26=KT-(KT-T_i26)*...
        exp(-(K(14,26)+K(17,26)+K(25,26))/((m_dot2/SYM)*cp_air));

    % -Enters bottom of motor
    T_i20=T_o26;

    % --Flows over manifold, diaphragm (inner), and stator yoke
    KT=((K(4,20)*T(4)+K(5,20)*T(5)+K(14,20)*T(14))/...
        (K(4,20)+K(5,20)+K(14,20)));
```

```
T_20a=KT-(KT-T_i20)*...
    exp(-(K(4,20)+K(5,20)+K(14,20))/(m_dot2/SYM*cp_air));

% --Then flows over diaphram (outer), flexispline,
    % stator tooth, coil bottom, and epoxy
KT=((K(6,20)*T(6)+K(7,20)*T(7)+...
    K(15,20)*T(15)+K(18,20)*T(18)+K(25,20)*T(25))/...
    (K(6,20)+K(7,20)+K(15,20)+K(18,20)+K(25,20)));
T_o20=KT-(KT-T_20a)*...
    exp(-(K(6,20)+K(7,20)+K(15,20)+K(18,20)+K(25,20))/...
    (m_dot2/SYM*cp_air));

% -Then enters air gap
T_i21=T_o20;

% --Flows over middle of coil, flexispline, stator tooth, epoxy
KT=((K(17,22)/2*T(17)+K(7,22)*T(7)+K(15,22)*T(15)+...
    K(25,22)*T(25))/(K(17,22)/2+K(7,22)+K(15,22)+K(25,22)));
T_o21=KT-(KT-T_i21)*...
    exp(-(K(17,22)/2+K(7,22)+K(15,22)+K(25,22))/...
    (m_dot2/SYM*cp_air));

% Temperature Change of Air
dT(19)=dT(11);
dT(20)=(T_i20+T_o20)/2-T(20);
dT(21)=(T_i21+T_o21)/2-T(21);
dT(22)=(T_i22+T_22a)/2-T(22);
dT(23)=(T_i23+T_o23)/2-T(23);
dT(24)=0;
dT(26)=(T_i26+T_o26)/2-T(26);
dT;
T = T + dT;

% Check if Maximum Temperaure has been Exceeded
if max(T)>=T_max;
    on=0;
    t_toshutoff=t;
end

% Periodic reporting of temperatures

if mod((step-1),n_record) == 0;
    t=double(step-1)*t_step;
    r_step=r_step+1;
    Tt(:,r_step,:)=T;
    t_plot(r_step)=t;

    % Check if Steady State Conditions are Met
    if max((Tt(:,r_step)-Tt(:,r_step-1))/t_record)<dT_dt_min...
            && t_ss==0;
        t_ss=t;
    end
```

```
    end

    % Find new Film Temperatures
    for n=1:26;
        T_f(n)=(T(n)+T_air)/2;
    end

    Q;

    % Does the Answer Make Sense?
    if imag(sum(T)) ~= 0;
        disp('Simulation Failed: Imaginary Numbers')
        disp('Try Decreasing Time Step')
        break
    end

    if min(T)<T_coolant-1;
        disp('Simulation Failed: Second Law Broken')
        disp('Try Decreasing Time Step')
        break
    end
%    mod(100*double(step)/(double(steps)-1),10)
    if mod(100*double(step)/(double(steps)-1),10) ==0;
        disp([num2str(100*(step-1)/(steps-1)),'% Complete'])
        toc
    end


end

Tt;

units = 0; % default units, seconds
dunits = 'seconds';

if Time > 600;
    units = 1; % set time display units to minutes
    dunits = 'minutes';

end

if Time > 3600*3;
    units = 2;
    dunits = 'hours';
end



disp('')
disp('---------------------------------------')
disp('          Simulation Results')
```

```
disp('-------------------------------------')

if t_ss > 0;
    disp('Steady-State Conditions Achieved')
    disp(['Maximum Temperature:  ',num2str(max(T)),setstr(176),...
            'C'])
    Ttau=(1-(1/exp(1)))*(max(T)-T_air)+T_air;
    tau=0;
    Ttau2=Tt-Ttau;
    for n=1:size(Tt,2);
        if max(Ttau2(:,n)) > 0 && tau==0;
            tau=t_plot(n);
        end
    end
    disp(['Time to Steady State: ',num2str(t_ss/60), ' minutes'])
    disp(['Time Constant tau: ',num2str(tau), ' seconds'])
end

if t_toshutoff < inf;
    disp(['Predicted Time to ',num2str(T_max),setstr(176),'C: ',...
        num2str(t_toshutoff/60), ' minutes'])
end

if t_ss==0 && t_toshutoff==inf;
    disp(['Increase Simulation Time to Find Time to Steady State'])
end

disp(' ')
disp(['Simulation Completed in ', num2str(toc), ' seconds'])

%P=t/t_estimate;

% plot(t_plot,Tt(16,:), 'r', t_plot,Tt(17,:), 'g', ...
%       t_plot,Tt(18,:),'b')
% title(['Temperature Rise of Motor Components Under ',...
%           num2str(I_peak), ' A Peak Current'])
% xlabel(['time (s)'])
% ylabel(['Temperature (', setstr(176),'C)'])

t_axis=Time/60^units;
t_plot=t_plot/60^units;

if Rotating == 1;

    subplot(2,3,[1 2]); plot(t_plot,Tt(18,:),'r-',t_plot,...
        Tt(17,:),'b-', t_plot,Tt(16,:),'g-')
    title(['Thermal Response of Coils at ', num2str(I_rms),...
        ' A RMS Current'])
    %axis([0,t_axis,0,T_max])
    grid
    xlabel(['time (', dunits, ')'])
    ylabel(['Temperature (', setstr(176),'C)'])
```

```
    legend('Bottom', 'Middle', 'Top',0)

    subplot(2,3,3); plot(t_plot,Tt(20,:),'r-',t_plot,Tt(21,:),...
        'b-', t_plot,Tt(22,:),'g-', t_plot,Tt(23,:),'m-')
    title(['Thermal Response of Inner Air at ', num2str(I_rms),...
        ' A RMS Current'])
    %axis([0,t_axis,0,T_max])
    grid
    xlabel(['time (', dunits, ')'])
    ylabel(['Temperature (', setstr(176),'C)'])
    legend('Bottom', 'Middle', 'Top', 'Shaft',0)

    subplot(2,3,4); plot(t_plot,Tt(15,:), 'r', t_plot,Tt(14,:),...
        'b', t_plot,Tt(8,:), 'g')
    title(['M19 Components at ', num2str(I_rms),...
        ' A RMS Current'])
    %axis([0,t_axis,0,T_max])
    grid
    xlabel(['time (', dunits, ')'])
    ylabel(['Temperature (', setstr(176),'C)'])
    legend('Pole', 'Yoke', 'Fieldbooster',0)

    subplot(2,3,5); plot(t_plot,Tt(1,:), 'k', t_plot,Tt(2,:),...
        'b', t_plot,Tt(3,:), 'g', t_plot,Tt(4,:), 'r', t_plot,...
        Tt(5,:), 'm', t_plot,Tt(6,:), 'c')
    title(['Structural Components at ', num2str(I_rms),...
        ' A RMS Current'])
    %axis([0,t_axis,0,T_max])
    grid
    xlabel(['time (', dunits, ')'])
    ylabel(['Temperature (', setstr(176),'C)'])
    legend('Shaft Top', 'Shaft Middle', 'Shaft Bottom', ...
    'Manifold', 'Diaphragm-In', 'Diaphragm-Out' , 0)

    subplot(2,3,6); plot(t_plot,Tt(7,:), 'r', t_plot,Tt(10,:),...
        'g', t_plot,Tt(11,:), 'b')
    title(['Harmonic Drive Components at ', num2str(I_rms), ...
        ' A RMS Current'])
    %axis([0,t_axis,0,T_max])
    grid
    xlabel(['time (', dunits, ')'])
    ylabel(['Temperature (', setstr(176),'C)'])
    legend('Flexispline', 'Gear Bottom', 'Gear Top', 0)

else
    subplot(2,3,1:6); plot(t_plot,Tt(14,:,1),'r',...
        t_plot,Tt(14,:,2),'g', t_plot,Tt(14,:,3), 'b',...
        t_plot,Tt(14,:,4), 'y')
    title(['Coil Temperatures at ', num2str(I_rms), ...
        ' A RMS Current'])
    %axis([0,t_axis,0,T_max])
    grid
```

```
    xlabel(['time (', dunits, ')'])
    ylabel(['Temperature (', setstr(176),'C)'])
    legend('Flexispline', 'Gear Bottom', 'Gear Top', 0)

end

[Tt(18,1),Tt(18,1801),Tt(18,3601),Tt(18,5401),Tt(18,7201),...
    Tt(18,10801),Tt(18,14401),Tt(18,18001)]

Output=[(t_plot/60)',Tt(18,:)'];
```

LPM_pre_1_geometry.m

```
% This file contains information proprietary to Sprung-brett RDI.
% Interested parties should contact Sprung-brett RDI
```

LPM_pre_2_matrix_init.m

```
% Initialize Model Parameter Matricies

V    =zeros(domains,1);         % Volume of parts
A_c  =zeros(domains);           % Convective Surface Area
L    =zeros(domains,1);         % Characteristic geometry

k    =zeros(domains,3);         % Thermal conductivity of part
rho  =zeros(domains,1);         % Density of parts
M    =zeros(domains,1);         % Mass of parts
c    =zeros(domains,1);         % Specific heat of parts
C    =zeros(domains,1);         % Thermal capacity of parts
Nu_c =zeros(domains);           % Nusselt numbers, forced convect'n
h_c  =zeros(domains);           % Conv. Heat Transfer Coefficient
e    =ones(domains,1);          % Emissivity of Materials
Fij  =zeros(domains);           % Thermal Radiation View Factors
A_r  =zeros(domains);           % Radiation Surface Area
A_contact=zeros(domains);       % Area for contact resistance

t_plot=zeros(1,recordings);
Tt=zeros(domains,recordings);
T_f  =T_air*ones(domains,parts);    % Initial film temperature
T    =T_air*ones(domains,parts);    % Initial temperatures
T_coils=T_air*ones(3);              % Special winding temperatures
Q    =zeros(domains,parts);         % Nodal thermal generation
Ra   =zeros(domains,parts);         % Rayleigh Numbers
Nu_fc=zeros(domains,domains,parts); % Nusselt numbers, free convect
h_fc =zeros(domains,domains,parts); % Natural Convection HT Coef.
h_rad_ext=zeros(domains,domains,parts); % External Rad. HT Coef
h_rad_int=zeros(domains,domains,parts); % Internal Rad. HT Coef
U    =zeros(domains,domains,parts);     % Total Heat Transfer Coef.

R    =inf*ones(domains,domains,parts);  % Internodal resist. matrix

R_r_i=zeros(domains,1);         % Radial thermal resistance, outer
R_r_o=zeros(domains,1);         % Radial thermal resistance, inner
R_r_m=zeros(domains,1);         % Radial thermal resistance, mid
R_t_i=zeros(domains,1);         % Tangential thermal res., outer
R_t_o=zeros(domains,1);         % Tangential thermal res., inner
R_t_m=zeros(domains,1);         % Tangential thermal res., mid
R_a_t=zeros(domains,1);         % Axial thermal resistance, top
R_a_b=zeros(domains,1);         % Axial thermal resistance, bottom
R_a_m=zeros(domains,1);         % Axial thermal resistance, mid
K    =zeros(domains);           % Internodal conductance matrix

R_bc =inf*ones(domains);        % Boundary condition resistance
K_bc =zeros(domains);           % BC conductance
```

LPM_pre_3_material_properties.m

```
% Material Properties

% - Isotropic Material Properties
k_4340 = 44.5;  rho_4340 = 7850;    c_4340 = 475;  e_4340=0.45;
k_1045 = 51.3;  rho_1045 = 7850;    c_1045 = 486;  e_1045=0.45;
k_6061 = 167;   rho_6061 = 2700;    c_6061 = 896;  e_6061=0.11;
k_cu   = 396;   rho_cu   = 8933;    c_cu   = 393;  e_cu  =0.09;
k_rubr = 0.13;  rho_rubr = 1100;    c_rubr = 2010; e_rubr=0.9;
k_brng = 10;    rho_brng = 7850;    c_brng = 480;  e_brng=0.45;
k_epox = 1.875; rho_epox = 1900;    c_epox = 1300; e_epox=1;
k_air  = 0.026; rho_air  = 1.2;     cp_air = 1005;
                rho_M_19 = 7330;    c_M_19 = 545;  e_M_19=0.60;
k_coil = 379;   rho_coil = 8616;    c_coil = 429;  e_coil=0.90;

% - Anisotropic Thermal Conductivities
k_M_19_r = 22.815; k_M_19_z = 4.61; % k_M_19_z = 0.371
```

LPM_pre_4_assemble.m

```
% Assemble Fundametal Thermal Parameters Matrix

% ##  Conductivity----Density----------Specific-Heat-Emissivity- %
n= 1; k(n,:)= k_1045; rho(n)= rho_1045; c(n)= c_1045; e(n)=e_1045;
n= 2; k(n,:)= k_1045; rho(n)= rho_1045; c(n)= c_1045; e(n)=e_1045;
n= 3; k(n,:)= k_1045; rho(n)= rho_1045; c(n)= c_1045; e(n)=e_1045;
n= 4; k(n,:)= k_6061; rho(n)= rho_6061; c(n)= c_6061; e(n)=e_6061;
n= 5; k(n,:)= k_4340; rho(n)= rho_4340; c(n)= c_4340; e(n)=e_4340;
n= 6; k(n,:)= k_4340; rho(n)= rho_4340; c(n)= c_4340; e(n)=e_4340;
n= 7; k(n,:)= k_4340; rho(n)= rho_4340; c(n)= c_4340; e(n)=e_4340;
n= 9; k(n,:)= k_rubr; rho(n)= rho_rubr; c(n)= c_rubr; e(n)=e_rubr;
n=10; k(n,:)= k_4340; rho(n)= rho_4340; c(n)= c_4340; e(n)=e_4340;
n=11; k(n,:)= k_4340; rho(n)= rho_4340; c(n)= c_4340; e(n)=e_4340;
n=12; k(n,:)= k_brng; rho(n)= rho_brng; c(n)= c_brng; e(n)=e_brng;
n=13; k(n,:)= k_brng; rho(n)= rho_brng; c(n)= c_brng; e(n)=e_brng;
n=16; k(n,:)= k_coil; rho(n)= rho_coil; c(n)= c_coil; e(n)=e_coil;
n=17; k(n,:)= k_coil; rho(n)= rho_coil; c(n)= c_coil; e(n)=e_coil;
n=18; k(n,:)= k_coil; rho(n)= rho_coil; c(n)= c_coil; e(n)=e_coil;
n=25; k(n,:)= k_epox; rho(n)= rho_epox; c(n)= c_epox; e(n)=e_epox;

% - For Anisotropic Components
n= 8; k(n,:) = k_M_19_r; rho(n) = rho_M_19; c(n) = c_M_19;
      k(n,3) = k_M_19_z;
n=14; k(n,:) = k_M_19_r; rho(n) = rho_M_19; c(n) = c_M_19;
      k(n,3) = k_M_19_z;
n=15; k(n,:) = k_M_19_r; rho(n) = rho_M_19; c(n) = c_M_19;
      k(n,3) = k_M_19_z;

air=[19:24,26];
for m=1:7;
    n=air(m);
    k(n,:)= k_air ; rho(n)= rho_air ; c(n)= cp_air;
end

% Component Volume, m^3 ---------------------------------------- %

% -Cylindrical Components

for n=1:14;
    V(n) = pi*(r_o(n)^2-r_i(n)^2)*Z(n)/SYM;
end

% -Rectangular Components
rect=[15:18,25];
for m=1:5;
    n=rect(m);
    V(n) = X(n)*Y(n)*Z(n);
end

% -Air Regions
```

```
n=19;   V(n) = pi*(r_o(n)^2-r_i(n)^2)*Z(n)/SYM;
n=20;   V(n) = pi*(r_i(7)^2-r_o(4)^2)*0.023428/SYM;
n=21;   V(n) = pi*(r_i(7)^2-r_o(14)^2)/SYM-X(15)*Y(15)-X(17)*Y(17);
n=22;   V(n) = pi*(r_i(7)^2-r_o(4)^2)*0.0415/SYM;
n=23;   V(n) = pi*r_i(2)^2*(Z(2)+Z(3))/SYM;
n=24;   V(n) = 0.1;
n=26;   V(n) = pi*0.0025^2*Z(25);

% Component Mass, m^3 ------------------------------------------ %

for n=1:domains;
    M(n)=rho(n)*V(n);
end

M(18)=1.1*M(18);    % Account for mass of end windings

% Thermal Capacitance, W*s/K ----------------------------------- %

for n=1:domains;
    C(n) = M(n)*c(n);
end

% Thermal Capacitance Correction Factor
C(16:18)=2*C(16:18);


% Thermal Resistance, K/W -------------------------------------- %

% -Solid cylinder
n=1;
    R_a_t(n) = 8*Z(n)/(k(n,3)*pi*(r_o(n)^2-r_i(n)^2));
    R_a_b(n) = R_a_t(n);
    R_a_m(n) = -8*Z(n)/(3*k(n,3)*pi*(r_o(n)^2-r_i(n)^2));
    r_i(n)   = 0.0001;
    R_r_i(n) = 0;
    R_r_o(n) = 4/(pi*k(n)*Z(n,1))*...
        (1-(2*r_i(n)^2*log(r_o(n)/r_i(n))/(r_o(n)^2-r_i(n)^2)));
    R_r_m(n) = -2/(pi*(r_o(n)^2-r_i(n)^2)*k(n,1)*Z(n))*...
        (r_o(n)^2+r_i(n)^2-(4*r_o(n)^2*r_i(n)^2*...
        log(r_o(n)/r_i(n)))/(r_o(n)^2-r_i(n)^2));
    R_t_o(n) = angle/(2*k(n,2)*Z(n)*log(r_o(n)/r_i(n)));
    R_t_i(n) = R_t_i(n);
    R_t_m(n) = -R_t_o(n)/3;

% -Hollow cylindrical components
for n=2:14;
    R_a_t(n) = 8*Z(n)/(k(n,3)*pi*(r_o(n)^2-r_i(n)^2));
    R_a_b(n) = R_a_t(n);
    R_a_m(n) = -8*Z(n)/(3*k(n,3)*pi*(r_o(n)^2-r_i(n)^2));
    R_r_i(n) = 4/(pi*k(n)*Z(n,1))*...
        ((2*r_o(n)^2*log(r_o(n)/r_i(n))/(r_o(n)^2-r_i(n)^2))-1);
```

```
    R_r_o(n) = 4/(pi*k(n,1)*Z(n))*...
        (1-(2*r_i(n)^2*log(r_o(n)/r_i(n))/(r_o(n)^2-r_i(n)^2)));
    R_r_m(n) = -2/(pi*(r_o(n)^2-r_i(n)^2)*k(n,1)*Z(n))*...
        (r_o(n)^2+r_i(n)^2-(4*r_o(n)^2*r_i(n)^2*...
        log(r_o(n)/r_i(n)))/(r_o(n)^2-r_i(n)^2));
    R_t_o(n) = angle/(2*k(n,2)*Z(n)*log(r_o(n)/r_i(n)));
    R_t_i(n) = R_t_i(n);
    R_t_m(n) = -R_t_o(n)/3;
end

n=19;
    R_a_t(n) = 8*Z(n)/(k(n,3)*pi*(r_o(n)^2-r_i(n)^2));
    R_a_b(n) = R_a_t(n);
    R_a_m(n) = -8*Z(n)/(3*k(n,3)*pi*(r_o(n)^2-r_i(n)^2));
    R_r_i(n) = 4/(pi*k(n,1)*Z(n))*...
        ((2*r_o(n)^2*log(r_o(n)/r_i(n))/(r_o(n)^2-r_i(n)^2))-1);
    R_r_o(n) = 4/(pi*k(n,1)*Z(n))*...
        (1-(2*r_i(n)^2*log(r_o(n)/r_i(n))/(r_o(n)^2-r_i(n)^2)));
    R_r_m(n) = -2/(pi*(r_o(n)^2-r_i(n)^2)*k(n,1)*Z(n))*...
        (r_o(n)^2+r_i(n)^2-(4*r_o(n)^2*r_i(n)^2*...
        log(r_o(n)/r_i(n)))/(r_o(n)^2-r_i(n)^2));

% -Rectangular components

for m=1:5;
    n=rect(m);
    R_r_i(n) = X(n)/(k(n,1)*Y(n)*Z(n));
    R_r_o(n) = R_r_i(n);
    R_r_m(n) = -R_r_i(n)/3;
    R_t_i(n) = Y(n)/(k(n,2)*X(n)*Z(n));
    R_t_o(n) = R_t_i(n);
    R_t_m(n) = -R_t_i(n)/3;
    R_a_t(n) = Z(n)/(k(n,3)*X(n)*Y(n));
    R_a_b(n) = R_a_t(n);
    R_a_m(n) = -R_a_t(n)/3;
end

% - If uncommented, model is standard type
% - If commented out, model is D. Roberts Type
for n=1:domains;
    R_r_m(n)=0;
    R_t_m(n)=0;
    R_a_m(n)=0;
end
```

LPM_pre_5_conduction.m

```
% Resistive Network - By Conduction

% 01 - Shaft Top
R(1,2)  = R_a_m(1)+R_a_b(1)+R_a_t(2)+R_a_m(2);
R(1,12) = R_a_m(1)+R_a_t(1)+R_r_i(12)+R_r_m(12);
R(1,13) = R_a_m(1)+R_a_b(1)+R_r_i(13)+R_r_m(13);
R(1,19) = R_r_m(1)+R_r_o(1)+R_r_i(19)+R_r_m(19);
% 02 - Shaft Middle
R(2,1)  = R(1,2);
R(2,3)  = R_a_m(2)+R_a_b(2)+R_a_t(3)+R_a_m(3);
R(2,14) = R_r_m(2)+R_r_o(2)+R_r_i(14)+R_r_m(14);
% 03 - Shaft Bottom
R(3,2)  = R(2,3);
R(3,4)  = R_r_m(3)+R_r_o(3)+R_r_i(4)+R_r_m(4);
% 04 - Manifold
R(4,3)  = R(3,4);
R(4,5)  = R_r_m(4)+R_r_o(4)+R_r_i(5)+R_r_m(5);
% 05 - Diaphragm - Inner
R(5,4)  = R(4,5);
R(5,6)  = R_r_m(5)+R_r_o(5)+R_r_i(6)+R_r_m(6);
% 06 - Diaphragm - Outer
R(6,5)  = R(5,6);
R(6,7) = R_r_m(6)+R_r_o(6)+R_a_b(7)+R_a_m(7);
% 07 - Flexispline
R(7,6)  = R(6,7);
R(7,8)  = R_r_m(7)+R_r_o(7)+R_r_i(8)+R_r_m(8);
% 08 - Fieldbooster
R(8,7)  = R(7,8);
R(8,9)  = R_r_m(8)+R_r_o(8)+R_r_i(9)+R_r_m(9);
% 09 – Thin Coating
R(9,8)  = R(8,9);
% 10 - Gear Bottom
R(10,11)= R_a_m(10)+R_a_t(10)+R_a_b(11)+R_a_m(1);
R(10,13)= R_r_m(10)+R_r_i(10)+R_r_o(13)+R_r_m(13);
% 11 - Gear Top
R(11,10)= R(10,11);
R(11,12)= R_a_m(11)+R_a_t(11)+R_r_o(12)+R_r_m(12);
R(11,19)= R_r_m(11)+R_r_i(11)+R_r_o(19)+R_r_m(19);
% 12 - Bearing Top
R(12,1) = R(1,12);
R(12,11)= R(11,12);
R(12,19)= R_a_m(12)+R_a_b(12)+R_a_t(19)+R_a_m(19);
% 13 - Bearing Bottom
R(13,1) = R(1,13);
R(13,10)= R(10,13);
R(13,19)= R_a_m(13)+R_a_t(13)+R_a_b(19)+R_a_m(19);
% 14 - Stator Core
R(14,2) = R(2,14);
R(14,15)= R_r_m(14)+R_r_o(14)+R_r_i(15)+R_r_m(15);
% 15 - Stator Tooth
R(15,14)= R(14,15);
```

```
R(15,17)= R_t_m(15)+R_t_o(15);
% 16 - Coil Top
R(16,17)= R_a_b(16)+R_a_m(16)+R_a_m(17)+R_a_t(17);
% 17 - Coil Mid
R(17,15)= R(15,17);
R(17,16)= R(16,17);
R(17,18)= R_a_m(17)+R_a_b(17)+R_a_t(18)+R_a_m(18);
R(17,25)= R_t_o(25)+R_t_m(25);
% 18 - Coil Bottom
R(18,17)= R(17,18);
% 19 - Air Pocket
R(19,1)=R(1,19);
R(19,11)=R(11,19);
R(19,12)=R(12,19);
R(19,13)=R(13,19);
% 25 - Epoxy
R(25,17)=R(17,25);

if Rotating==1;
    K_bc=zeros(domains);
else
    bcs=[1:14,25];
    for m=1:15;
        n=bcs(m);
        R_bc(n,n)=2*R_t_o(n);
    end
    K_bc=1./R_bc;
end
```

LPM_pre_6_thermal_gen.m

```
% Thermal Generation

%I_rms = I_peak/sqrt(3);
J_dc  = I_rms/A_wire;
J_rms = I_rms/A_wire;

n_C = 0.96;
n_SP = 1.0078;
if ConstVoltage==1;
    n_T = 1/(1 + alpha*(T_air-T_ref));
else
    n_T = 1 + alpha*(T_air-T_ref);
end

% Volumetric Generation, W/m^3
Q3core_fb = 1000;
Q3core_stator = 500;
if Rotating==1;
    Q3joule = n_C*n_SP*rho_e*J_rms^2;
else
    Q3joule = rho_e*J_dc^2;
end

% -Core Loss, W
if Rotating==1;
    n= 8; Q(n) = Q3core_fb*pi*(r_o(n)^2-r_i(n)^2)*Z(n)/SYM;
    n=14; Q(n) = Q3core_stator*pi*(r_o(n)^2-r_i(n)^2)*Z(n)/SYM;
    n=15; Q(n) = Q3core_stator*X(n)*Y(n)*Z(n);
end

% -Joule Loss, W
for n=16:18;
    Q(n,1) = Q3joule*X(n)*Y(n)*Z(n);
end
```

LPM_pre_7_contact_res.m

```
% Thermal Resistance

% Contact Resistance, m^2*K/W
R_tc_s_a  = 1e-4;           % Steel on Aluminum, tight
R_tc_s_m1 = 1e-4;           % Steel on M19, 0.005" tolerance
R_tc_s_m2 = 1e-4;           % Steel on M19, fill material?
R_tc_s_s  = 1e-4;           % Steel on Steel, tight
R_tc_sl   = 3e-2;           % Coils on M19, Slot Liner
R_tc_coil = 1e-3;           % Coil on Coil

A_contact(1,12) = 2*pi*r_i(12)*Z(12)/SYM;
A_contact(1,13) = 2*pi*r_i(13)*Z(13)/SYM;
A_contact(2,14) = 2*pi*r_i(14)*Z(14)/SYM;
A_contact(3,4)  = 2*pi*r_i(4)*Z(4)/SYM;
A_contact(4,5)  = 2*pi*r_i(5)*Z(5)/SYM;
A_contact(7,8)  = 2*pi*r_i(8)*Z(8)/SYM;
A_contact(10,13)= 2*pi*r_o(13)*Z(13)/SYM;
A_contact(11,12)= 2*pi*r_o(12)*Z(12)/SYM;
A_contact(15,17)= X(17)*Z(17);

if ContactRes==1;
    R(1,12) =R(1,12)+R_tc_s_s/A_contact(1,12);   % Bearing on Shaft
    R(12,1) =R(1,12);
    R(1,13) =R(1,13)+R_tc_s_s/A_contact(1,13);   % Bearing on Shaft
    R(13,1) =R(1,13);
    R(2,14) =R(2,14)+R_tc_s_m1/A_contact(2,14);  % Shaft on Stator
    R(14,2) =R(2,14);
    R(3,4)  =R(3,4)+R_tc_s_a/A_contact(3,4);     % Shaft on Manifld
    R(4,3)  =R(3,4);
    R(4,5)  =R(4,5)+R_tc_s_a/A_contact(4,5);     % Manifld on Diaph
    R(5,4)  =R(4,5);
    R(7,8)  =R(7,8)+R_tc_s_m2/A_contact(7,8);    % FB on Flexisplin
    R(8,7)  =R(7,8);
    R(10,13)=R(10,13)+R_tc_s_s/A_contact(10,13); % Brng on SpurGear
    R(13,10)=R(10,13);
    R(11,12)=R(11,12)+R_tc_s_s/A_contact(11,12); % Brng on SpurGear
    R(12,11)=R(11,12);
    R(15,17)=R(15,17)+R_tc_sl/A_contact(15,17);  % Stator on Coil
    R(17,15)=R(15,17);
end
```

LPM_pre_8_conv_geometry.m

```
% Geometry for Convection

% - Convective Surface Areas, m^2 ------------------------------ %
A_c(1,24) = pi*r_o(1)^2/SYM;
A_c(2,22) = (pi*(r_o(2)^2-0.0317^2)+2*pi*0.0317*0.02278)/SYM;
A_c(2,23) = pi*r_i(2)^2*Z(2)/SYM;
A_c(2,24) = (pi*r_i(2)^2*Z(2)+pi*(r_o(2)^2-r_o(3)^2))/SYM;
A_c(3,23) = pi*r_i(3)^2*Z(3)/SYM;
A_c(3,24) = pi*r_o(3)^2*Z(3)/SYM;
A_c(4,20) = 2*pi*r_o(4)*(Z(4)-Z(5))/SYM;
A_c(4,24) = pi*(r_o(4)^2-r_i(4)^2)/SYM;
A_c(5,20) = pi*(r_o(5)^2-r_i(5)^2)/SYM;
A_c(5,24) = (pi*(r_o(5)^2-r_i(5)^2)+2*pi*r_o(5)*(Z(5)-Z(6)))/SYM;
A_c(6,20) = (r_o(6)^2-r_i(6)^2)/SYM;
A_c(6,24) = (r_o(6)^2-r_i(6)^2)/SYM;
A_c(7,20) = 2*pi*r_i(7)*0.023428/SYM;
A_c(7,21) = 2*pi*r_i(7)*Z(14)/SYM;
A_c(7,22) = 2*pi*r_i(7)*0.0415/SYM;
A_c(7,24) = 2*pi*r_o(7)*(0.0415+0.0235)/SYM;
A_c(8,24) = 2*pi*(r_o(8)^2-r_i(8)^2)/SYM;
A_c(9,24) = (2*pi*r_o(9)*Z(9)+pi*(r_o(9)^2-r_i(9)^2)*2)/SYM;
A_c(10,22)= (pi*(r_o(10)^2-r_i(10)^2)-8*pi/4*0.0254^2+...
            8*pi*0.0254*Z(10)+2*pi*r_o(10)*Z(10))/SYM;
A_c(10,24)= (pi*(r_o(10)^2-r_i(10)^2)-8*pi/4*0.0254^2)/SYM;
A_c(11,24)= (2*pi*r_o(11)*Z(11)+pi*(r_o(11)^2-r_i(11)^2))/SYM;
A_c(12,24)= pi*(r_o(12)^2-r_i(12)^2)/SYM;
A_c(14,20)= pi*(r_o(14)^2-r_o(4)^2)/SYM;
A_c(14,26)= 0.009088*Z(14);
A_c(14,22)= pi*(r_o(14)^2-r_i(14)^2)/SYM;
A_c(15,20)= X(15)*Y(15);
A_c(15,21)= Y(15)*Z(15);
A_c(15,22)= X(15)*Y(15);
A_c(16,22)= 2*(X(16)+Y(16))*Z(16)*1.5;  % 1.5 factor takes into...
%A_c(17,21)= Y(17)*Z(17);
A_c(17,26)= Y(17)*Z(17);
A_c(18,20)= 2*(X(18)+Y(18))*Z(18)*1.5;  % account irregular surface
A_c(25,20)= X(25)*Y(25);
A_c(25,21)= 1.5*Y(25)*Z(25);
A_c(25,22)= X(25)*Y(25);
A_c(25,26)= 0.5*Y(25)*Z(25);

% - Characteristic Geometry, m --------------------------------- %

L(1) = 2*r_o(11);
L(2) = 2*r_o(7);
L(3) = Z(3);
L(4) = 2*r_o(7);
L(5) = 2*r_o(7);
L(6) = 2*r_o(7);
L(7) = Z(7);
L(8) = r_o(8)-r_i(8);
```

```
L(9) = Z(9);
L(10)= 2*r_o(10);
L(11)= Z(11);
L(12)= 2*r_o(11);
L(13)= 2*r_o(13);
L(14)= 2*r_o(14);
L(15)= Z(15);
L(16)= Z(16);
L(17)= Z(17);
L(18)= Z(18);
L(25)= Z(25);

% - Roughness ---------------------------------------------------- %
epsln(20)=0.005;    % Bottom:
epsln(21)=0.001;    % Air Gap:
epsln(22)=0.0005;   % Air Top:
epsln(23)=0.00005;  % Shaft Air: Steel Roughness
epsln(26)=0.001;    % Air Path:  Lamination thickness
```

LPM_pre_9_geometry.m

```
% Radiation Surface Areas and View Factors

% (E) Indicates a Nearly Exact View Factor
% (A+) Indicates (Good) Approximated View Factor
% (A-) Indicates (Poor) Approximated View Factor
% Assumptions were made to simplify geometry so model can be
% adapted to design tool where exact geometry is unknown

m= 6;   % Diaphragm - Outer
    n=18;   A_r(m,n)=pi*(r_o(m)^2-r_i(m)^2)/SYM;
            Fij(m,n)=0.5;     % (A+) Faces Bottom of Coil
    n=25;   A_r(m,n)=pi*(r_o(m)^2-r_i(m)^2)/SYM;
            Fij(m,n)=0.5;     % (A+) Faces Bottom of Epoxy

m=16;   % Coil Top
    n=7;    A_r(m,n)=Y(m)*Z(m);
            Fij(m,n)=1;     % (E) Outer Face Faces Flexispline Only
    n=10;   A_r(m,n)=X(m)*Z(m);
            Fij(m,n)=1;     % (A-) Top Faces Spur Gear Bottom Only
    n=14;   A_r(m,n)=X(m)*Z(m);
            Fij(m,n)=1;     % (A-) Inside Faces Stator Yoke Only
    n=15;   A_r(m,n)=X(m)*Z(m);
            Fij(m,n)=1;     % (A+) Bottom Faces Stator Tooth Only

            A_r(m,:)=1.5*A_r(m,:);

m=25;   % Epoxy
    n=7;    A_r(m,n)=Y(m)*Z(m);
            Fij(m,n)=1;     % (E) Outer Epoxy face faces fs only
    n=10;   A_r(m,n)=X(m)*Y(m);
            Fij(m,n)=1;     % (E) Top Epoxy face faces gear only
    n=6;    A_r(m,n)=X(m)*Y(m);
            Fij(m,n)=1;     % (E) Bottom Epoxy face faces gear only
    n=14;   A_r(m,n)=Y(m)*Z(m);
            Fij(m,n)=1;     % (E) Inner Epoxy faces stator yoke

m=10;   % Gear Bottom
    n=16;   A_r(m,n)=pi*(r_o(m)^2-r_i(m)^2)/SYM;
            Fij(m,n)=Fij(n,m)*A_r(n,m)/A_r(m,n);
    n=25;   A_r(m,n)=pi*(r_o(m)^2-r_i(m)^2)/SYM;
            Fij(m,n)=Fij(n,m)*A_r(n,m)/A_r(m,n);
    n=14;   A_r(m,n)=pi*(r_o(m)^2-r_i(m)^2)/SYM;
            Fij(m,n)=1-Fij(10,16)-Fij(10,25);

m=14;   % Stator Yoke
    n=10;   A_r(m,n)=pi*(r_o(m)^2-r_i(m)^2)/SYM;
            Fij(m,n)=0.75;  % (A+)
    n=16;   A_r(m,n)=pi*(r_o(m)^2-r_i(m)^2)/SYM;
            Fij(m,n)=0.25;  % (A+)
    n=17;   A_r(m,n)=(2*pi*r_o(m)/SYM-Y(n))*Z(m);
```

```
            Fij(m,n)=0.5;     % (A+) Outer Side Half Faces Coil
    n=18;   A_r(m,n)=pi*(r_o(m)^2-r_i(m)^2)/SYM;
            Fij(m,n)=1;     % (E) Outer Side Faces Coil Only
    n=25;   A_r(m,n)=(2*pi*r_o(m)/SYM-Y(n))*Z(m);
            Fij(m,n)=0.5;   % (A+) Outer Side Half Faces Epoxy

m=15;   % Stator Tooth
    n=7;    A_r(m,n)=Y(m)*Z(m);
            Fij(m,n)=1;     % (E) Faces Flexispline Only
    n=16;   A_r(m,n)=X(m)*Y(m);
            Fij(m,n)=1;     % (A+) Top Faces Top Coil Only
    n=18;   A_r(m,n)=X(m)*Y(m);
            Fij(m,n)=1;     % (A-) Bottom Faces Bottom Coil Only


m=17;   % Coil Middle
    n=7;    A_r(m,n)=+Y(m)*Z(m);
            Fij(m,n)=1;     % (E) Outer face faces Flexispline Only
    n=14;   A_r(m,n)=Y(m)*Z(m);
            Fij(m,n)=1;     % (E) Inside Faces Stator Yoke Only

m=18;   % Coil Bottom
    n=6;    A_r(m,n)=X(m)*Z(m);
            Fij(m,n)=1;     % (A-) Bottom Faces Diaphragm Only
    n=7;    A_r(m,n)=Y(m)*Z(m);
            Fij(m,n)=1;     % (E) Outer Face Faces Flexispline Only
    n=14;   A_r(m,n)=Y(m)*Z(m);
            Fij(m,n)=1;     % (A-) Inside Faces Stator Yoke Only
    n=15;   A_r(m,n)=X(m)*Z(m);
            Fij(m,n)=1;     % (A+) Top Faces Stator Tooth Only

            A_r(m,:)=1.5*A_r(m,:);

m= 7;   % Flexispline
    n=15;   A_r(m,n)=2*pi*r_i(m)*Z(m)/SYM;
            Fij(m,n)=Fij(n,m)*A_r(n,m)/A_r(m,n);
    n=16;   A_r(m,n)=2*pi*r_i(m)*Z(m)/SYM;
            Fij(m,n)=Fij(n,m)*A_r(n,m)/A_r(m,n);
    n=17;   A_r(m,n)=2*pi*r_i(m)*Z(m)/SYM;
            Fij(m,n)=Fij(n,m)*A_r(n,m)/A_r(m,n);
    n=18;   A_r(m,n)=2*pi*r_i(m)*Z(m)/SYM;
            Fij(m,n)=Fij(n,m)*A_r(n,m)/A_r(m,n);
    n=25;   A_r(m,n)=2*pi*r_i(m)*Z(m)/SYM;
            Fij(m,n)=Fij(n,m)*A_r(n,m)/A_r(m,n);

    Fij(m,:)=Fij(m,:)./sum(Fij(m,:));   % Ensure Fij sums to 1

% A_enc_top=sum(:,16);
% A_enc_top_coil=
% A_enc_bottom=sum(:,18);
```

LPM_main_1_free_conv.m

```
% Free Convection

solids=[1:18,25];

for m=1:19;
    n=solids(m);
    for i=1:parts;
        Ra(n,i) = 9.81*(1/(T_f(n,i)+273.15))*...
            abs(T(n,i)-T(24,i))*L(n)^3/...
            (air_nu(T_f(n,i))*air_alpha(T_f(n,i)));
    end
end

for o=1:parts;
    h_fc(:,:,o)=0;
    % 20 - Air Bottom
    n=20;
    % Vertical Surfaces (Manifold and Flexispline)
    faces=[4,7];
    for i=1:2;
        m=faces(i);
        Nu_fc(m,n,o) = 0.68+(0.67*Ra(m,o)^(1/4))/...
            (1+(0.492/air_Pr(T_f(m,o)))^(9/16))^(4/9);
        h_fc(m,n,o) = Nu_fc(m,n,o)*air_k(T_f(m,o))/L(m);
    end

    % Horizontal Surfaces Facing Up (Diaphragm (inner/outer))
    faces=[5,6];
    for i=1:2;
        m=faces(i);
        Nu_fc(m,n,o) = 0.001+0.15*Ra(m,o)^(1/3);
        h_fc(m,n,o) = Nu_fc(m,n,o)*air_k(T_f(m,o))/L(m);
    end

    % Horizontal Surfaces Facing Down (Stator)
    faces=[14,15,25];
    for i=1:3;
        m=faces(i);
        Nu_fc(m,n,o) = 0.001+0.27*Ra(m,o)^(1/4);
        h_fc(m,n,o) = Nu_fc(m,n,o)*air_k(T_f(m,o))/L(m);
    end

    % Horizontal Cylinder (Coil Bottom)
    faces=[18];
    for i=1;
        m=faces(i);
        Nu_fc(m,n,o) = (0.6+((0.387*Ra(m,o)^(1/6))/...
            (1+(0.559/air_Pr(T_f(m,o)))^(9/16))^(8/27)))^2;
        h_fc(m,n,o) = Nu_fc(m,n,o)*air_k(T_f(m,o))/L(m);
    end
```

```
% 21 - Air Gap
n=21;
% Vertical Surfaces (Flexispline, Tooth, Coil Mid)
faces=[7,15,17,25];
for i=1:4;
    m=faces(i);
    Nu_fc(m,n,o) = 0.68+(0.67*Ra(m,o)^(1/4))/...
        (1+(0.492/air_Pr(T_f(m,o)))^(9/16))^(4/9);
    h_fc(m,n,o) = Nu_fc(m,n,o)*air_k(T_f(m,o))/L(m);
end

% 22 - Top Air
n=22;
% Vertical Surfaces (Shaft-Middle and Flexispline)
faces=[2,7];
for i=1:2;
    m=faces(i);
    Nu_fc(m,n,o) = 0.68+(0.67*Ra(m,o)^(1/4))/...
        (1+(0.492/air_Pr(T_f(m,o)))^(9/16))^(4/9);
    h_fc(m,n,o) = Nu_fc(m,n,o)*air_k(T_f(m,o))/L(m);
end

% Horizontal Surfaces Facing Up (Stator Yoke, Tooth)
faces=[14,15,25];
for i=1:3;
    m=faces(i);
    Nu_fc(m,n,o) = 0.001+0.15*Ra(m,o)^(1/3);
    h_fc(m,n,o) = Nu_fc(m,n,o)*air_k(T_f(m,o))/L(m);
end

% Horizontal Surfaces Facing Down (Gear Bottom)
faces=[10];
for i=1;
    m=faces(i);
    Nu_fc(m,n,o) = 0.001+0.27*Ra(m,o)^(1/4);
    h_fc(m,n,o) = Nu_fc(m,n,o)*air_k(T_f(m,o))/L(m);
end

% Horizontal Cylinder (Coil Top)
faces=[16];
for i=1;
    m=faces(i);
    Nu_fc(m,n,o) = (0.6+((0.387*Ra(m,o)^(1/6))/...
        (1+(0.559/air_Pr(T_f(m,o)))^(9/16))^(8/27)))^2;
    h_fc(m,n,o) = Nu_fc(m,n,o)*air_k(T_f(m,o))/L(m);
end

% 23 - Shaft Air
n=23;
% Vertical Surfaces (Shaft-Bottom and Middle)
faces=[2,3];
```

```
    for i=1:2;
        m=faces(i);
        Nu_fc(m,n,o) = 0.68+(0.67*Ra(m,o)^(1/4))/...
            (1+(0.492/air_Pr(T_f(m,o)))^(9/16))^(4/9);
        h_fc(m,n,o) = Nu_fc(m,n,o)*air_k(T_f(m,o))/L(m);
    end

    % 24 - External Air
    n=24;

    % Vertical Surfaces
    faces=[2,3,7,9,11];
    for i=1:5;
        m=faces(i);
        Nu_fc(m,n,o) = 0.68+(0.67*Ra(m,o)^(1/4))/...
            (1+(0.492/air_Pr(T_f(m,o)))^(9/16))^(4/9);
        h_fc(m,n,o) = Nu_fc(m,n,o)*air_k(T_f(m,o))/L(m);
    end

    % Horizontal Surfaces Facing Down
    faces=[4,5,6];
    for i=1:3;
        m=faces(i);
        Nu_fc(m,n,o) = 0.001+0.27*Ra(m,o)^(1/4);
        h_fc(m,n,o) = Nu_fc(m,n,o)*air_k(T_f(m,o))/L(m);
    end

    % Horizontal Surfaces Facing Up
    faces=[1,8,10,12];
    for i=1:4;
        m=faces(i);
        Nu_fc(m,n,o) = 0.001+0.15*Ra(m,o)^(1/3);
        h_fc(m,n,o) = Nu_fc(m,n,o)*air_k(T_f(m,o))/L(m);
    end

    % 26 - Air Path
    n=26;
    % Vertical Surfaces (Stator Yoke, Coil Mid)
    faces=[14,17,25];
    for i=1:3;
        m=faces(i);
        Nu_fc(m,n,o) = 0.68+(0.67*Ra(m,o)^(1/4))/...
            (1+(0.492/air_Pr(T_f(m,o)))^(9/16))^(4/9);
        h_fc(m,n,o) = Nu_fc(m,n,o)*air_k(T_f(m,o))/L(m);
    end

    h_fc(:,:,o)=h_fc(:,:,o)+h_fc(:,:,o)';
    h_fc=a_fc*h_fc;
%     for i=1:domains;
%         for j=1:domains;
%             if h_fc(i,j,o)>0;
%                 h_fc(i,j,o)=5;
```

```
%                 end
%             end
%         end
%         h_fc
end
```

LPM_main_2_forced_conv.m

```
% Forced Convection

for o=1:parts;
    h_c(:,:,o)=0;

    part_air=[20,21,26];
    for i=1:3;
        m=part_air(i);
        Re(m)=4*(2*m_dot2)/...
            (pi*air_rho(T(m,o))*air_nu(T(m,o))*D_h(m));
    end

    all_air=[22,23];
    for i=1:2;
        m=all_air(i);
        Re(m)=4*(m_dot1+m_dot2)/...
            (pi*air_rho(T(m,o))*air_nu(T(m,o))*D_h(m));
    end

    % 20 - Air Bottom
    n=20;

    faces=[4,5,6,7,14,15,16,25];
    for i=1:8;
        m=faces(i);
        if Re(n) < 2300;
            Nu_c(m,n,o) = 3.66;
        else
            f=(-1.8*log10((6.9/Re(n))+...
                ((epsln(n)/D_h(n))/3.7)^1.11))^-2;
            Nu_c(m,n,o)=(f/8)*(Re(n)-1000)*air_Pr(T_f(m))/...
                (1+12.7*(f/8)^(1/2)*(air_Pr(T_f(m))^(2/3)-1));
        end
        h_c(m,n,o)=air_k(T_f(m))*Nu_c(m,n,o)/(D_h(n));
    end

    % 21 - Air Gap
    n=21;

    faces=[7,15,17,25];
    for i=1:4;
        m=faces(i);
        if Re(n) < 2300;
            Nu_c(m,n,o) = 3.66;
        else
            f=(-1.8*log10((6.9/Re(n))+...
                ((epsln(n)/D_h(n))/3.7)^1.11))^-2;
            Nu_c(m,n,o)=(f/8)*(Re(n)-1000)*air_Pr(T_f(m))/...
                (1+12.7*(f/8)^(1/2)*(air_Pr(T_f(m))^(2/3)-1));
        end
```

```
        h_c(m,n,o)=air_k(T_f(m))*Nu_c(m,n,o)/(D_h(n));
    end

    % 22 - Top Air
    n=22;

    faces=[2,7,10,14,15,16,25];
    for i=1:7;
        m=faces(i);
        if Re(n) < 2300;
            Nu_c(m,n,o) = 3.66;
        else
            f=(-1.8*log10((6.9/Re(n))+...
                ((epsln(n)/D_h(n))/3.7)^1.11))^-2;
            Nu_c(m,n,o)=(f/8)*(Re(n)-1000)*air_Pr(T_f(m))/...
                (1+12.7*(f/8)^(1/2)*(air_Pr(T_f(m))^(2/3)-1));
        end
        h_c(m,n,o)=air_k(T_f(m))*Nu_c(m,n,o)/(D_h(n));
    end

    % 23 - Air Shaft
    n=23;
    faces=[2,3];
    for i=1:2;
        m=faces(i);
        if Re(n) < 2300;
            Nu_c(m,n,o) = 3.66; % Constant Surface Temperature
        else
            f=(-1.8*log10((6.9/Re(n))+...
                ((epsln(n)/D_h(n))/3.7)^1.11))^-2;
            Nu_c(m,n,o)=(f/8)*(Re(n)-1000)*air_Pr(T_f(m))/...
                (1+12.7*(f/8)^(1/2)*(air_Pr(T_f(m))^(2/3)-1));
        end
        h_c(m,n,o) = air_k(T_f(2))*Nu_c(m,n,o)/(2*r_i(2));
    end

    % 26 - Air Path
    n=26;

    faces=[14,17,25];
    for i=1:3;
        m=faces(i);
        if Re(n) < 2300;
            Nu_c(m,n,o) = 3.66;
        else
            f=(-1.8*log10((6.9/Re(n))+...
                ((epsln(n)/D_h(n))/3.7)^1.11))^-2;
            Nu_c(m,n,o)=(f/8)*(Re(n)-1000)*air_Pr(T_f(m))/...
                (1+12.7*(f/8)^(1/2)*(air_Pr(T_f(m))^(2/3)-1));
        end
        h_c(m,n,o)=air_k(T_f(m))*Nu_c(m,n,o)/(D_h(n));
    end
```

```
    h_c=h_c+h_c';

%     for i=1:domains;
%         for j=1:domains;
%             if h_c(i,j,o)>0;
%                 h_c(i,j,o)=270;
%             end
%         end
%     end

    h_c=a_c*h_c;

end
```

LPM_main_3_radiation.m

```
% To Surroundings

for m=1:12;
    for o=1:parts;
        h_rad_ext(m,24,o)=e(m)*sigma*...
            (T(m,o)+273.15+T(24,o)+273.15)*...
            ((T(m,o)+273.15)^2+(T(24,o)+273.15)^2);
        h_rad_ext(24,m,o)=h_rad_ext(m,24,o);
    end

end

% Special Cases for Radiation

for o=1:parts;
    % - Two Surface Enclosures
    m=7;

        n=15;
            h_rad_int(m,n,o)=sigma*...
            (T(m,o)+273.15+T(n,o)+273.15)*...
            ((T(m,o)+273.15)^2+(T(n,o)+273.15)^2)/...
            (((1-e(m))/e(m))+(1/Fij(m,n))+...
            ((1-e(n))/e(n))*(A_r(m,n)/A_r(n,m)));

            R(m,n,o)=1/(h_rad_int(m,n,o)*A_r(m,n));
            R(n,m,o)=R(m,n,o);

        n=17;
            h_rad_int(m,n,o)=sigma*...
            (T(m,o)+273.15+T(n,o)+273.15)*...
            ((T(m,o)+273.15)^2+(T(n,o)+273.15)^2)/...
            (((1-e(m))/e(m))+(1/Fij(m,n))+...
            ((1-e(n))/e(n))*(A_r(m,n)/A_r(n,m)));

            R(m,n,o)=1/(h_rad_int(m,n,o)*A_r(m,n));
            R(n,m,o)=R(m,n,o);

    m=14;
        n=17;
            h_rad_int(m,n,o)=sigma*...
            (T(m,o)+273.15+T(n,o)+273.15)*...
            ((T(m,o)+273.15)^2+(T(n,o)+273.15)^2)/...
            (((1-e(m))/e(m))+(1/Fij(m,n))+...
            ((1-e(n))/e(n))*(A_r(m,n)/A_r(n,m)));

            R(m,n,o)=1/(h_rad_int(m,n,o)*A_r(m,n));
            R(n,m,o)=R(m,n,o);
```

```
m=16;
    n=7;
        h_rad_int(m,n,o)=sigma*...
        (T(m,o)+273.15+T(n,o)+273.15)*...
        ((T(m,o)+273.15)^2+(T(n,o)+273.15)^2)/...
        (((1-e(m))/e(m))+(1/Fij(m,n))+...
        ((1-e(n))/e(n))*(A_r(m,n)/A_r(n,m)));

        R(m,n,o)=1/(h_rad_int(m,n,o)*A_r(m,n));
        R(n,m,o)=R(m,n,o);

    n=10;
        h_rad_int(m,n,o)=sigma*...
        (T(m,o)+273.15+T(n,o)+273.15)*...
        ((T(m,o)+273.15)^2+(T(n,o)+273.15)^2)/...
        (((1-e(m))/e(m))+(1/Fij(m,n))+...
        ((1-e(n))/e(n))*(A_r(m,n)/A_r(n,m)));

        R(m,n,o)=1/(h_rad_int(m,n,o)*A_r(m,n));
        R(n,m,o)=R(m,n,o);

    n=14;
        h_rad_int(m,n,o)=sigma*...
        (T(m,o)+273.15+T(n,o)+273.15)*...
        ((T(m,o)+273.15)^2+(T(n,o)+273.15)^2)/...
        (((1-e(m))/e(m))+(1/Fij(m,n))+...
        ((1-e(n))/e(n))*(A_r(m,n)/A_r(n,m)));

        R(m,n,o)=1/(h_rad_int(m,n,o)*A_r(m,n));
        R(n,m,o)=R(m,n,o);

    n=15;
        h_rad_int(m,n,o)=sigma*...
        (T(m,o)+273.15+T(n,o)+273.15)*...
        ((T(m,o)+273.15)^2+(T(n,o)+273.15)^2)/...
        (((1-e(m))/e(m))+(1/Fij(m,n))+...
        ((1-e(n))/e(n))*(A_r(m,n)/A_r(n,m)));

        R(m,n,o)=1/(h_rad_int(m,n,o)*A_r(m,n));
        R(n,m,o)=R(m,n,o);

m=18;
    n=6;
        h_rad_int(m,n,o)=sigma*...
        (T(m,o)+273.15+T(n,o)+273.15)*...
        ((T(m,o)+273.15)^2+(T(n,o)+273.15)^2)/...
        (((1-e(m))/e(m))+(1/Fij(m,n))+...
        ((1-e(n))/e(n))*(A_r(m,n)/A_r(n,m)));

        R(m,n,o)=1/(h_rad_int(m,n,o)*A_r(m,n));
        R(n,m,o)=R(m,n,o);
```

```
        n=7;
            h_rad_int(m,n,o)=sigma*...
            (T(m,o)+273.15+T(n,o)+273.15)*...
            ((T(m,o)+273.15)^2+(T(n,o)+273.15)^2)/...
            (((1-e(m))/e(m))+(1/Fij(m,n))+...
            ((1-e(n))/e(n))*(A_r(m,n)/A_r(n,m)));

            R(m,n,o)=1/(h_rad_int(m,n,o)*A_r(m,n));
            R(n,m,o)=R(m,n,o);

        n=14;
            h_rad_int(m,n,o)=sigma*...
            (T(m,o)+273.15+T(n,o)+273.15)*...
            ((T(m,o)+273.15)^2+(T(n,o)+273.15)^2)/...
            (((1-e(m))/e(m))+(1/Fij(m,n))+...
            ((1-e(n))/e(n))*(A_r(m,n)/A_r(n,m)));

            R(m,n,o)=1/(h_rad_int(m,n,o)*A_r(m,n));
            R(n,m,o)=R(m,n,o);

        n=15;
            h_rad_int(m,n,o)=sigma*...
            (T(m,o)+273.15+T(n,o)+273.15)*...
            ((T(m,o)+273.15)^2+(T(n,o)+273.15)^2)/...
            (((1-e(m))/e(m))+(1/Fij(m,n))+...
            ((1-e(n))/e(n))*(A_r(m,n)/A_r(n,m)));

            R(m,n,o)=1/(h_rad_int(m,n,o)*A_r(m,n));
            R(n,m,o)=R(m,n,o);

    m=25;
        n=6;
            h_rad_int(m,n,o)=sigma*...
            (T(m,o)+273.15+T(n,o)+273.15)*...
            ((T(m,o)+273.15)^2+(T(n,o)+273.15)^2)/...
            (((1-e(m))/e(m))+(1/Fij(m,n))+...
            ((1-e(n))/e(n))*(A_r(m,n)/A_r(n,m)));

            R(m,n,o)=1/(h_rad_int(m,n,o)*A_r(m,n));
            R(n,m,o)=R(m,n,o);

        n=7;
            h_rad_int(m,n,o)=sigma*...
            (T(m,o)+273.15+T(n,o)+273.15)*...
            ((T(m,o)+273.15)^2+(T(n,o)+273.15)^2)/...
            (((1-e(m))/e(m))+(1/Fij(m,n))+...
            ((1-e(n))/e(n))*(A_r(m,n)/A_r(n,m)));

            R(m,n,o)=1/(h_rad_int(m,n,o)*A_r(m,n));
            R(n,m,o)=R(m,n,o);
```

```
        n=10;
            h_rad_int(m,n,o)=sigma*...
            (T(m,o)+273.15+T(n,o)+273.15)*...
            ((T(m,o)+273.15)^2+(T(n,o)+273.15)^2)/...
            (((1-e(m))/e(m))+(1/Fij(m,n))+...
            ((1-e(n))/e(n))*(A_r(m,n)/A_r(n,m)));

            R(m,n,o)=1/(h_rad_int(m,n,o)*A_r(m,n));
            R(n,m,o)=R(m,n,o);

        n=14;
            h_rad_int(m,n,o)=sigma*...
            (T(m,o)+273.15+T(n,o)+273.15)*...
            ((T(m,o)+273.15)^2+(T(n,o)+273.15)^2)/...
            (((1-e(m))/e(m))+(1/Fij(m,n))+...
            ((1-e(n))/e(n))*(A_r(m,n)/A_r(n,m)));

            R(m,n,o)=1/(h_rad_int(m,n,o)*A_r(m,n));
            R(n,m,o)=R(m,n,o);
end
```

LPM_main_4_R_matrix.m

```
% Update Temperature Dependent Portions of R matrix

for i=1:parts;

    % 20 - Air Bottom
    n=20;
        m=4;    R(m,n,o)=R_a_m(m)+R_a_t(m)+1/(U(m,n,o)*A_c(m,n));
                R(n,m,o)=R(m,n,o);
        m=5;    R(m,n,o)=R_a_m(m)+R_a_t(m)+1/(U(m,n,o)*A_c(m,n));
                R(n,m,o)=R(m,n,o);
        m=6;    R(m,n,o)=R_a_m(m)+R_a_t(m)+1/(U(m,n,o)*A_c(m,n));
                R(n,m,o)=R(m,n,o);
        m=7;    R(m,n,o)=R_r_m(m)+R_r_i(m)+1/(U(m,n,o)*A_c(m,n));
                R(n,m,o)=R(m,n,o);
        m=14;   R(m,n,o)=R_a_m(m)+R_a_b(m)+1/(U(m,n,o)*A_c(m,n));
                R(n,m,o)=R(m,n,o);
        m=15;   R(m,n,o)=R_a_m(m)+R_a_b(m)+1/(U(m,n,o)*A_c(m,n));
                R(n,m,o)=R(m,n,o);
        m=18;   R(m,n,o)=1/(U(m,n,o)*A_c(m,n));
                R(n,m,o)=R(m,n,o);
        m=25;   R(m,n,o)=R_a_m(m)+R_a_b(m)+1/(U(m,n,o)*A_c(m,n));
                R(n,m,o)=R(m,n,o);

    % 21 - Air Gap
    n=21;
        m=7;    R(m,n,o)=R_r_m(m)+R_r_i(m)+1/(U(m,n,o)*A_c(m,n));
                R(n,m,o)=R(m,n,o);
        m=15;   R(m,n,o)=R_r_m(m)+R_r_o(m)+1/(U(m,n,o)*A_c(m,n));
                R(n,m,o)=R(m,n,o);
%        m=17;   R(m,n,o)=1/(U(m,n,o)*A_c(m,n));
                R(n,m,o)=R(m,n,o);
        m=25;   R(m,n,o)=R_r_m(m)+R_r_o(m)+1/(U(m,n,o)*A_c(m,n));
                R(n,m,o)=R(m,n,o);

    % 22 - Top Air
    n=22;
        m=7;    R(m,n,o)=R_r_m(m)+R_r_i(m)+1/(U(m,n,o)*A_c(m,n));
                R(n,m,o)=R(m,n,o);
        m=10;   R(m,n,o)=R_a_m(m)+R_a_b(m)+1/(U(m,n,o)*A_c(m,n));
                R(n,m,o)=R(m,n,o);
        m=14;   R(m,n,o)=R_a_m(m)+R_a_t(m)+1/(U(m,n,o)*A_c(m,n));
                R(n,m,o)=R(m,n,o);
        m=15;   R(m,n,o)=R_a_m(m)+R_a_t(m)+1/(U(m,n,o)*A_c(m,n));
                R(n,m,o)=R(m,n,o);
        m=16;   R(m,n,o)=1/(U(m,n,o)*A_c(m,n));
                R(n,m,o)=R(m,n,o);
        m=25;   R(m,n,o)=R_a_m(m)+R_a_t(m)+1/(U(m,n,o)*A_c(m,n));
                R(n,m,o)=R(m,n,o);

    % 23 - Shaft Air
```

```
    n=23;
        m=2;    R(m,n,o)=R_r_m(m)+R_r_i(m)+1/(U(m,n,o)*A_c(m,n));
                R(n,m,o)=R(m,n,o);
        m=3;    R(m,n,o)=R_r_m(m)+R_r_i(m)+1/(U(m,n,o)*A_c(m,n));
                R(n,m,o)=R(m,n,o);

    % 24 - Ambient Air
    n=24;
        m=1;    R(m,n,o)=R_a_m(m)+R_a_t(m)+1/(U(m,n,o)*A_c(m,n));
                R(n,m,o)=R(m,n,o);
        m=2;    R(m,n,o)=R_a_m(m)+R_a_b(m)+1/(U(m,n,o)*A_c(m,n));
                R(n,m,o)=R(m,n,o);
        m=3;    R(m,n,o)=R_r_m(m)+R_r_o(m)+1/(U(m,n,o)*A_c(m,n));
                R(n,m,o)=R(m,n,o);
        m=4;    R(m,n,o)=R_a_m(m)+R_a_b(m)+1/(U(m,n,o)*A_c(m,n));
                R(n,m,o)=R(m,n,o);
        m=5;    R(m,n,o)=R_a_m(m)+R_a_b(m)+1/(U(m,n,o)*A_c(m,n));
                R(n,m,o)=R(m,n,o);
        m=6;    R(m,n,o)=R_a_m(m)+R_a_b(m)+1/(U(m,n,o)*A_c(m,n));
                R(n,m,o)=R(m,n,o);
        m=7;    R(m,n,o)=R_a_m(m)+R_a_t(m)+1/(U(m,n,o)*A_c(m,n));
                R(n,m,o)=R(m,n,o);
        m=8;    R(m,n,o)=R_a_m(m)+R_a_b(m)+1/(U(m,n,o)*A_c(m,n));
                R(n,m,o)=R(m,n,o);
        m=9;    R(m,n,o)=R_r_m(m)+R_r_o(m)+1/(U(m,n,o)*A_c(m,n));
                R(n,m,o)=R(m,n,o);
        m=10;   R(m,n,o)=R_a_m(m)+R_a_t(m)+1/(U(m,n,o)*A_c(m,n));
                R(n,m,o)=R(m,n,o);
        m=11;   R(m,n,o)=R_r_m(m)+R_r_o(m)+1/(U(m,n,o)*A_c(m,n));
                R(n,m,o)=R(m,n,o);
        m=12;   R(m,n,o)=R_a_m(m)+R_a_t(m)+1/(U(m,n,o)*A_c(m,n));
                R(n,m,o)=R(m,n,o);

    % 26 - Air Path
    n=26;
        m=14;   R(m,n,o)=R_r_m(m)+R_r_o(m)+1/(U(m,n,o)*A_c(m,n));
                R(n,m,o)=R(m,n,o);
        m=17;   R(m,n,o)=R_r_m(m)+R_r_i(m)+1/(U(m,n,o)*A_c(m,n));
                R(n,m,o)=R(m,n,o);
        m=25;   R(m,n,o)=R_r_m(m)+R_r_i(m)+1/(U(m,n,o)*A_c(m,n));
                R(n,m,o)=R(m,n,o);
end
```

Appendix E

LabVIEW Virtual Instrument Block Diagram

In order to find the heat flux from the HFS-4 sensor, the temperature correction equation from Section 4.1.2 must be incorporated in real-time into the data acquisition Virtual Instrument (VI). The following sub-VI takes the sensor temperature, measured from the imbedded K-type thermocouple, the voltage generated by the heat flux sensor, and the gain specific to the sensor used and outputs the heat flux in units of W/m².

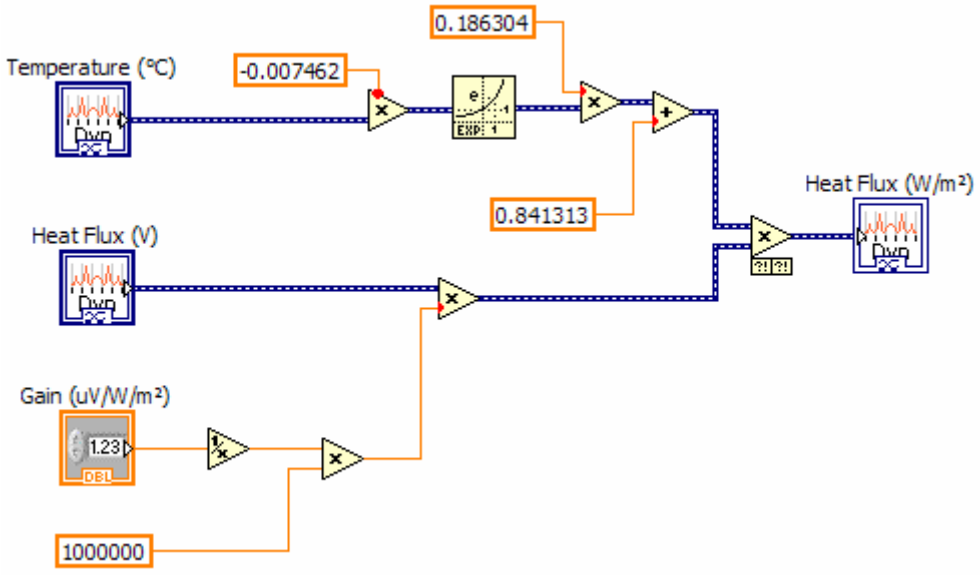

Figure E-1: Heat flux sensor sub-VI

Appendix E LabVIEW Virtual Instrument Block Diagram

The main VI collects the temperature from eight thermocouples and the voltages from four heat flux sensors and computes, displays, and records the eight temperatures, the time-rate-of-change of those temperatures, and the heat flux at four locations.

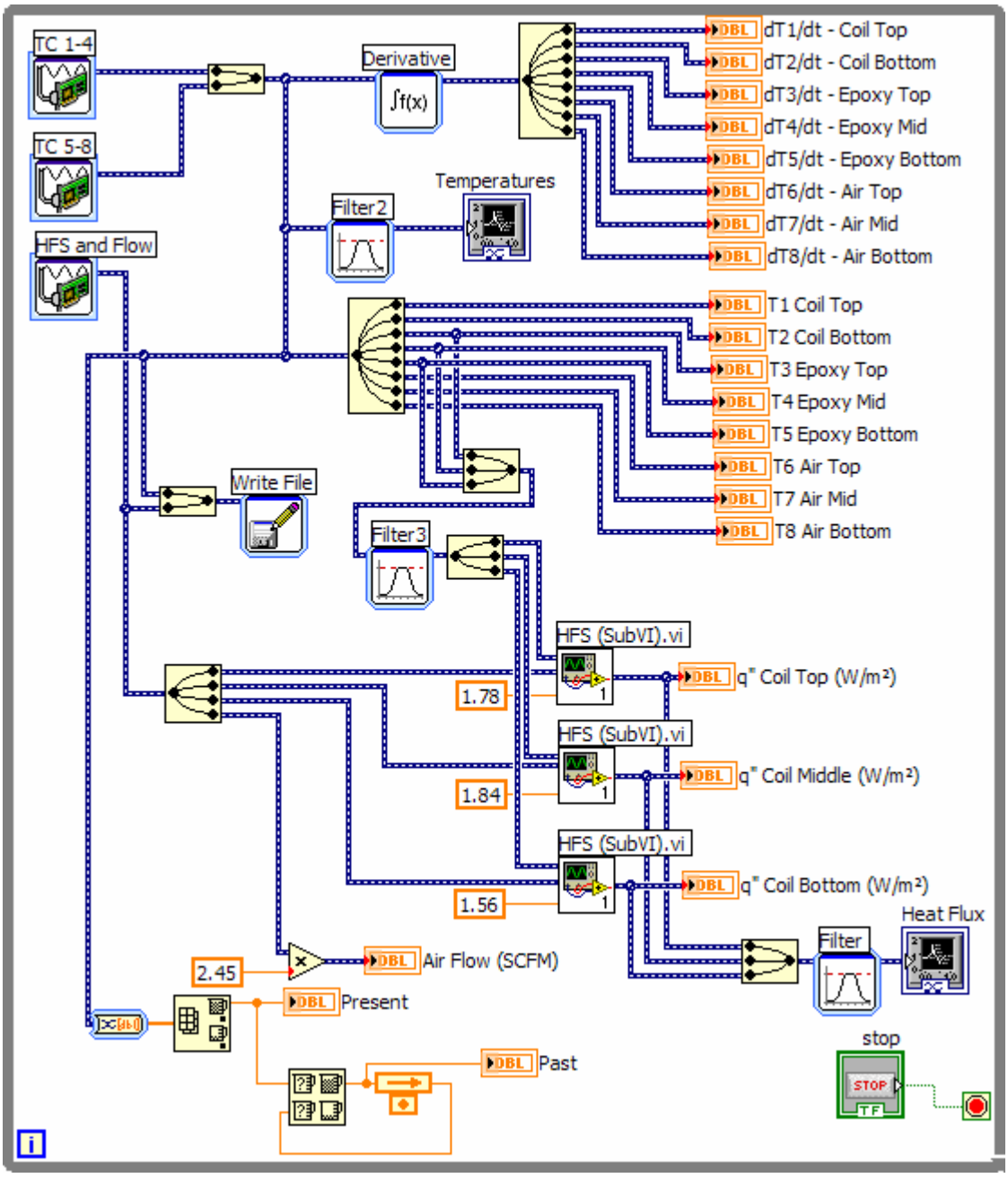

Figure E-2: Motor thermal VI